THE UNIVERSITY OF
WARWICK

AUTHOR: **Simon Richard Guy Joyce**   DEGREE: **MSc**

TITLE: **The X-ray emissions of Cataclysmic Variables during the eclipse of the White Dwarf.**

DATE OF DEPOSIT: ....

I agree that this thesis shall be available in accordance with the regulations governing the University of Warwick theses.

I agree that the summary of this thesis may be submitted for publication.

I **agree** that the thesis may be photocopied (single copies for study purposes only).

Theses with no restriction on photocopying will also be made available to the British Library for microfilming. The British Library may supply copies to individuals or libraries. subject to a statement from them that the copy is supplied for non-publishing purposes. All copies supplied by the British Library will carry the following statement:

> "Attention is drawn to the fact that the copyright of this thesis rests with its author. This copy of the thesis has been supplied on the condition that anyone who consults it is understood to recognise that its copyright rests with its author and that no quotation from the thesis and no information derived from it may be published without the author's written consent."

AUTHOR'S SIGNATURE: ....

USER'S DECLARATION

1. I undertake not to quote or make use of any information from this thesis without making acknowledgement to the author.

2. I further undertake to allow no-one else to use this thesis while it is in my care.

DATE   SIGNATURE   ADDRESS

....

....

....

....

....

The X-ray emissions of Cataclysmic Variables during the eclipse of the White Dwarf.

by

Simon Richard Guy Joyce

Thesis

Submitted to The University of Warwick

for the degree of

Master of Science (by Research)

Department of Physics

June 2012

THE UNIVERSITY OF

WARWICK

Contents

List of Tables

List of Figures

vii

Acknowledgments

I would like to thank my supervisor, Dr Peter Wheatley, for giving me the opportunity to study astronomy. His guidance and enthusiasm have helped me to learn more than I could have imagined.

I would also like to thank George, Joao, Steven, Rachel, Sandra, Jon G and John R, Simon, Elme, Philip, Penelope, Madelon, Nicola and Stylianos for their friendship and for many helpful hints and illuminating conversations. Special thanks to Rachel for the steady supply of tea and biscuits which keep us all going.

Finally thank you to my parents, Michael and Elaine for supporting me and guiding me throughout my life. Without them, none of it would have been possible.

Declarations

I, Simon Richard Guy Joyce, hereby declare that this thesis has not been submitted before to any university for the award of a higher degree. This thesis is my own work except where references to other works are given.

Abstract

I present analysis of X-ray and optical observations made using XMM-Newton. The cataclysmic variable systems Z Cha, HT Cas and OY Car are eclipsing systems which gives us a chance to search for residual X-ray emission while the white dwarf and boundary layer are eclipsed. X-rays are detected during the eclipses of all 3 systems in the $0.2 - 1.4\,\mathrm{keV}$ range. The X-ray luminosity of the in-eclipse sources is estimated at $3.09 - 3.14 \times 10^{28}\,\mathrm{erg\,s^{-1}}$. In all 3 systems the in-eclipse source is much softer than the out-of-eclipse source. Evidence from analysis of the spectra, hardness ratios and variability of the sources strongly suggest that the in-eclipse X-rays have a different origin to the out-of-eclipse X-rays.

I discuss the possible origin of these emissions such as scattered boundary layer emission, the corona of the secondary star and the accretion disk bright spot. The results suggest that the most likely source of the in-eclipse X-rays is coronal emission from the secondary star. Analysis of the optical light curve shows that in the Z Cha observation, some of the in-eclipse X-rays may be from the bright spot. The in-eclipse sources are inconsistent with a model for scattered boundary layer emission.

Chapter 1

Introduction

When seen from Earth, each star seems to have its own place in the sky. Even though we know the stars are enormous, they seem dwarfed by the huge distances between them. But our perception of stars as these solitary giants is misleading. Many have close companions in a mutual orbit. Some are so closely bound together that they have a profound influence on each others behaviour and evolution. While one of the stars may be hidden in the glare of its more brilliant companion, it is the material sacrificed by this secondary star which allows the primary star to shine on, long after its natural life has ended.

1.1 Cataclysmic variables

1.1.1 Binary stars

A binary star system consists of two stars orbiting each other. There are many classes of binary system depending on properties such as the masses of the stars, the orbital separation and the way the two stars interact with each other.

The orbital period and separation of binary stars are related by Keplers 3rd law.

$$P_{orb}^2 = \frac{4\pi^2 a^3}{G\left(M_1 + M_2\right)} \tag{1.1}$$

M_1 and M_2 are the masses of the two stars, a is the separation and G is the universal gravitational constant. One important result of this law is that for two stars of a given mass, a smaller orbital separation will result in a shorter orbital period.

The stars in a wide binary will evolve as if they were single stars. The only effect of being in a wide binary is that the two stars orbit around the binary centre of mass. There are also close binary systems where the stars are close enough together

to interact in a variety of ways. Often the two stars have a different initial mass which means one will evolve more quickly than the other. When the more massive star evolves off the main sequence it will expand which causes a redistribution of the mass in the system. This leads to changes in the orbital separation of the stars. There is the possibility that the stars will move close enough together so that matter can transfer from one star to the other.

The wide range of possible configurations of close binary systems has led to many subcategories. The type of systems studied in this thesis are cataclysmic variables (CVs) which are a class of binary where one star is a white dwarf and the other is a low mass main sequence or evolved star (Warner, 1995b). Closely related to cataclysmic variables are systems where the high mass star has evolved into a neutron star or a black hole. These are called low mass X-ray binaries if the second star is a low mass main sequence star. They are high mass X-ray binaries if the second star is a high mass giant.

1.1.2   Roche lobe

The Roche model (Kopal, 1959) is a way of describing the potential of a particle due to the net gravitational force acting on it. A particle of mass (m) will be attracted more to one of the stars depending on the balance of forces acting on the particle. The resultant force acting on a particle will depend on the mass of the two stars and the distance of the particle from each star. In a binary system there is also a centrifugal force due to the rotation of the system. The Roche potential determines the direction the particle will move since the resultant force acts to make particles move from regions of high potential to regions of low potential.

In between the stars there is a point where the force on a particle due to the gravitational attraction of one star will be balanced by the attraction of the other star. This is called the inner Lagrange point. The material that makes up each star will also be affected by the gravitational attraction of the other star, but as long as it is not near the Lagrange point, the attraction of the host star will be stronger.

A Roche equipotential surface is a surface where the Roche potential is the same at any point on the surface. When a star is in equilibrium, its surface will be defined by a Roche equipotential. A star's Roche lobe is a special Roche equipotential surface, which is in contact with the inner Lagrange point. It defines the maximum volume a star can fill before mass overflows the Lagrange point.

1.1.3 Mass transfer

It is possible for matter to transfer from one star to the other in a binary system. The lower mass star that is losing matter is called the secondary, while the star that is gaining matter by accretion is called the primary. In the case of CVs, the primary is a white dwarf so it is much more compact than the secondary star.

If the secondary does not fill its Roche lobe it can still lose mass by its stellar wind. This is more important when the secondary is a high mass star with a strong stellar wind. In some binary systems, matter is transferred from one star to the other by the process of Roche lobe overflow. These are categorised as semi-detached systems (Kopal, 1978).

In the Roche lobe overflow type of mass transfer(Kuiper, 1941), the secondary star fills its Roche lobe either because the star is expanding as it evolves or because the Roche lobe shrinks as the stars move closer together (Paczynski, 1967). The result of a star filling its Roche lobe is that material from the secondary star's surface that is near the Lagrange point (fig 1.1) can fall into the potential well of the primary star and so matter from the secondary transfers to the primary (Paczynski, 1971).
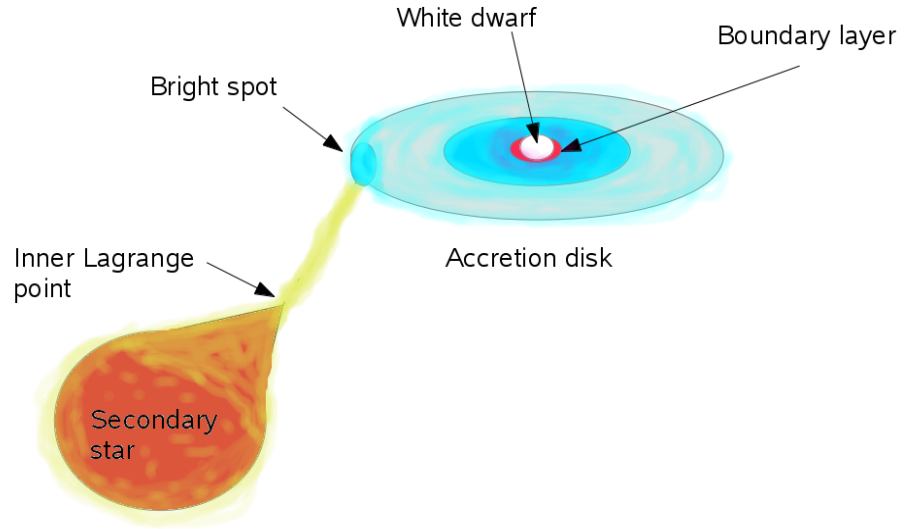
Figure 1.1: The general structure of a non-magnetic cataclysmic variable with the transfer of matter from the secondary star to the white dwarf via the accretion disk. Note that colours and scale are for illustrative purposes only.

1.1.4 Accretion disks

In systems where the flow of material is not influenced by magnetic fields, material from the secondary flows in a stream towards the white dwarf. The Roche potential acts in a co-rotating reference frame so the accretion stream is subject to the Coriolis effect (Lubow and Shu, 1975). The result is that material cannot fall directly on to the white dwarf. Instead, the material goes into orbit around the white dwarf and forms an accretion disk in the plane of the orbit of the system (Verbunt, 1982).

The point where the matter stream from the secondary star meets the accretion disk is called the bright spot (or hot spot in some sources). The bright spot is discussed more in section (1.2.4).

The viscosity of particles in the disk causes most of them to spiral inwards. This is because, according to Kepler's 3rd law (eqn 1.1), particles at smaller orbital radii are orbiting faster than particles at larger radii. The viscous drag between them causes the angular momentum of the faster particles to be transferred to the slower particles which move to a larger radius so that angular momentum is conserved. The inner particles which have lost angular momentum move to a smaller orbital radius. For a review see Papaloizou and Lin (1995). During this process, the gravitational potential energy of the material moving deeper into the gravitational well is released and heats up the disk. The disk is cool in the outer regions but gets hotter closer to the inner rim. Temperatures in the disk range from 30,000K in the inner disk to 5000K in the outer disk (p43, (Warner, 1995b)). These temperatures mean the disk radiates in the ultra-violet to infra-red wavelengths. Only the very inner radius of the disk, called the boundary layer, will be hot enough to radiate X-rays.

The boundary layer

The boundary layer is the region between the white dwarf and the accretion disk. The boundary layer extends from the surface of the white dwarf out to a radius of only $\sim 1.15 R_{wd}$ (Mauche, 1998).

The material in the boundary layer is still travelling at Keplerian velocities much faster than the rotation of the white dwarf. Shocks between particles in the turbulent boundary layer and material impacting on the white dwarf release kinetic energy and raise the temperature of the gas (Pringle and Savonije, 1979). The gas is then hot enough to cool by emitting X-ray radiation. The temperature of the boundary layer reaches $\sim 2 \times 10^8$ K for low accretion rates. The high temperature plasma in the boundary layer is thought to be the main source of X-ray emission in the system (Pringle et al, 1977).

1.1.5 Mass transfer rate

Differences in the matter transfer rate of CVs cause them to have different observable characteristics. There are several sub-categories of CVs which group together systems with similar characteristics. The effects of different mass transfer rates are manifested as differences in the outburst behaviour observed for each system. It is thought that in a nova-like system the mass transfer rate is higher so the system is in a permanent state of outburst. In contrast, dwarf novae have a lower accretion rate so most of the time the system is in a quiescent state. It takes time for enough matter to build up in the accretion disk to cause an outburst. The important systems for this investigation are the dwarf novae rather than the nova-like variables.

Outbursts

When a dwarf nova undergoes an outburst it is thought to be due to a sudden increase in the flow of matter from the disk onto the white dwarf (Osaki, 1974). The disk instability model (for review see Osaki (1996)) attributes this to an increase in the viscosity of the disk as the build up of material in the disk causes it to reach a critical density. Once the critical density is reached, the enhanced viscosity increases the rate of mass flow through the disk and on to the white dwarf. The sudden increase in accretion releases large amounts of energy which heat up the disk. This is seen as an increase in brightness of the accretion disk lasting several days.

The SU UMa type is a subcategory of dwarf novae (Szkody and Mattei, 1984). The SU UMa type have the normal dwarf nova outbursts but they also have regular super-outbursts which are thought to be due to material building up in the disk over the course of several normal outbursts (Whitehurst, 1988). They have short orbital periods of <3 hours. Systems with a higher mass secondary star will also have a longer orbital period. The longer the orbital period, the larger the Roche lobe. We know that the secondary must be just filling its Roche lobe to produce the matter transfer rates and X-ray luminosity observed in SU UMa systems. To have a star that only just fills its Roche lobe when the orbital separation is so small shows that it must be a very low mass star.

1.1.6 Tidal synchronisation

In a close binary system, the gravity of the primary distorts the secondary so it has a tidal bulge. The gravitational attraction of the white dwarf on the bulge will always try to pull it so it is at the closest point between the two stars (fig 1.1).

However, if the binary orbit period and the secondary stars rotational period are not synchronised, the bulge is pulled around the secondary as the stars orbit around each other. The viscosity of the stars convective envelope means that it takes time for the bulge to move to the equilibrium position.

If $P_{rot} > P_{orb}$ the bulge lags behind. If $P_{rot} < P_{orb}$ the bulge will be ahead of the equilibrium point. The viscosity of the stars convection zone prevents the bulge moving freely around the secondary star and means that energy from the binary orbit must be transferred to the star to keep moving the bulge. The secondary gains angular momentum from the CVs orbit and is spun up (Zahn, 1977) while the loss of angular momentum from the orbit causes the stars to move closer together. The viscous dissipation model of tidal synchronisation only applies if the system is already close to synchronisation (Campbell and Papaloizou, 1983). The synchronisation time scale is given by equation (1.2)

$$t \approx r^{-6}q^{-2}(yrs) \qquad (1.2)$$

where q is the mass ratio $q = \frac{M_2}{M_1}$ and $r = \frac{R}{a}$ where R is the stellar radius and a is the orbital semi major axis (Giuricin et al., 1984). The most appropriate equation depends on the theoretical mechanism thought to be causing the viscosity but they all give a similar time scale.

One of the consequences of the secondary star being tidally locked is that one side always faces the white dwarf. The side of the star facing the white dwarf is heated up by the radiation from the boundary layer and white dwarf. The star can be much hotter on the side facing the primary. Some studies have shown that irradiation can cause the properties of emission lines from the secondary star to vary over the course of an orbit. For example, variations in the TiO absorption of Z Cha could be modelled in this way (Brett and Smith, 1993).

The amount of heating due to irradiation depends on the brightness of the boundary layer and white dwarf. Studies have shown that during quiescence these are not as bright and cause little heating of the secondary (Hessman et al, 1984), so as long as the secondary is observed when the system is in quiescence, the effects of irradiation should be negligible. Also, during the eclipse, we see the side facing away from the white dwarf so this would not be affected by irradiation.

1.1.7 CV evolution

Cataclysmic Variables are formed from a binary system that initially contains a high mass star of between $0.95 - 10M_\odot$ (p450,(Warner, 1995b)) and a low mass

6

star. The high mass star evolves much more quickly and ends its life as a white dwarf (Kippenhahn and Weigert, 1990). The low mass star evolves much more slowly so it will still be on the main sequence long after the white dwarf has formed. Just before the primary star forms a white dwarf, it expands to such a large radius that the secondary star orbits within its atmosphere. This is called the common envelope phase (Ostriker, 1976). The atmospheric drag causes the secondary star to spiral inwards and the angular momentum is transferred to the gas surrounding the two stars which can then escape the system (Livio and Soker, 1988). The result is that the secondary star and the newly formed white dwarf are in a much closer orbit than before. The resulting orbital periods of CVs are very short. The typical range is about 1-12 hours (Ritter and Kolb, 2003).

Period Gap

The period of a CV changes over time due to the loss of angular momentum from the system. As the angular momentum decreases, the stars move closer together and P_{orb} also decreases. A plot showing the distribution of orbital periods for a population of CVs shows that there are very few systems with P_{orb} between 2.2 - 2.8 hours (fig 1.2). This has become known as the period gap (Warner, 1976).

This is important to this study because the period gap is thought to be a consequence of the structure of the secondary star and is related to the generation of magnetic fields in the star. In section (1.3) I discuss how the magnetic field of a star is linked to its X-ray luminosity.

The properties of main sequence stars are linked by relationships such as the Mass - Radius relationship and the Mass - Spectral type relationship. Studies have shown that there are similar relationships between the properties of secondary stars (Warner, 1995a). There has been some debate about whether the Roche lobe filling secondary stars in CVs follow the same relationships. The main sequence Mass - Radius relationship did not seem to apply to DQ Her (Smak, 1980) or U Gem (Wade, 1981). However others found good agreement between the predictions of the M-R relationship and the secondaries in HT Cas (Marsh, 1990) and Z Cha (Wade and Horne, 1988). An empirically derived Mass - Radius relation based on data from Webbink (1990) was found to be consistent with the equations for low mass main sequence stars (Warner, 1995a). In equation (1.3) and (1.4) R and M are radius and mass in solar units and (2) shows that these are the parameters for the secondary star.

$$R_{\odot}(2) = M_{\odot}^{\frac{13}{15}}(2) \tag{1.3}$$
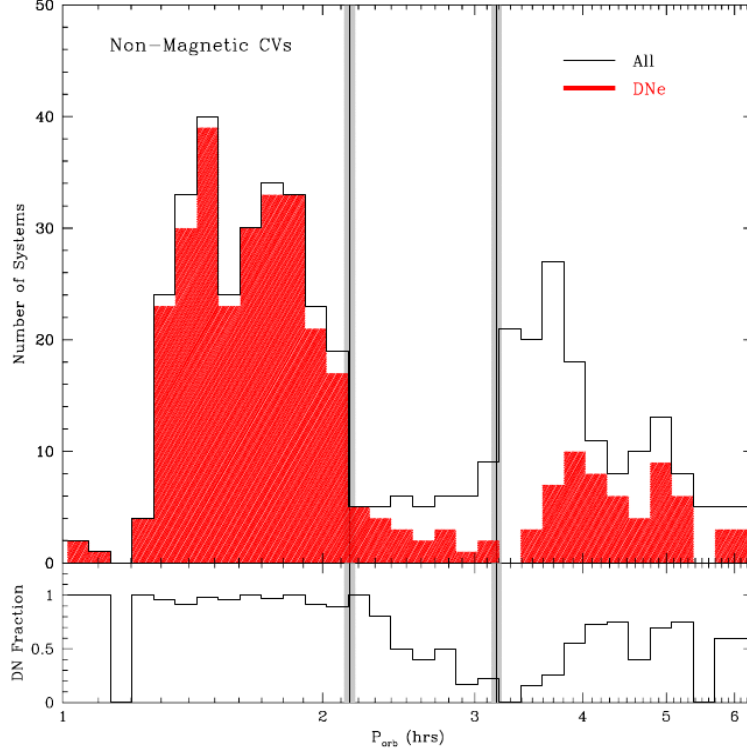
Figure 1.2: The distribution of orbital periods of CVs with the period gap between $P_{orb} \sim$ 2-3 hours. Figure reproduced from Knigge et al. (2011)

.

When combined with Kepler's 3rd law this gives a Mass-Period relation for CV secondaries (Warner, 1995a)(eqn 7).

$$M_{\odot}(2) = 0.065 P_{orb}^{\frac{5}{4}} \qquad 1.3 \leq P_{orb}(hours) \leq \sim 9 \tag{1.4}$$

The influence of the secondary star on CV evolution

The secondary star has a crucial influence on the long term evolution of a CV. The driving force behind the accretion process is the gradual shrinking of the Roche lobe. The shrinking of the secondary star Roche lobe forces matter to spill over the inner Lagrange point. In CVs, the primary star has a much smaller radius and does not fill its Roche lobe so matter only flows one way.

The reason the Roche lobe shrinks is that angular momentum is being lost from the system and the two stars are gradually moving closer together. The loss of angular momentum for CV's above the period gap is due to magnetic braking which is caused by the magnetic field of the secondary star (Huang, 1966).

The effects of magnetic braking are also seen in single stars where in general the older a star is, the slower it rotates. This is because the rate of rotation is reduced over time by magnetic braking (Weber and Davis, 1967). As matter flows away from the star in the stellar wind, it is still under the influence of the stars magnetic field which acts to make the matter rotate with the star. To make the matter rotate out to large distances the star must transfer some of its angular momentum which is then lost as the matter escapes the magnetic field.

In the special case of a tidally locked binary, the loss of angular momentum by the secondary star results in loss of angular momentum from the binary orbit. This is because the loss of angular momentum should cause the star to slow down. However the tidal synchronisation mechanism acts to keep the star rotating at the same rate as the binary orbit. The only way this can happen is if angular momentum from the binary orbit is transferred to the secondary. The end result is that the two stars move closer together to compensate for the loss of angular momentum from the orbit (Paczynski, 1967).

The magnetic braking model also provides an explanation for the period gap. As the secondary continues to lose mass, its internal structure changes. The convection zone becomes deeper until at spectral type $\sim M4$ or mass $\sim 0.2 M_\odot$ (Stassun et al, 2010) the star becomes fully convective. This causes a change in the stars magnetic field (see section 1.3.1) so magnetic braking stops being effective (Rappaport et al., 1983). This has become known as the disrupted magnetic braking model.

The disrupted magnetic braking model explains the period gap because when magnetic braking stops, the loss of angular momentum slows. The stars then stop moving closer together and the secondary stars Roche lobe stops shrinking. This shuts off the mass transfer once the secondary is no longer filling its Roche lobe.

A consequence of the continual mass loss above the period gap is that the secondary star will have a larger radius than expected compared to a isolated main sequence star of the same mass (Knigge et al., 2011)(fig 1.3). The gradual change in mass of the secondary means its radius and spectral type must also change to maintain thermal equilibrium but the stars radius can not shrink as quickly as mass is lost due to magnetic braking. Once mass transfer ceases, the star regains equilibrium and the radius returns to that expected for a main sequence star(fig 1.4).

It is suggested (Knigge, 2006) that CVs below the period gap only loose angular momentum by gravitational radiation which is a much slower process than magnetic braking. This would require that any secondary star below mass $0.2 M_\odot$
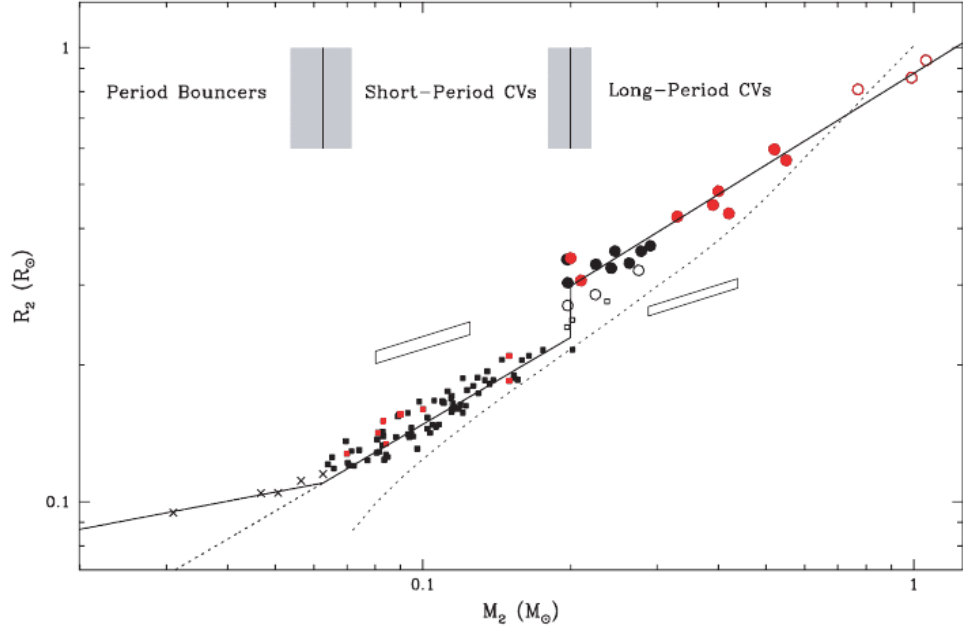
Figure 1.3: Diagram showing the change in the Mass - Radius relation at M = $0.2 M_\odot$ for the secondary stars in CVs. Reproduced from Knigge (2006).

or $P_{orb} \sim 3$ h must have a different magnetic field topology which does not have open field lines connected to the stellar wind.

It is pointed out by Shao and Li (2012) that the angular momentum loss rate below the period gap is still 2.47 ± 0.22 times greater than that expected from gravitational radiation alone. In figure 1.4 the radii of CV secondary stars compared to single main sequence stars of the same mass are shown. It is clear that secondary stars are inflated compared to main sequence stars. Secondary stars at the fully convective boundary ($\sim 0.18 - 0.2 M_\odot$) do have radii similar to those of main sequence stars, but as we move to lower masses, the radii again increase relative to their expected values.

1.2 X-ray emission processes occurring in cataclysmic variables

It is known that CVs are bright X-ray sources e.g.(Rappaport et al, 1974), but the observed X-ray emission of various CVs are very different and there can even be large variations in the X-ray flux detected from the same system over time. Variation in the X-ray emission of CVs can be caused by changes in the rate of accretion onto
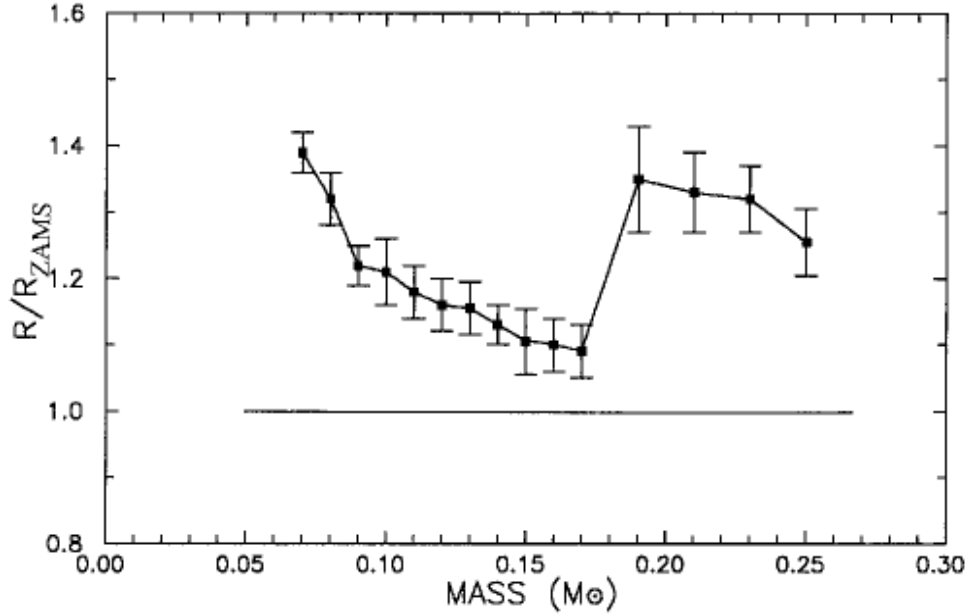
Figure 1.4: Diagram showing how the radii of secondary stars deviate from the values expected from main sequence stars following the M - R relation. Reproduced from Patterson et al (2005).

the white dwarf. There are also a number of other features of the X-ray light curves such as periodic dips and humps which are a result of the changing view we have of the system as the stars orbit each other.

1.2.1 X-ray eclipses of CVs

One reason for the difference in observed X-ray characteristics of CVs depend on the orientation of the system to our line of sight. The inclination of the system is the key parameter and is measured as the angle between the rotational axis of the system and a line orthogonal to the plane of the sky. A system with a low inclination ($\sim 0°$) is seen face on so the white dwarf and boundary layer are always visible so these systems tend to be brighter in X-rays than high inclination systems.

A high inclination system ($\sim 90°$) is seen edge on. The result is that the accretion disk can obscure the X-ray emission from the boundary layer and white dwarf. Also the visibility of the bright spot and secondary star will vary as they orbit the primary star. One of the most obvious features of the light-curve for a high inclination system is that there are periodic eclipses when the secondary star

passes in front of the white dwarf. It is also possible for systems with a slightly lower inclination to exhibit partial eclipses of the white dwarf and boundary layer. The 3 systems studied in this thesis have total eclipses due to their high inclination.

Observing the eclipses in different wavelengths, such as optical or X-ray, can help to identify the region in the system where different types of emission are coming from. For example, it is observed that the X-ray eclipses occur sharply at almost the same time as the optical eclipse of the white dwarf. This indicates that the X-ray emissions are coming from a narrow boundary layer very close to the white dwarf e.g.(van Teeseling, 1997). The duration of the eclipse ingress/egress can be used to calculate the radius of the white dwarf and the total duration of the eclipse gives us the radius of the secondary star if we know the inclination.

Observations of eclipsing systems have shown that the behaviour of the eclipses changes during outburst. The increased accretion causes increased emission from the disk which temporarily dominates the white dwarf, boundary layer and bright spot. Optical eclipses of the disk are still observed, but there are no X-ray eclipses since the secondary star cannot occult the whole disk at once e.g.(Pratt et al, 1999b). During the period between outbursts, known as quiescence, the boundary layer is the main X-ray source and this is small enough be eclipsed by the secondary star.

1.2.2 The cataclysmic variables Z Cha, HT Cas and OY Car

The cataclysmic variables studied in this thesis are Z Cha, HT Cas and OY Car. They are all SU UMa systems with short orbital periods ($\sim 1.5 - 1.7$ hours) below the period gap. They are particularly suited to this study because they are eclipsing systems and have been observed using XMM-Newton.

Eclipses were discovered in the X-ray wavelength for the systems Z Cha, HT Cas and OY Car among others (van Teeseling, 1997), (Wood et al, 1995),(Pratt et al, 1999a) respectively. The X-ray eclipses in quiescence are sharp and coincide with the eclipse of the white dwarf. This shows that the X-ray emission comes from a small region very close to the white dwarf (van Teeseling, 1997).

The fact that they are eclipsing makes them suitable for studying the X-ray emission during eclipse because when the white dwarf and boundary layer are eclipsed, the main source of X-rays is hidden. Any remaining X-rays must come from a different source such as the secondary star, or reflection of the white dwarf and boundary layer emission by other material in the system.

1.2.3 X-ray emissions during the eclipse of OY Car

Two studies have investigated the possibility that X-rays are still visible from OY Car during eclipse (Ramsay et al, 2001) and (Wheatley and West, 2002). The study by Wheatley and West (2002) found that X-rays are still detected during eclipse and they are softer than those detected out-of-eclipse. It was suggested that the softer spectrum points to the possibility of the secondary stars corona being the in-eclipse source. The study by Ramsay et al (2001) also found evidence for X-ray emission during the in-eclipse period with a count rate of $0.024 \pm 0.004 \, \mathrm{ct \, s^{-1}}$ in the energy range 0.1-1.0keV. They investigated the possibility that the source could be the secondary star by comparing the measured X-ray luminosity of the in-eclipse source to the X-ray luminosity expected from a $0.1 \mathrm{M_\odot}$ star. The estimated luminosity for the in-eclipse source was $9 \times 10^{28} \, \mathrm{erg \, s^{-1}}$ in the 0.1-1keV energy range. The X-ray luminosity for a $0.1 \mathrm{M_\odot}$ star was calculated as $L_X < 4 \times 10^{27} \, \mathrm{erg \, s^{-1}}$ (see discussion section 4.2.1). They concluded that the observed in-eclipse luminosity was an order of magnitude too large for a secondary star of $0.1 \mathrm{M_\odot}$ and so this was unlikely to be the source.

1.2.4 Possible sources of X-rays during eclipses

The white dwarf and boundary layer are the main sources of X-rays in a CV and these are both hidden from our view during the eclipse. If they are the only X-ray sources then the system should not be visible during the eclipse in X-ray wavelengths. However, there are several possible scenarios which would cause X-rays to be observable during the eclipse and these are discussed below.

The secondary star

During the eclipse, the secondary star is the only component of the system which is fully visible. It is expected that the secondary star will be spun up and very active so it should be a strong emitter of coronal X-rays (See section 1.3). This makes it a possible source of in-eclipse X-rays.

Scattering

In the scattering scenario, the X-rays emitted by the boundary layer are scattered by material surrounding the binary system. Clouds of ions can absorb X-rays and then re-emit them in all directions. This implies that some of the scattered X-rays could be visible during the eclipse if the scattering region is not too close to the white dwarf. This is illustrated in fig 1.5. A scenario like this has been used to

explain soft X-ray emission from Seyfert 2 galaxies (Awaki, 1997) and the symbiotic star CH Cyg (Wheatley and Kallman, 2006).
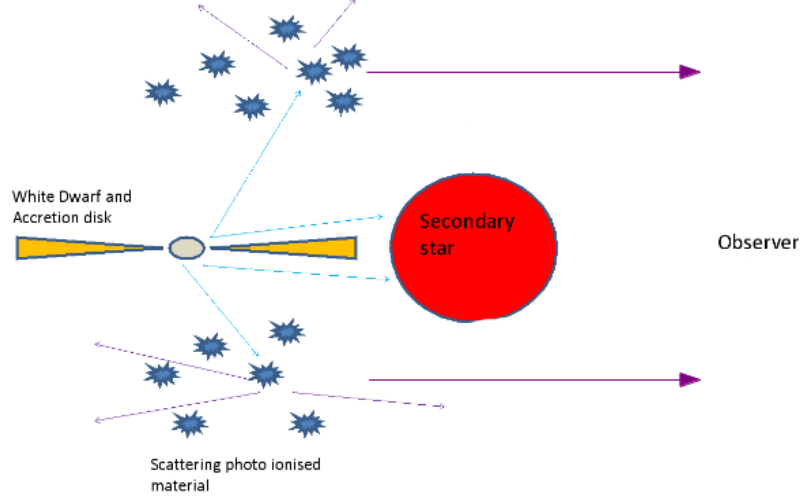
Figure 1.5: Diagram showing how the X-rays emitted from the boundary layer could be scattered into our line of sight by material surrounding the binary system.

This type of X-ray source would have an emission line spectrum with very little continuum because ions can only absorb and emit radiation at certain wavelengths. Scattering by electrons could produce some continuum emission but it is unlikely that the density of electrons would be high enough to make a significant contribution.

The bright spot

The bright spot is where the stream of material from the secondary star impacts the material in the accretion disk (fig 1.6). Gravitational potential energy is converted to kinetic energy as the matter stream falls into the potential well of the primary. This kinetic energy is released by matter as it impacts the disk which causes this region to be optically bright (See review by Livio (1993)).

When viewing high inclination systems, the view of the bright spot changes as we are seeing different parts of the disk at different times in the orbit. This causes a hump in the optical light curve (fig 1.7) as the bright spot moves in to view. The bright spot is also eclipsed by the secondary star but the eclipse happens slightly later than the eclipse of the white dwarf because the bright spot is slightly ahead of the line between the secondary and the white dwarf. The relative timing between the eclipse of the white dwarf and the eclipse of the bright spot is largely dependent

14
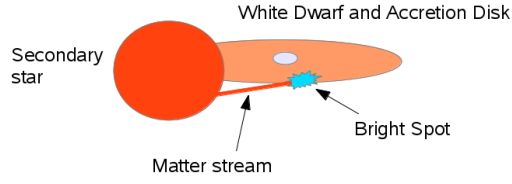
Figure 1.6: Diagram showing how the matter stream from the secondary star impacts the accretion disk and forms a bright spot which emits X-rays.

on the mass ratio of the primary and secondary star.
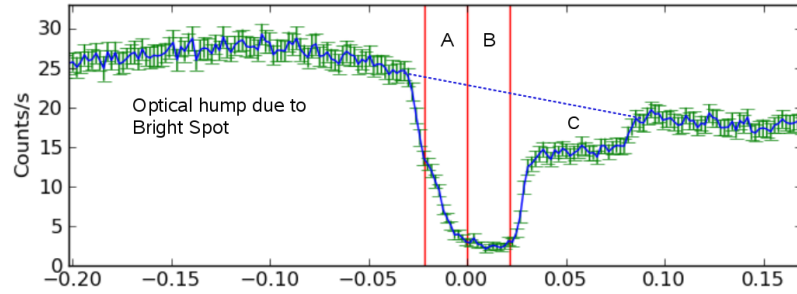
Figure 1.7: The optical light curve of Z Cha (see section 3.5) showing the hump due to the bright spot coming into view (phase -0.2 to -0.025 and the period of the white dwarf eclipse where the bright spot still contributes to the X-ray flux (region A).

The type of optical light curve shown in fig 1.7 has been observed in Z Cha (Warner, 1974), HT Cas (Patterson, 1981) and OY Car (Vogt et al, 1981) among others. The phase marked A is where the white dwarf has become fully eclipsed by the secondary star but the bright spot is still visible. At phase B the bright spot is also eclipsed so any X-rays observed in this period cannot come from the white dwarf, boundary layer or bright spot. After phase B the boundary layer followed by the white dwarf emerge from behind the secondary. Then there is a plateau (region C) where the bright spot is still eclipsed depending on the radial extent of the bright spot. The bright spot may not be a compact region on the edge of the disk. It is possible for part of the matter stream to overflow and impact in different regions of the disk (Lubow and Shu, 1975). The impact can also heat up the disk and produce a bright bulge around part of the rim of the disk (Meglicki et al., 1993).

1.3 X-ray emissions of low mass stars

Estimates of the mass for the secondary stars in CVs (table 1.1) show that they are very low mass stars $\sim 0.1 M_\odot$ of spectral type M. They would be identical to main sequence stars if they were not under the gravitational influence of the white dwarf, which has an affect on the size and shape of the secondary.

As discussed on page 9 the mass of a main sequence star determines its internal structure which in turn has an effect on the magnetic field and other stellar properties. An important change in the structure happens at spectral type $\sim$ M4 or mass $\sim 0.2 M_\odot$ For a review see (Stassun et al, 2010). Stars above this mass have a convective layer on top of a radiative layer while stars of lower mass or later spectral type are fully convective. This transition does not appear to be at an exact spectral type but comes in to effect over the spectral range M3 - M6.

The most important implication for this study is the change in the stars magnetic dynamo since this could affect the X-ray luminosity. Rapidly rotating low mass stars are known to produce magnetic fields which cause coronal activity (Walter and Bowyer, 1981). This implies that secondary stars in CVs would be expected to emit X-rays from the high temperature plasma in the corona.

The secondary star is a potential source of in-eclipse X-rays so I review here the relevant theories of stellar X-ray emission.

1.3.1 Stellar X-ray emission and magnetic activity

Stellar X-ray emission is closely related to magnetic activity in the star. The brighter the X-ray emission, the more magnetically active the stellar source. The magnetic field forms loops which can trap hot plasma and these loops of hot plasma are what makes up a stars corona (Zeilik et al., 1992). It is the high temperature plasma in these loops that emits X-rays. Plasma temperatures of $\sim 10^7$K lead to emission of soft X-rays ~ 0.14 keV. The way that the plasma becomes heated to such high temperatures is not well understood. The general theory is that the magnetic field lines are twisted as they rise to the surface of the convection zone which stores up potential energy in the magnetic field. The magnetic field lines then re-connect in coronal loops so they are no longer twisted and the potential energy is released to heat the corona (Parker, 1983). There are several indicators of magnetic activity occurring in a star. X-rays are an indicator of coronal magnetic activity, while Ca+ emission is an indicator of surface magnetic activity (Frazier, 1970).

Dynamo Theory

According to the stellar dynamo theory e.g. (Belvedere et al., 1980), stellar magnetic fields are generated by the dynamo action of the rotating convection zone. A consequence of this is that the rate of stellar rotation influences the strength of the magnetic field. It is at the interface between the top of the radiative zone and the bottom of the convective shell that the magnetic fields are produced e.g.(Stassun et al, 2010). An important consideration here is that stars below the period gap are fully convective. In this case there is no interface between the radiative and convective zones to generate a magnetic field.

It is possible that an alternative dynamo mechanism operates in fully convective stars which could produce the same magnetic heating effects and X-ray emission as the standard dynamo (Rosner, 1980). The magnetic field in fully convective stars is thought to be a simple dipole rather than having the complex magnetic field structure found in convective shell stars (Gudel and Naze, 2009). Observations of low mass stars later than type M5 have confirmed that they do emit X-rays (Fleming et al, 1993).

Rotation

Many detailed studies e.g. ((Pallavicini et al, 1981), (Pizzolato et al, 2003)) have shown that the level of X-ray emission from stars later than spectral type F is linked to their rotation rate. It was originally thought that the age of a star had an influence on its X-ray luminosity(L_X). X-ray luminosity for isolated main sequence stars decreases with age (Skumanich, 1972). However, it is actually the rotation rate which is directly influencing X-ray emission. A stars rotation rate normally slows down as it ages due to loss of angular momentum through magnetic braking and emission of gravitational waves (Mestel, 1968). While this does lead to a decrease in L_X, it is due to the reduction of the rotation rate and not the age of the star. It is observed that stars that have had their rotation speed increased due to tidal interaction will emit more X-rays than other stars of the same age which have a lower rotation rate. This was observed in the tidally spun up star V471 Tau (Wheatley, 1998). V471 Tau has an X-ray luminosity consistent with younger stars which have the same rotation rate as V471 Tau.

Stars with the same temperature and mass will show different levels of activity depending on the rate of rotation. This implies that if we take two identical stars, then the one that is spinning faster will be more active and show stronger X-ray emission. This correlation is shown to hold for late type (F7-M5) main se-

quence stars (Pallavicini et al, 1981). The activity-rotation relation, based on a large sample of stars, is $L_X \approx 10^{27}(v_{rot})^2\,\mathrm{erg\,s^{-1}}$ where the rotation speed of the star is $v_{rot} = \,\mathrm{km\,s^{-1}}$. However, even for stars rotating at the same speed there can be a large spread in the X-ray flux. This shows that there are other factors involved. The key factor is the convection zone depth. This affects the emission in two ways. 1) The greater rotation speeds at greater depths mean there is a stronger interaction between rotation and convection which generates a stronger magnetic field. 2) In a deep convection zone, the magnetic flux tubes take longer to rise so they have more time to get amplified by the differential rotation (Pallavicini et al, 1981).

The Rossby number

Having shown that the rotation and convection zone depth are the key parameters influencing the magnetic activity of stars later than spectral type F, it is possible to combine these in a single number called the Rossby number (R_0) which can then be used to predict the X-ray luminosity of a star (Noyes et al, 1984). The Rossby number parameterises the convective turnover time (τ_c) and the rotation period of a star (P_{rot}).

$$R_0 = \frac{P_{rot}}{\tau_c} \tag{1.5}$$

The convective turnover time (τ_c) is the time taken for material trapped in the magnetic field at the base of the convection zone to rise to the top of the convection zone. The modified Rossby number ($R_0^{'}$) as described in Pizzolato et al (2003) is given by

$$R_0^{'} = \frac{P_{rot}}{\tau_e} \tag{1.6}$$

where P_{rot} is the rotation period of the secondary star (days). In Pizzolato et al (2003) τ_e is the modified convective turnover time which scales with the mass of the star($M_\odot$) so that for a star of $1M_\odot$

$$log\tau_e = 1.1\mathrm{days} \tag{1.7}$$

For stars rotating slower than the saturation level, the X-ray luminosity is related to the rotation period and convective turnover time by

$$\frac{L_X}{L_{bol}} = C\left(\frac{P_{rot}}{\tau_e}\right)^{-2} \tag{1.8}$$
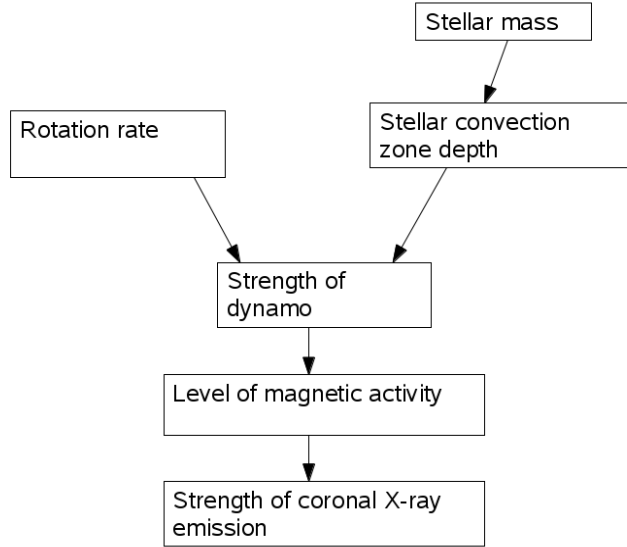
Figure 1.8: The factors involved in the X-ray activity level of low mass stars.

where C is a constant. This relationship between rotation rate and L_X only works up to a point. Observations show that L_X is limited to less than 0.001 times L_{bol} where L_{bol} is the stars bolometric luminosity. In the literature this limit is usually quoted as

$$\frac{L_X}{L_{bol}} \approx 10^{-3} \tag{1.9}$$

When L_X increases to the point where $\frac{L_X}{L_{bol}} \approx 10^{-3}$, the star becomes saturated and the X-ray luminosity will not increase any more however fast the star is rotating (Vilhu, 1984). This limit applies to stars from spectral type G - M (Fleming et al, 1993).

There is some evidence that very rapidly rotating stars may be affected by a phenomenon called Super-Saturation (James et al, 2000). This observation seems to show that stars with very fast rotation rates of $100 - 200 \, \mathrm{km \, s^{-1}}$ actually have L_X levels lower than the normal saturation level of $\frac{L_X}{L_{bol}} \approx 10^{-3}$. This was first observed (Prosser et al, 1996) in a sample of G-K type stars from the Alpha Persei cluster. Other observations (James et al, 2000) showed that this also applied to their observations of M dwarf stars although their sample only included two stars with rotation velocity $\geq 100 \, \mathrm{km \, s^{-1}}$. The secondary stars in CVs with orbital periods less than 2 hours would be expected to be rotating at $\geq 100 \, \mathrm{km \, s^{-1}}$. An overview of the factors involved in stellar X-ray emission is shown in fig 1.8.

The difference between the saturated and un-saturated regime

There are two distinct scenarios for calculating the X-ray emission of late type stars, the un-saturated regime in which L_X increases with rotation velocity and the saturated regime where L_X no longer increases despite an increase in rotation speed. In the saturated case the only parameter that affects the L_X level where saturation is reached is L_{bol} which is directly dependent on the mass and structure of the star (Pizzolato et al, 2003).

The ratio $\frac{L_X}{L_{bol}}$ is a way of comparing the level of X-ray emission of different stars. Scaling the X-ray luminosity by the bolometric luminosity allows us to compare the magnetic activity in stars of different spectral types and hence take account of the mass of the star. While all stars saturate at the level $\frac{L_X}{L_{bol}} \approx 10^{-3}$, the fact that L_{bol} decreases with spectral type means that the level of L_X at this saturation limit must also be lower. The L_X at saturation was found to vary from $L_X = 2 \times 10^{30}$ erg/s for solar mass stars down to $L_X = 2 \times 10^{28}$ erg/s for stars of $0.4\ M_\odot$ (Pizzolato et al, 2003).

The limit where saturation occurs can be defined in different ways. Using the rotation period we can say that saturation occurs at a particular rotation period

$$P_{rot}^{sat} \approx 1.2 \left(\frac{L_{bol}}{L_\odot} \right)^{-\frac{1}{2}} \text{ days} \tag{1.10}$$

Alternatively we can use the modified Rossby number where the saturation limit is $R_0' \leq 0.1$ (Pizzolato et al, 2003).

The period when the star enters saturation increases for lower mass stars. This is equivalent to saying that saturation starts at slower rotational velocities for lower mass stars. This is reflected in equation (1.10) because L_{bol} also depends on the mass of the star. The Rossby number includes the convective turnover time which is dependent on the stars mass so this is already taken into account.

To calculate L_X, we have to choose the appropriate equation depending on whether the star is saturated or not.

$$\frac{L_X}{L_{bol}} \propto R_0'^{-2} \quad \text{or} \quad L_X \propto P^{-2} \quad \text{unsaturated} \quad P_{rot} \geq P_{rot}^{sat} \tag{1.11}$$

$$\frac{L_X}{L_{bol}} \approx 10^{-3} \quad \text{saturated} \quad P_{rot} \leq P_{rot}^{sat} \tag{1.12}$$

(Gudel and Naze, 2009)

We now go on to discuss the way the activity - rotation theory may be applied

to low mass secondary stars and the observational evidence that supports this.

The X-ray emissions of fully convective secondary stars in CVs

To be able to calculate quantities such as the Rossby number and determine whether or not the secondary star should be saturated, we need to know the rotation period of the secondary star. Since the secondary is synchronised to the binary orbit, the rotation period will be the same as the binary orbit period. In the case of eclipsing CVs such as Z Cha, HT Cas and OY Car, the orbital period can be timed by the eclipses.

The short orbital period of CVs means that when the secondary is synchronised, it could be rotating at very high speed. This increased rotation speed enhances the magnetic field in the star via the dynamo mechanism. This in turn could lead to higher X-ray emission than would be observed in a more slowly rotating star.

1.4   Previous studies and aims

1.4.1   Previous studies

Z Cha   Z Cha was first observed by Mumford (1969). The system was later found to be eclipsing in optical wavelengths (Warner, 1974). The length of the eclipse ingress and egress were used to determine the systems parameters (Wood, 1987). This method gives the mass of the secondary star as $0.081 \pm 0.003 M_\odot$ while the mass of the white dwarf is $0.544 \pm 0.012 M_\odot$ which gives $q = 0.14 \pm 0.0035$. Infra red observations detected the secondary star and estimated its spectral type as M5.5 with a mass of $0.125 \pm 0.014 M_\odot$ based on its radial velocity (Wade and Horne, 1988) (table 1.1). The donor masses adopted in this thesis are all taken from Wood (1987) for consistency and are based on eclipse timings.

Eclipsing systems are useful for accurate measurements of orbital period variation as the eclipses provide a reference point in time. A study of the orbital period of Z Cha found that the orbital period is not constant. Analysis of 30 years of observations show that the orbital period is varying sinusoidally (Baptista et al, 2002). This sinusoidal variation has an amplitude of 1.0 ± 0.2min over 28 years so it would have a negligible effect on the observation used in this thesis. The importance of the sinusoidal variation is that it may be due to the magnetic activity cycle of the secondary star (Applegate and Patterson, 1987). Similar sinusoidal variations in orbital period have also been found in HT Cas and OY Car.

X-ray eclipses of Z Cha were first discovered with ROSAT observations which

confirmed the theory that X-rays in CVs mostly come from a narrow boundary layer during quiescence (van Teeseling, 1997).

HT Cas HT Cas has been shown to have eclipses in X-ray wavelengths (Wood et al, 1995). This study showed that the X-ray eclipses occur at times consistent with the optical eclipses. The X-ray source must therefore be on or very close to the white dwarf. This would be consistent with the X-rays being emitted by a boundary layer between the white dwarf and the accretion disk. The measured flux in the 0.1-1.2 keV range was $5 \times 10^{-13} \, \mathrm{erg \, s^{-1} cm^{-2}}$ with a hydrogen column density of $n_H \sim 1.8 \times 10^{20} \, \mathrm{cm^{-2}}$. The spectrum was found to be a good fit with thermal bremsstrahlung at a temperature of $kT \sim 2.4 \, \mathrm{keV}$. The spectrum being consistent with thermal bremsstrahlung is further evidence that the out-of-eclipse X-ray emission is from a hot boundary layer.

A later study (Mukai and Wood et al, 1997) confirmed the detection of X-rays. Detailed study of the depth and width of the eclipse light curve limited the possible extent of the X-ray emitting region to $1.15 R_{WD}$. HT Cas was observed using XMM Newton in 2002. These data were used to carry out a spectral and timing analysis (Nucita et al, 2009). They concluded that the out of eclipse count rate was was 0.56 ± 0.05 counts/s compared to only 0.01 ± 0.02 counts/s, which is consistent with zero, during the X-ray eclipse.

The orbital period of HT Cas is 1.77 hours, but this has been shown to change over time in a similar way to Z Cha and OY Car. HT Cas is thought to follow a sinusoidal ephemeris with a semi amplitude of $\sim 40 \, \mathrm{s}$ over a 36 year period (Borges et al, 2008). The short orbital period of HT Cas places it below the 2-3 hour period gap and indicates that the secondary star is fully convective.

Further information about the secondary star comes from infra-red observations of HT Cas. At infra-red wavelengths the secondary star is no longer dominated by the light from the white dwarf so it can be studied more easily at these wavelengths. The spectral type of the secondary was determined to be $M5.4 \pm 0.3$ based on its TiO band ratio (Marsh, 1990). This study also found that the mass, luminosity and temperature of the secondary star are consistent with values expected for main sequence stars of the same spectral type. The distance to HT Cas was estimated to be in the range 120-230 pc.

Table 1.1: Parameters for the secondary stars in Z Cha, HT Cas and OY Car from the literature (see references column). The numbers in brackets are the error in the last digit.

CV	$P_{orb}(days)$	$M_2(M_\odot)$	$R_2(R_\odot)$	Spectral Type	References
Z Cha	0.07450(1)	0.090(4)	0.155(3)		(Patterson et al., 2005)
		0.089(3)	0.155(1)		(Knigge, 2006)
		0.125(14)	0.172(10)	M5.5V	(Wade and Horne, 1988)
		0.13			(Warner, 1995a)
		0.08	0.16		(Wood, 1987)
	0.074499297(2)				(Baptista et al, 2002)
HT Cas	0.07365(1)	0.090(9)	0.145(5)		(Patterson et al, 2005)
		0.089(9)	0.154(5)		(Knigge, 2006)
		0.09(2)	0.154(13)		(Horne et al., 1991)
		0.13			(Warner, 1995a)
		0.126(20)		M5.4V	(Marsh, 1990)
		0.21(10)			(Zhang et al., 1986)
		0.19(2)			(Young et al., 1981)
	0.073647200(2)				(Borges et al, 2008)
		0.09	0.15		(Wood, 1987)
OY Car	0.06312(1)	0.069(6)	0.126(5)	not available	(Patterson et al, 2005)
		0.065(4)	0.125(3)		(Knigge, 2006)
		0.070	0.13		(Wood, 1987)
		0.11			(Warner, 1995a)
		0.09(1)			(Hessman et al, 1989)
		0.019(1)			(Schoembs et al., 1987)
	0.0631209126				(Greenhill et al., 2006)

OY Car X-ray eclipses of OY Car were first observed by ROSAT (Pratt et al, 1999a). Subsequent observations showed that the X-ray eclipses do not occur when the system is in a state of outburst (Pratt et al, 1999b). Optical observations have shown that there is a lot of absorption due to gas around the OY Car system This phenomenon is called the 'iron curtain' (Horne et al, 1994). This may absorb soft X-rays form the boundary layer (Naylor and La Dous, 1997) due to the high column density of $n_H \sim 10^{22}\,\mathrm{cm}^{-2}$. The secondary star has been detected in the J band and the rotational velocity ($V_{rot}\sin i$) measured spectroscopically as $107.9\pm3\,\mathrm{km\,s}^{-1}$ (Copperwheat et al, 2012).

Distance estimates Table 1.2 shows distance measurements taken from various studies. It is clear that there is a large range of uncertainty in the distance estimates.

Table 1.2: Distance estimates to Z Cha HT Cas and OY Car in parsecs.

Z Cha	HT Cas	OY Car
131 ± 10^{a}	125 ± 8^{d}	121 ± 20^{e}
120 ± 8^{b}	140 ± 12^{d}	82 ± 12^{f}
97 ± 15^{c}	107 ± 6^{d}	-

[a] (Beuermann and Weichhold, 1999)
[b] (Wood et al, 1986)
[c] (Bailey et al, 1981)
[d] (Wood et al., 1992)
[e] (Sherrington et al, 1982)
[f] (Wood et al, 1989)

1.4.2 Motivation

In this thesis I aim to investigate the possibility that residual X-rays are visible during the eclipses of certain cataclysmic variable stars. If the secondary star emits X-rays as expected, then they would only be detectable during the eclipse since they would be very faint compared to the normal boundary layer emission. An investigation of such faint X-ray sources has only become possible since highly sensitive instruments such as the XMM-Newton X-ray observatory have been launched.

If X-rays are still detected during the eclipse then the next aim is to try and determine their source. This could have implications for many areas of research depending on the origin of the in-eclipse X-rays. If they are from the secondary star then this will show that even fully convective low mass stars can produce strong magnetic fields by an alternative dynamo mechanism. It could also provide an

insight into the link between the rotation rate and the X-ray luminosity of low mass stars as well as testing the theory of super saturation.

If the in-eclipse X-ray source is not the secondary star then other possibilities need to be considered. Other authors have suggested that in-eclipse X-rays detected in low mass X-ray binaries could be due to scattering of X-rays by dust surrounding the system (Hyodo et al, 2009). Its has also been suggested that an accretion disc corona may be the source of in-eclipse X-rays detected in OY Car (Ramsay et al, 2001).

Chapter 2

Observations

2.1 The XMM - Newton satellite

The X-ray Multi Mirror telescope (XMM-Newton) (Jansen et al., 2001) is a space based X-ray observatory launched by the European Space Agency in 1999. X-rays can only be observed in space as they are absorbed by the Earth's atmosphere before they can reach a ground based detector. The satellite has 3 CCD cameras for detecting X-rays as well as 2 reflection grating spectrometers and an optical monitor (OM). The 3 X-ray cameras together are called the European Photon Imaging Camera (EPIC). The cameras are individually referred to as pn, MOS1 and MOS2. The pn camera uses a pn CCD and the MOS cameras use metal oxide semiconductor CCDs. Three separate telescopes focus X-rays onto the EPIC cameras. Normal optical mirrors and lenses do not work for X-rays because of their high energy. In order to focus the incoming X-rays, X-ray telescopes use a tube called a grazing incidence mirror which deflects incident X-rays onto the CCD. The mirrors are coated with gold and are in the shape of a paraboloid followed by a hyperboloid (fig 2.1).

In the two MOS telescopes, half of the incident X-rays are diverted to the reflection grating spectrometers. This means the pn camera receives twice as much X-ray flux as the individual MOS cameras. The EPIC cameras can detect X-rays with energy in the range 0.15-12 keV. The X-rays are detected when an X-ray photon interacts with a silicon atom in the CCD chip. This releases a number of electrons proportional to the energy of the incident X-ray. The electrons are then sent to a readout node.

The Optical Monitor (OM) can take observations of the target at the same time as the X-ray telescopes are operating. The OM covers the wavelength range 170nm - 650nm which is the ultra violet to optical range. The telescope has a
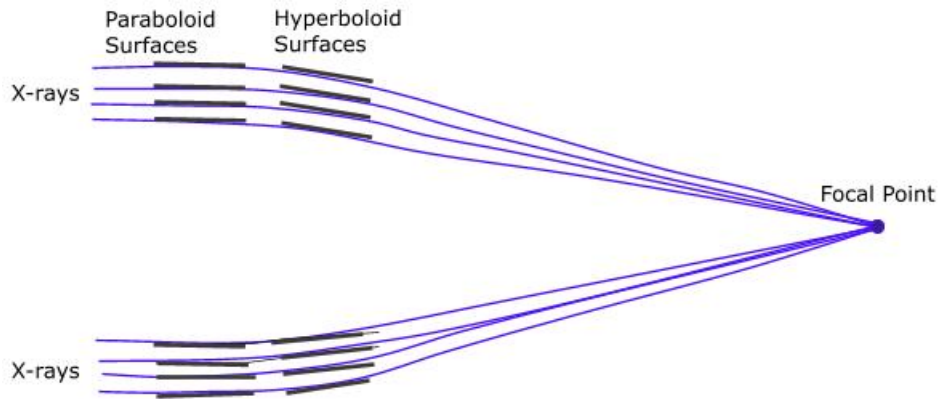
Figure 2.1: Arrangement of X-ray mirrors in each of the 3 telescopes in XMM-Newton. (Image from (NASA XMM-Newton pages))

Ritchey - Chretian arrangement of mirrors which focus onto a CCD detector (XMM Newton Users Handbook, 2011).

Main features of the instruments

The pn camera has 12 CCD chips arranged in 2 rows of 6, where the nominal target position is on CCD number 4. The MOS cameras each have 7 CCDs each arranged with 6 of the CCDs surrounding one main CCD at the centre. The pn camera has a faster readout time so it can collect data with a better time resolution than the MOS cameras (table 2.1). The time resolution of CCD instruments is limited because the CCD must be read out to record the events. The time when the CCD is collecting photons is the integration time, but after the integration, it takes some time to read out the CCD. During the read out, any photons that are incident on the chip will not be recorded.

The CCD must be read out before the photons pile up. Pile up is when more than one photon hits the same pixel and release more electrons. When the CCD is read out, this will be interpreted as one high energy X-ray since there is no difference between the electrons released by one high energy X-ray or several lower energy X-rays. This would lead to unreliable spectral data since the data would record proportionally more hard X-rays and less soft X-rays than were actually emitted by the source. To reduce the effects of pile up when observing bright sources, a shorter time interval between read outs is used so that less photons have time to accumulate.

Both types of instrument can be operated in different modes. The different modes work by only reading out the part of the main CCD where the source is

27

Table 2.1: Time resolution for EPIC cameras in different modes

Mode	pn Time Resolution(ms)	MOS Time Resolution(s)
Full frame	73.4	2.6
Large window	48	0.9
Small window	6	0.3
Timing mode	0.03	1.5(ms)

located. In full frame mode, the entire CCD is read out. In partial window mode only a portion of the CCD is read out which saves time reading out the CCD and allows smaller gaps between integrations. These modes can be used to prevent pile up for bright sources and also to improve time resolution by sacrificing some of the image data. The time resolution for each camera in different modes is shown in table 2.1 (XMM Newton Users Handbook, 2011).

Data preparation and software

There are a number of background X-ray sources and instrumental characteristics which can cause the recorded data to differ from a true representation of the observed X-ray source source. These contaminating effects must be taken into account when interpreting data to find out more about the source.

Serious contamination can come from soft proton flares as the satellite passes through clouds of protons in the magnetosphere. When these protons interact with the CCDs they produce a signal as if they were incident X-rays. Extracting a light curve in the 10-12 keV range reveals whether the observation has been affected by background flares (fig 3.1-3.3). Any time intervals where there is a high count rate in this energy range indicate there was a solar flare, and if necessary, these time intervals can be removed from the observation.

Another factor to be taken into account is the contribution of background X-rays. Background X-rays are due to unresolved cosmic sources. Background X-rays and proton flares can be corrected for by extracting a light curve from a region of sky with no X-ray sources. This background light curve is then subtracted from the source light curve to give the background subtracted light curve. The region the background light curve is extracted from is preferably from the same CCD chip where the source is detected so that the characteristics of the detector should not be too different between the source and the background region. It is also better to use as large an area as possible to extract the background to reduce the error in the background measurement. Background noise can also come from electronic defects

such as hot pixels and each chip in the CCD has slightly different characteristics.

Science Analysis Software (SAS)   The XMM-Newton Science Archive (XSA) is an on-line database of all observations made with the XMM-Newton satellite. The data from the XSA can be downloaded in the form of an Observation Data File (ODF) which contains the data from all the instruments. Some processing must be done to prepare the data and produce the files needed for images, light curves and spectra. This was done with the Scientific Analysis Software (SAS) (de la Calle et al, 2011). Information needed to calibrate all XMM observation files is contained in the Current Calibration File (CCF). Firstly a Calibration Index file (CIF) was generated to link the ODF file to the specific files in the CCF which apply to this observation. This was done with the task 'cifbuild'. The task 'odfingest' was run to produce a summary of all the files in the ODF. This summary file '*SUM.SAS' was used by SAS whenever tasks were run.

The next stage is to produce event files. These are the most fundamental files which contain all the information about each photon that was detected such as position, time and energy. For the PN instrument the task 'epproc' was used. For MOS 1 and 2 it was 'emproc'. These event files were used to produce images, light curves and spectra. The preparation of the optical monitor data will be discussed in section (3.4).

A correction must be made to the event files to adjust the time of arrival for each photon. This is because the movement of the XMM satellite around the solar system has an effect on the arrival times. This was corrected with the task 'barycen' which was run on all PN and MOS event files. This does a barycentric correction which adjusts the photon arrival times to the time they would be if the satellite was always at the barycentre of the solar system. The barycentre is the centre of mass of the solar system.

Detector characteristics   The quantum efficiency of the detectors is a measure of how many of the incident photons will actually be detected. The quantum efficiency of the CCD detectors varies with the energy of the incident photons so the observed spectrum is not exactly the same as the spectrum emitted by the source. For example the source spectrum may have a higher proportion of soft photons, but if the detector is not as efficient in the soft X-ray range compared to the higher energy range, then the detected spectrum will have proportionally fewer soft X-rays. When carrying out spectral analysis, the quantum efficiency characteristics of the detector are used to calculate the spectrum that would be detected if a model X-ray source

was observed. This is achieved by generating an Ancillary Responce File (ARF) using the SAS task 'arfgen' which contains all the information needed to correct the data.

Another effect which must be corrected for is energy redistribution. This is due to the variation in the response across different regions of the CCDs. Some regions of the CCDs will be slightly more or less sensitive than others and will respond differently to different energy photons. This is corrected using a Redistribution Matrix File (RMF) generated by the SAS task 'rmfgen'. This file describes the response of each CCD as a function of energy and channel and the data can be corrected accordingly.

When carrying out spectral analysis using XSPEC (Arnaud, 1996), the data was corrected with the RMF and ARF files to calculate the spectrum that would have been observed free of instrumental effects. This was then compared to model spectra to see if there is a match between the model and the observed source.

2.2   The Observations

In this thesis I consider XMM-Newton observations of Z Cha, HT Cas and OY Car (table 2.2), which are available in the XMM-Newton Science Archive (de la Calle et al, 2011). Observation 0306560301 for Z Cha was taken during an outburst and the X-ray light curve does not show any eclipses. For this reason observation 0306560301 was not used for this analysis. There was also a problem with observation 0152490201 for HT Cas. There was a lot of background flaring during the observation and inspection of the light curve shows many gaps in the data. This makes it unreliable for measuring the in-eclipse count rate so this observation was not used. The observation IDs for the three observations used in this analysis are Z Cha (0205770101), HT Cas (0111310101) and OY Car (0099020301).

Z Cha was observed using XMM on 19/20th December 2003 for a period of 101ks covering 16 eclipses. The MOS cameras were operated in imaging mode during the same period. There is also an observation from the OM covering 15 eclipses in fast mode.

HT Cas was observed for   ∼59ks on 20th August 2002 and 7 eclipses were observed. These are seen in in all 3 cameras and the optical monitor although the optical observation only covers 3 of the eclipses.

OY Car was observed on 29th June 2000 for 61ks and 10 eclipses are seen in both the pn and MOS cameras. Unfortunately the OM was only operating for a short time and captured one eclipse.

Table 2.2: Observations taken from the XSA archive.

Object	Obs ID	Start Date	Time	length (s)	PI
Z Cha	0205770101	19-12-2003	21:07:14	101417	Dr Peter Wheatley
Z Cha	0306560301	30-09-2005	01:44:29	88953	Dr Peter Wheatley
HT Cas	0111310101	20-08-2002	09:47:41	59852	Dr Michael Watson
HT Cas	0152490201	12-07-2003	07:57:59	55339	Dr Peter Wheatley
OY Car	0099020301	29-06-2000	23:28:29	61427	Prof Keith Mason

Table 2.3: The 3 main observations used in the analysis. "ff" means full frame mode.

	Position		Instrument Mode			Number of Eclipses
	Ra	Dec	pn	MOS 1 & 2	OM	
Z Cha	08:07:27.75	-76:32:00.7	ff	imaging	fast	16
HT Cas	01:10:13.13	+60:04:35.4	ff	imaging	fast	7
OY Car	10:06:22.07	-70:14:04.6	ff	imaging	fast	10

Chapter 3

Analysis

3.1 Identifying X-ray eclipses

To identify the times of the eclipses in the data, the first stage was to identify which observations have X-ray eclipses since it is the eclipses we are primarily interested in. I determined the usefulness of the data by extracting a full light-curve from the PN data which showed if eclipses were present (fig 3.1-3.3). To make the full light-curve for each observation, an image was made from the PN event file to see which region to extract the source light-curve from. The images were extracted using 'evselect' and displayed with the ds9 image viewer.

For Z Cha in fig 3.4 the source was clearly visible at co-ordinates (08:07:27.75, -76:32:00.7) which match the Ra/Dec co-ordinates for Z Cha given by the Ritter & Kolb catalogue (Ritter and Kolb, 2003). The light-curve was extracted from a circular region, centred on the source, which has a radius of 25 arc seconds to contain the main source but not include any other bright sources.

The extracted light curves for Z Cha, HT Cas and OY Car are shown in figures 3.1-3.3. One of the Z Cha observations (0306560301) shows no eclipses due to the system being in outburst. The observations which have eclipses and are suitable for further investigation are Z Cha (ID 0205770101), HT Cas (ID 0111310101) and OY Car (ID 0099020301).
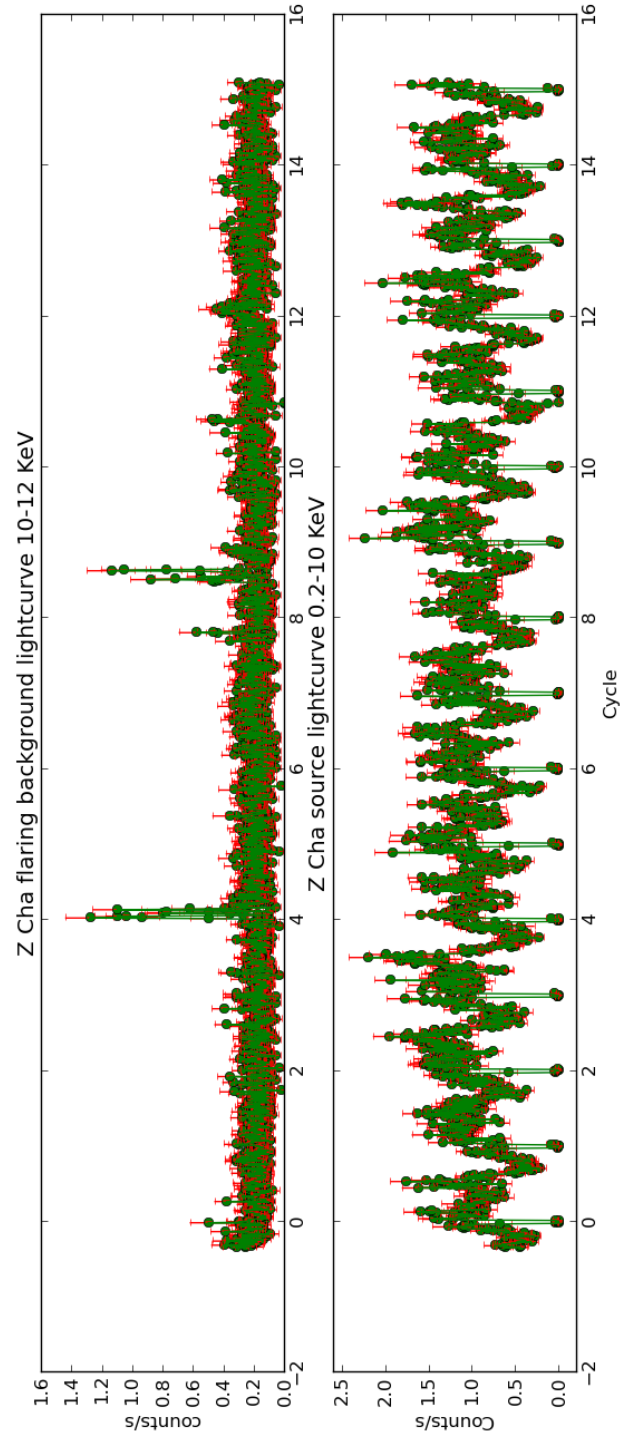
Figure 3.1: Full light-curve for the Z Cha observation(OBS ID:0205770101).The background light curve in the 10-12keV range (top) and the source light-curve showing the eclipses in the 0.2-10keV range (bottom).
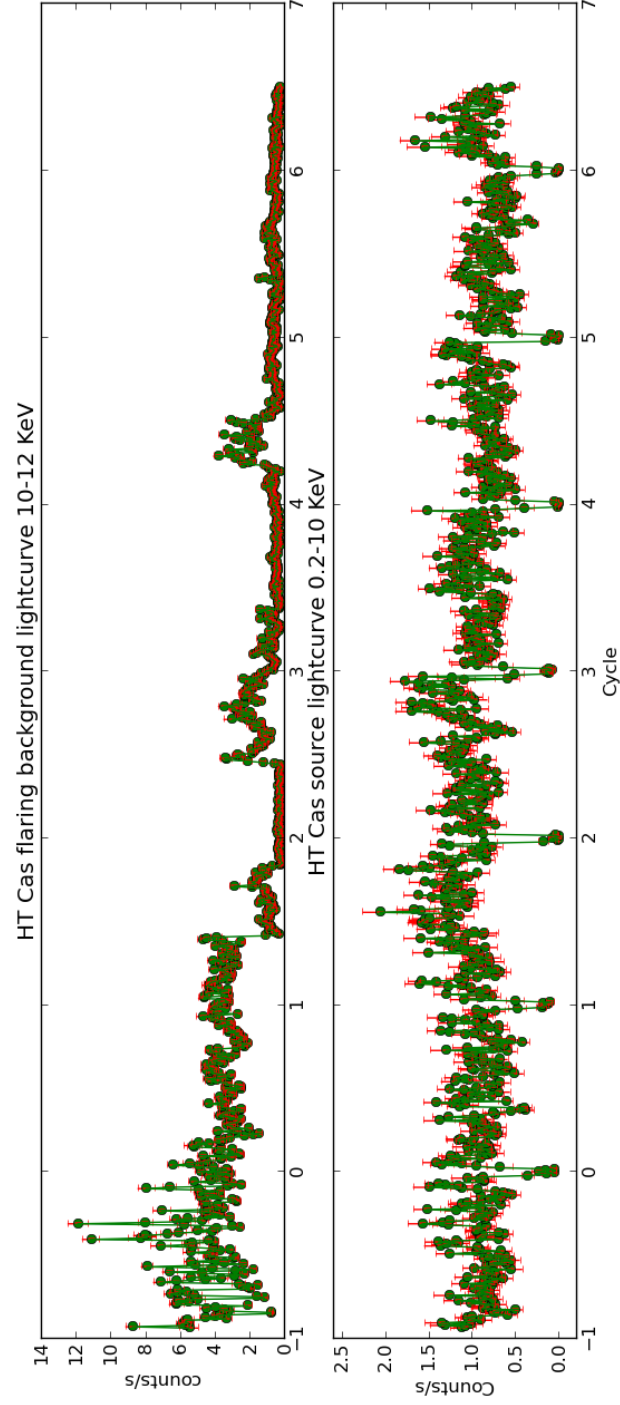
Figure 3.2: Full light-curve for the HT Cas observation(OBS ID:0111310101).The background light curve in the 10-12keV range (top) and the source light-curve showing the eclipses in the 0.2-10keV range (bottom).
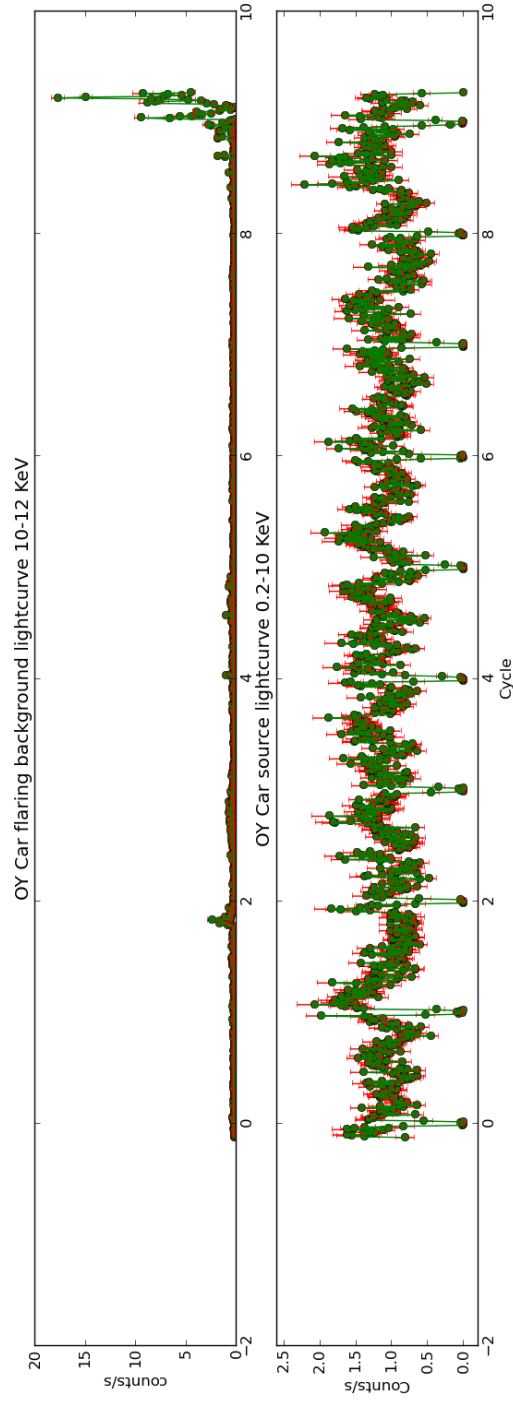
Figure 3.3: Full light-curve for the OY Car observation(OBS ID:0099020301).The background light curve in the 10-12keV range (top) and the source light-curve showing the eclipses in the 0.2-10keV range (bottom).

The next stage was to isolate the time intervals when the system was in eclipse. The light curves are very variable on time-scales of seconds so it is hard to see exactly where an eclipse starts and ends. This was improved by folding the light curve on the orbital period so that all the eclipses line up on top of each other.

The process of folding a light curve creates a plot of all the eclipses on top of each other. This makes the shape of the eclipses easier to see as there are more data points per phase value. The light curve can also be improved by binning the data so that each data point on the light curve is the average of all the events within that phase bin. I wrote a python program to bin up the light curves with a bin width of 0.0019 cycles. This reduces the effects of noise which distort individual eclipses.

The light curves were folded using the time of the mid point of the first eclipse 't0' as a reference point so that each photon has a phase value between -0.5 and +0.5 with t0 being at phase 0. The time for the mid eclipse point of each subsequent eclipse was calculated by adding the orbital period (seconds) to t0. The orbital periods used were taken from the literature. For Z Cha there are regular eclipses every 6436.7 seconds (Baptista et al, 2002), which is about ~ 107 mins. The HT Cas and OY Car observations also show these regular X-ray eclipses. HT Cas has a period of 6363 sec (Borges et al, 2008) and OY Car 5453 sec (Greenhill et al, 2006). The published ephemerides were not used because the sinusoidal variation in the orbital period of these systems means that the observed eclipse times can vary from the calculated eclipse times by up to 10 seconds. This is because the ephemeris is calculated as the best fit to 30 years worth of data but is not necessarily the best estimate of t0 for a particular data set. For this reason I selected the time for t0 visually based on the data set I was using and checked that the mid eclipse times calculated from it lined up with the mid point of each subsequent eclipse.

The folded and binned light curves are shown in fig 3.5. The phase values chosen to mark the beginning and end of the in-eclipse phase are marked A and B. A slight gap was left after the ingress and before the egress to ensure that no X-rays from the white dwarf or boundary layer contaminated the in-eclipse observations. An in-eclipse event file was extracted from the time period between A and B which only contained X-ray events recorded during total eclipse. The method of extracting the in-eclipse event files is described in detail in section (3.2). The light curves produced from these event files are referred to as the in-eclipse light curves.

3.2 Detection of the X-ray sources during eclipse

The next stage was to find out if there were any X-ray sources visible during the eclipses. This was done by producing an image from the in-eclipse event file. If there was still an X-ray source present during eclipse then it would be visible in this image.

Figure 3.4 compares the in-eclipse and out-of-eclipse images for Z Cha , HT Cas and OY Car. The images show that a source was detected during the in-eclipse periods for all 3 observations. Images made using only high energy ranges ($\sim 2 - 10\,\text{keV}$)show the out-of-eclipse source but not the in-eclipse source. This shows that the in-eclipse source may be softer than the out-of-eclipse source. The in-eclipse images in fig 3.4 show the energy range 0.2-2 keV. The in-eclipse source is circled and the circle also indicates the region used to extract in-eclipse source light curves.

3.2.1 Separating in-eclipse and out-of-eclipse time periods

To compare the in and out-of-eclipse sources, it was necessary to extract light curves from the correct time intervals. The in-eclipse light curve should only contain time intervals where the source was fully eclipsed to avoid contamination from when the source was only partially eclipsed. The out-of-eclipse light curves were extracted from time intervals where the source was fully visible and an eclipse had not yet started.

There is also the problem that CVs are very variable over the course of the orbit as different parts of the system come in to view. For this reason, the intervals used for the out-of-eclipse light-curve were located either side of the eclipse. This means the source, as it appeared during eclipse and out-of-eclipse, was compared at as close as possible to the same time.

To allow direct comparison, the time intervals from which the out-of-eclipse event files were extracted were set to be the same length as the in-eclipse intervals. Figure 3.5 shows the time intervals selected from each observation. The C-D and E-F intervals were combined to make the out-of-eclipse intervals the same length as the in-eclipse(A-B) interval.

The D and E phase values for each observation were selected from the folded light curves so that they were well clear of the ingress/egress periods. The C and F phase values were then calculated from the D and E values respectively so that the interval each side of the eclipse would be half as long as the in-eclipse interval.

The selected time intervals were used to create new event files for each obser-
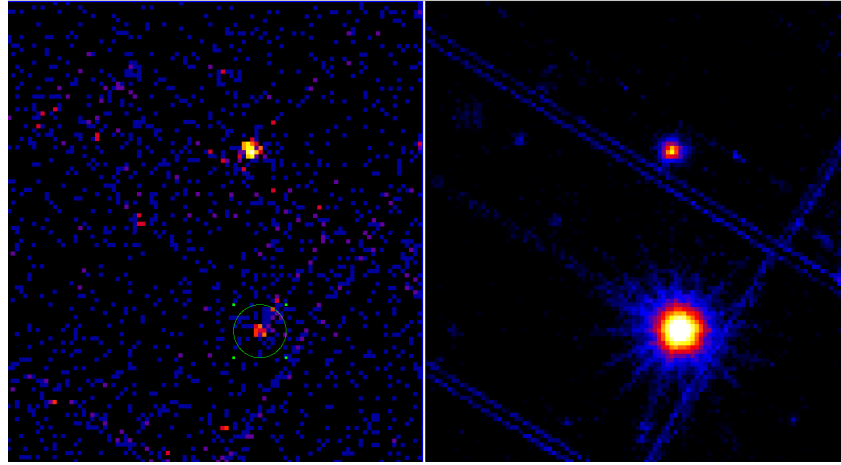
(a) Z Cha
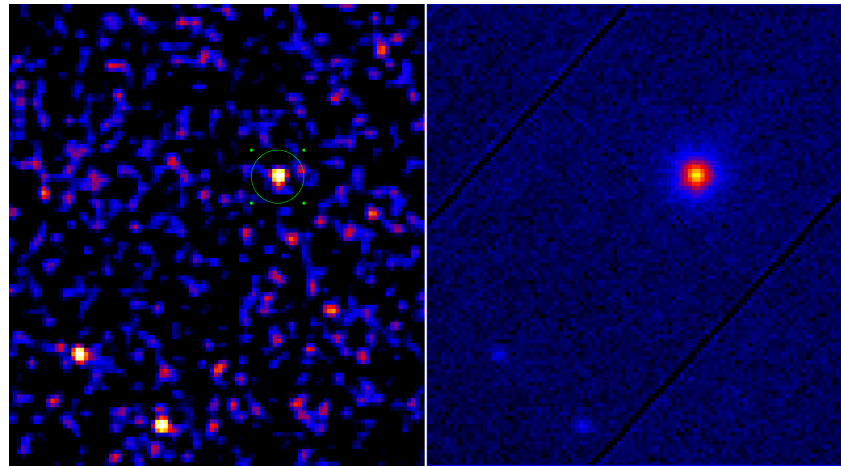
(b) HT Cas
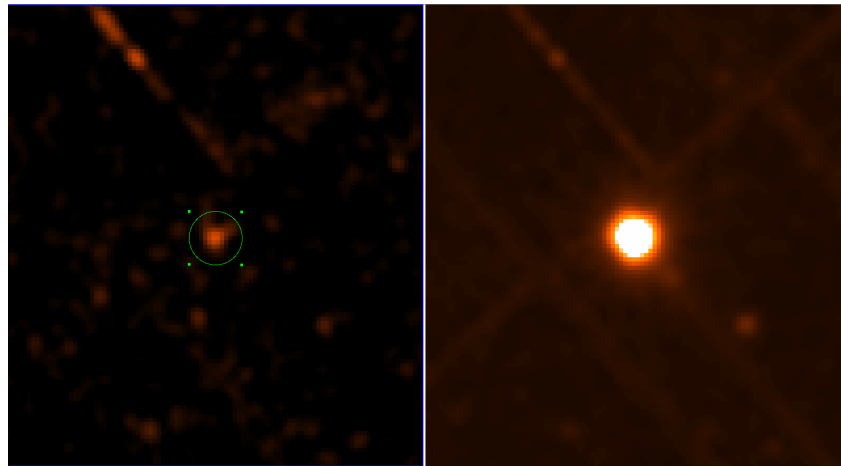
(c) OY Car

Figure 3.4: Z Cha, HT Cas & OY Car in-eclipse image from the PN camera in the 0.2-2keV energy range(left) and out-of-eclipse image (right).
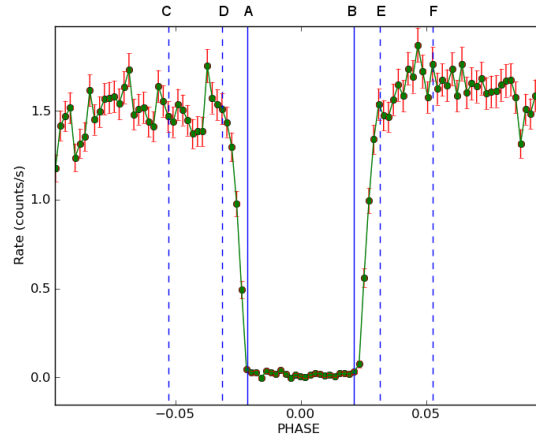
(a) Z Cha
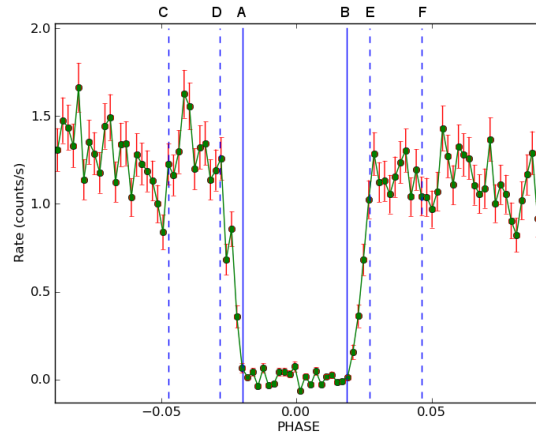
(b) HT Cas
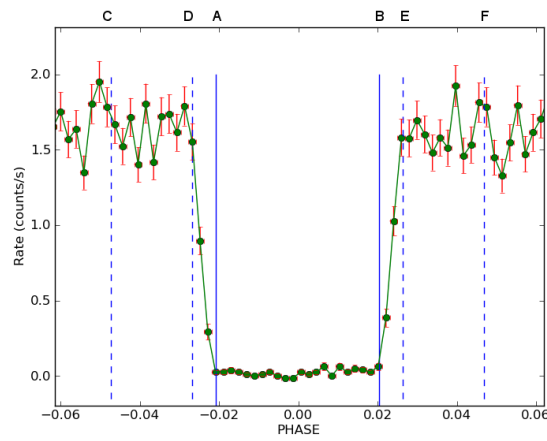
(c) OY Car

Figure 3.5: Z Cha, HT Cas & OY Car in-eclipse and out-of-eclipse phase ranges.

vation. For each observation I created two event files. One containing only in-eclipse events and the other for out-of-eclipse events. These were created from the original event file for each observation by filtering it using a good time interval (GTI) file. The time values calculated from the A,B,C,D,E,F phase values were used with the SAS tool 'tabgtigen' to produce the GTI files. The GTI files were then used with 'eveselect' to produce new event files containing only the selected time intervals.

The in-eclipse and out-of-eclipse event files form the basis for the analysis in each of the following sections. In section (3.3) they are used to calculate the total counts for each in-eclipse and out-of-eclipse interval. In section (3.4) they are used to calculate the total counts detected in various energy ranges. For section (3.5) X-ray light curves from the filtered event files were extracted using 'eveselect'. In section (3.6) they were used to extract X-ray spectra.

3.3 Comparing the variability of the sources

In the previous section I showed that an X-ray source is still detected during the eclipse for all 3 systems. I now investigate whether X-rays detected during the eclipses have the same origin as the X-rays detected out-of-eclipse. It is possible that material in the system reflects the X-rays produced by the boundary layer so that some are still visible during the eclipse. This would mean the in-eclipse and out-of-eclipse X-rays are produced by the same source. It is also possible that the in-eclipse X-rays are produced by a different source independently of the boundary layer emission. This could be from a range of possible sources such as the corona of the secondary star or the bright spot where the matter stream impacts the disk.

In this section I test the variability of the in-eclipse source and compare it to the variability of the out-of-eclipse source. If the in-eclipse X-rays are actually boundary layer X-rays reflected by material in the binary system, then we would expect the brightness of the in-eclipse and out-of-eclipse source to vary in unison over the same time period. This is assuming that the time it takes for the light to travel to the reflecting material is small compared to the variability time-scale. If they do not vary in unison then this would indicate that they are independent and the X-rays have a different origin.

The energy range used was 0.2-10 keV. The circle regions used were the same as for the full light curves in section (3.1). Light curves for the in-eclipse and out-of-eclipse sources were extracted from the filtered event files as described in section (3.2.1). A python program was used to bin up the light curves so that all the events from one eclipse go into one bin. When operating on the out-of-eclipse light-curve,

the events come from two time intervals, one either side of the eclipse. In this case the events from both intervals were combined in to one bin. The total number of counts was calculated for each bin. This means that for each eclipse we got a total number of counts during the eclipse and a corresponding number for the out-of-eclipse counts. This was repeated for all 3 instruments and the results combined to get the final totals.

Background light curves were extracted from the same energy ranges and time intervals. The extraction region was made up of multiple circles arranged on the same CCD as the target source but positioned so that they were not contaminated by any other sources. This gave a much larger region to extract the background light curves which reduces the error in the background count. The number of background counts in each light curve was scaled to what it would have been if the background and source regions were the same size. The scaled background counts were then subtracted from the source counts. The SAS task 'epiclccorr' was not used for the background subtraction because it also does other corrections which artificially add counts to the final number detected to compensate for vignetting and the quantum efficiency of the detector. Instead, the background counts were subtracted separately.

The variability of the source

First I investigated whether each source is variable or not. This was tested by comparing the average count rate for each eclipse against the average count rate for all the eclipses in an observation. For all the sources, the individual eclipses vary around the average value. However, it is necessary to check whether this is just fluctuation due to noise or whether the count rate really is changing from one eclipse to the next.

The chi-square (χ^2) test was used to check if the variation of the source from one eclipse to the next is significant. The formula used was

$$\chi^2 = \sum \frac{(X_i - M_i)^2}{\sigma_i^2} \tag{3.1}$$

where X_i is the total counts in each eclipse bin and M_i is the average of all the bins. σ_i is the error in each value of X (Lampton et al., 1976). The test was used separately for the in-eclipse data and then the out-of-eclipse data.

The results of the χ^2 test (table 3.1) show that for all 3 observations the out-of-eclipse source is not well correlated with the average and is therefore very variable. The in-eclipse sources showed no detectable variability.

Table 3.1: Results of χ^2 to test the variability of the sources from their mean value over the course of each observation.

	Z Cha		HT Cas		OY Car	
	IN	OUT	IN	OUT	IN	OUT
average counts/s	0.020	1.99	0.022	1.579	0.031	1.996
reduced χ^2	1.79	10.52	0.81	14.75	0.94	4.4
d.o.f.	15	15	6	6	9	9
null hypothesis %	2.9	0	56.6	0	48.6	0

The low count rate for the in-eclipse data means that low amplitude variability can not be ruled out due to the large error ranges in the average count rate for individual in-eclipse data points. However, large scale variability can be ruled out. This analysis does show that the out-of-eclipse sources are very variable.

The in-eclipse count rates compared to the out-of-eclipse count rates

Next I compared the in-eclipse and out-of-eclipse light curves together to see if they vary in unison or not. The count rate from the in-eclipse bins is always much lower than for the out-of-eclipse bins so the counts/s for each bin have been rescaled in fig 3.6 and 3.7. The count rate was rescaled by taking the average of the in-eclipse count rates and dividing each data point by the average so that they vary around 1. The same procedure is repeated for the out-of-eclipse data points so both sets of data are rescaled to 1. This allows a clear comparison of the count rate in each eclipse. To calculate χ^2 for this test I used the formula

$$\chi^2 = \sum \frac{(x_i - y_i)^2}{\sigma_i^2} \tag{3.2}$$

Table 3.2: The results of comparing the variability of the in-eclipse and out-of-eclipse source for each observation. A χ^2 value close to 1 indicates that the data is consistent with the in-eclipse and out-of-eclipse sources varying in unison. However, the reduced χ^2 result for Z Cha is 2.02 which is not consistent with them varying in unison.

	Z Cha	HT Cas	OY Car
no of eclipses	16	7	10
reduced χ^2	2.02	1.02	0.90
d.o.f.	14	5	8
null hypothesis %	1.27	40.5	51.7
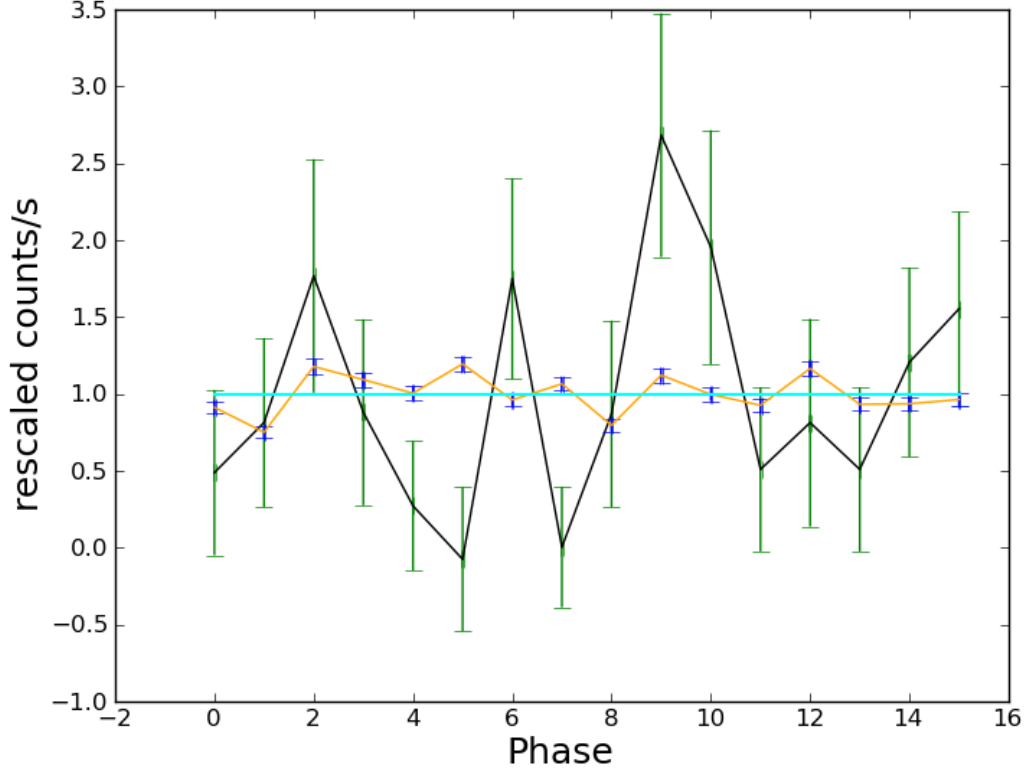
Figure 3.6: The variability of the in-eclipse source compared to the variability of the out-of-eclipse source for Z Cha. In-eclipse (black) and out-of-eclipse (yellow)

where x_i is the total counts measured during an eclipse, y_i is the total counts measured during the corresponding out-of-eclipse period and σ_i^2 is the error in the difference $(x_i - y_i)$. This was repeated for each eclipse to find the sum (χ^2). The reduced Chi-square is given by

$$X_\nu^2 = \frac{\chi^2}{N - 2} \tag{3.3}$$

where N is the number of in and out-of-eclipse data points and it is -2 because the in-eclipse and out-of-eclipse average values each use one degree of freedom.

The results show that for Z Cha the variability of the sources is not well correlated since the reduced χ^2 is 2.02 . The in-eclipse source shows no detectable variability although there is a large error range on individual data points. There is no obvious correlation between the change in count rate from one eclipse to the next and the corresponding out-of-eclipse count rates. However, the large decrease in the signal to noise ratio between the out-of-eclipse and in-eclipse data may limit

Figure 3.7: The variability of the in-eclipse source compared to the variability of the out-of-eclipse source for HT Cas and OY Car.
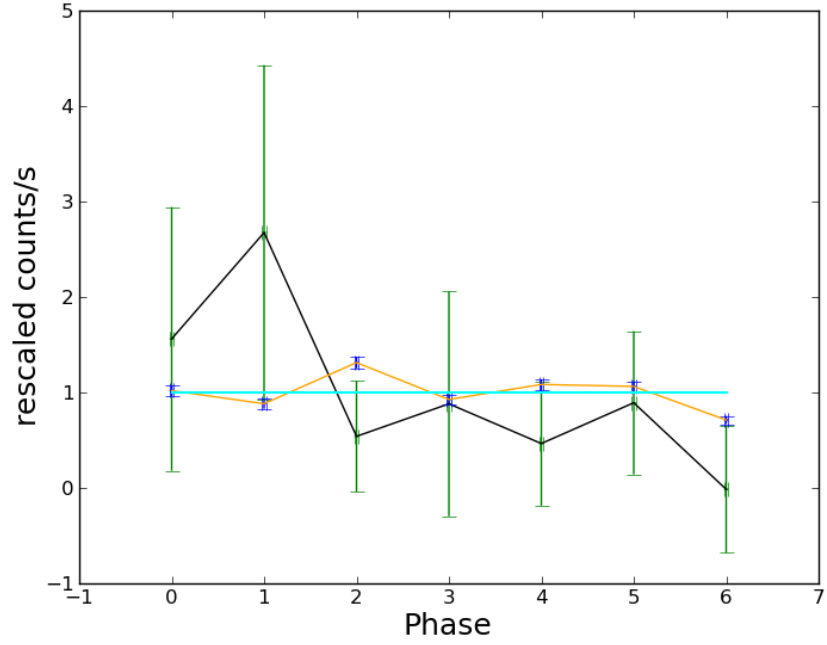
(a) HT Cas In-eclipse (black) and out-of-eclipse (yellow)
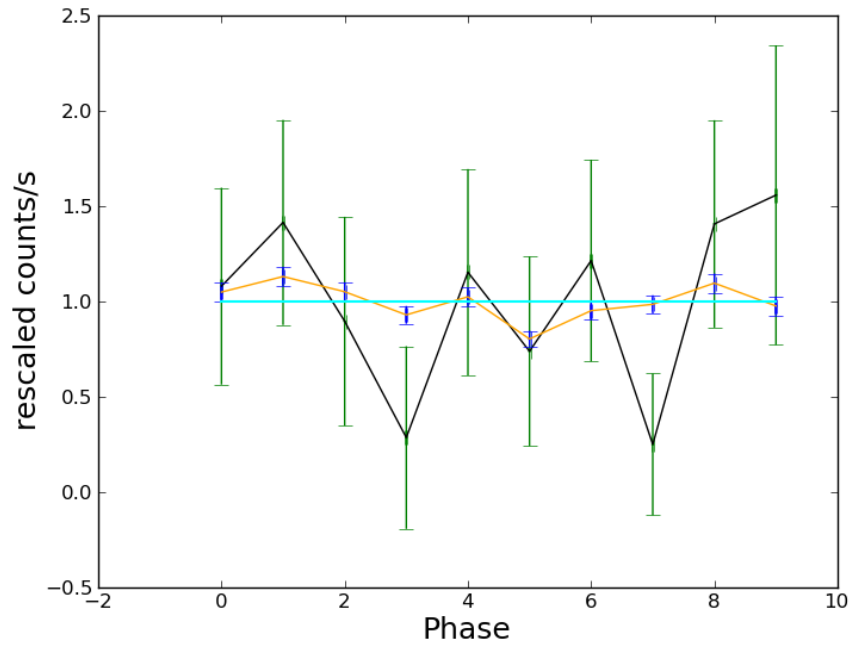
(b) OY Car In-eclipse (black) and out-of-eclipse (yellow)

44

the validity of this test. It is possible that there is variability in the in-eclipse count rate that is not detectable at this low signal to noise ratio. The reduced χ^2 results for HT Cas and OY Car are consistent with the sources varying in unison. However, the results have a low statistical significance and the low χ^2 values may be due to the large error ranges rather than any genuine correlation. The results are plotted in fig 3.6 and 3.7. Figure 3.6 indicates that for Z Cha the in-eclipse source often varies in a different way to the out-of-eclipse count rate.

Unfortunately the results from this analysis are fairly inconclusive for Z Cha, HT Cas and OY Car. This is mainly due to the low number of counts in each eclipse which makes any variations during eclipse difficult to detect using this data. To get reliable results, the data from many eclipses has to be taken together but this then makes it impossible to compare the variation over the course of the observation.

3.4   Comparing the hardness of the sources

In this section, I set out to determine whether there is a difference between the X-ray spectrum of the in-eclipse source compared to the out-of-eclipse source. The hypothesis is that if the in-eclipse source is different to the out-of-eclipse source. If this is true then it may have a different spectrum. If the in-eclipse X-ray emission is thermal emission from a stellar corona, we would expect it to be softer than the emission from accretion which dominates the out-of-eclipse source.

3.4.1   Calculation of hardness ratios

To test the above hypothesis, I split the observations into different energy ranges. I then determined the total number of counts detected in each energy range and calculated the ratio between them. This was repeated for the in-eclipse and out-of-eclipse data to see is there is a difference between their hardness ratios.

The light curves were extracted from the in-eclipse and out-of-eclipse event files which were made in section (3.1). This means they were extracted from time intervals of the same length. The in-eclipse events come only from time intervals when the white dwarf was fully eclipsed and the out-of-eclipse events come only from periods either side of the eclipse. The circles used for the extraction region 25 arc seconds radius and were the same for both in and out-of-eclipse.

The light curves were extracted in 3 energy ranges to allow ratios to be calculated between them. The ranges used were 0.2 - 0.6 keV, 0.6 - 1.4 keV and 1.4 - 8 keV. These ranges (0.2 - 0.6 and 0.6 - 1.4 keV) were chosen because images extracted at different energy ranges showed that the in-eclipse source was only visible

in the 0.2 - 1.4 keV energy range. This range was then divided in two so that a ratio could be calculated. This is referred to as Ratio 1. The 1.4-8 keV range was included because the out-of-eclipse source is still visible in this range. By combining the 0.2 - 0.6keV and 0.6 - 1.4keV range I also got a total for the 0.2 - 1.4keV (soft) range which was then be compared to the 1.4 - 8 keV (hard range). This gives Ratio 2. The background counts for each energy range were extracted from multiple circles on the same CCD as the source and scaled to the source region in the same way as described in the previous section.

The count rate for the in-eclipse source is very low for all observations. To improve the quality of the results, the data from the pn and MOS 1 & 2 cameras was combined to get a total number of counts using all 3 instruments.

The hardness ratio was calculated from the background corrected total number of counts in each energy range. The standard hardness ratio calculation is H/S where H is the total counts in the hard energy range and S is the total counts in the soft energy range. An alternative formula is (H-S)/(H+S). The advantage of using this formula is that the resulting number is limited to the range -1 to 1 . For this analysis the formula (H-S)/(H+S) was used although both were tested and gave equivalent results. This was repeated for both the in-eclipse and out-of-eclipse observations. The number calculated using this ratio gives an indication of how hard or soft the source is. Note that this is only relative to the energy ranges used in the calculation. Using this formula, a result of less than 0 indicates a softer source and results greater than 0 indicate a harder source. The results for all 3 observations are tabulated in table 3.3. The calculated hardness ratios are plotted in fig 3.8. The error in the ratio (H-S)/(H+S) was calculated using equation(3.4) (Jin et al., 2006), where σ_H and σ_S is the error in the total counts for the energy range in question.

$$\sigma_{HR} = \frac{2\sqrt{S^2\sigma_H^2 + H^2\sigma_S^2}}{(S+H)^2} \qquad (3.4)$$

Table 3.3: Total detected X-rays in different energy ranges for observation Z Cha. Totals are the result of combining detections from all 3 cameras. Results for HT Cas and OY Car are continued on next page.

Z Cha	Range 1 (keV)		Range 2 (keV)		Range 3 (keV)		Range 4 (keV)		Ratio 1		Ratio 2	
	0.2 - 0.6	±	0.6 - 1.4	±	0.2 - 1.4	±	1.4 - 8	±	0.6-1.4/0.2-0.6	±	1.4-8/0.2-1.4	±
Source												
in-eclipse	34	6	62	8	96	10	23	5	-	-	-	-
out-of-eclipse	1264	36	3425	59	4689	68	4035	64	-	-	-	-
Background												
in-eclipse	10.08	3.17	5.88	2.43	16.0	3.9	14.6	3.8	-	-	-	-
out-of-eclipse	12.8	3.6	8.3	2.9	21.05	4.6	20.5	4.5	-	-	-	-
Corrected												
in-eclipse	23.9	7.4	56.1	8.6	80.0	11.3	8.6	7.2	0.40	0.14	-0.80	0.15
out-of-eclipse	1251.2	35.7	3416.7	58.6	4667.9	68.6	4014.5	63.8	0.46	0.01	-0.08	0.01

HT Cas	Range 1 (keV)		Range 2 (keV)		Range 3 (keV)		Range 4 (keV)		Ratio 1		Ratio 2	
	0.2 - 0.6	±	0.6 - 1.4	±	0.2 - 1.4	±	1.4 - 8	±	0.6-1.4/0.2-0.6	±	1.4-8/0.2-1.4	±
Source												
in-eclipse	16	4	42	7	58	8	64	8	-	-	-	-
out-of-eclipse	286	17	1024	32	1310	36	1461	38	-	-	-	-
Background												
in-eclipse	10.1	3.2	14.0	3.7	24.0	4.9	65.7	8.1	-	-	-	-
out-of-eclipse	11.8	3.4	15.5	3.9	27.3	5.2	60.1	7.8	-	-	-	-
Corrected												
in-eclipse	6	6	28	8	34	10	-1.7	14.0	0.65	0.30	-1.10	0.91
out-of-eclipse	274.2	17.3	1008.5	32.2	1282.7	36.6	1400.9	39.9	0.57	0.02	0.04	0.02

OY Car	Range 1 (keV)		Range 2 (keV)		Range 3 (keV)		Range 4 (keV)		Ratio 1		Ratio 2	
	0.2 - 0.6	±	0.6 - 1.4	±	0.2 - 1.4	±	1.4 - 8	±	0.6-1.4/0.2-0.6	±	1.4-8/0.2-1.4	±
Source												
in-eclipse	27	5	37	6	64	8	24	5	-	-	-	-
out-of-eclipse	586	24	1818	43	2404	49	2077	46	-	-	-	-
Background												
in-eclipse	5.2	2.3	3.5	1.9	8.7	2.9	13.0	3.6	-	-	-	-
out-of-eclipse	5.9	2.4	6.8	2.6	12.7	3.6	21.7	4.7	-	-	-	-
Corrected												
in-eclipse	21.8	6.1	33.5	6.6	55.3	9.0	11.0	7.1	0.21	0.16	-0.67	0.18
out-of-eclipse	580.1	24.3	1811.2	42.7	2391.3	49.2	2055.3	46.0	0.51	0.02	-0.08	0.02

Figure 3.8: Comparison of the hardness ratio calculated for Z Cha (green), HT Cas (blue) and OY Car (yellow) during eclipse (circles) and out-of-eclipse (squares). Errors are calculated using eqn(3.4) but are too small to see on the out-of-eclipse data points.
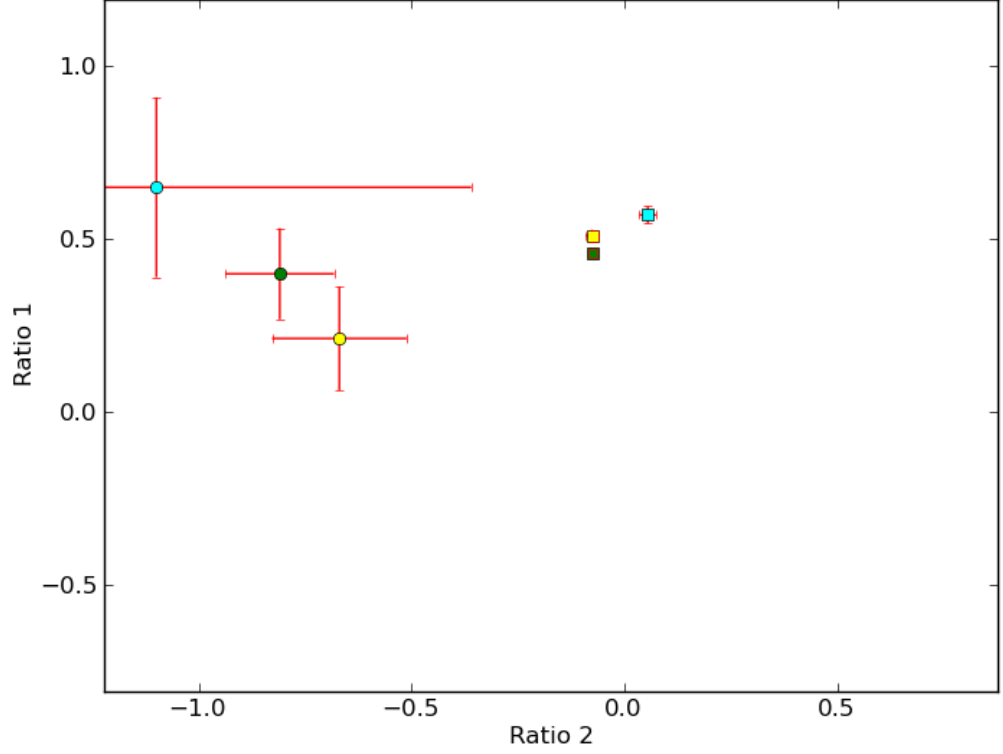
3.4.2 Results

Z Cha

The results show that in all 3 observations, there is an in-eclipse detection of at least 3σ in the 0.2-1.4 keV range. For Z Cha the background subtracted in-eclipse source is detected at the 6σ level with 80 ± 11 source counts compared to only 16 ± 4 background counts. The in-eclipse source is mostly detected in the 0.2-1.4 keV range. After background subtraction there are 80 ± 11 counts in the 0.2-1.4 keV range compared to only 8 ± 7 in the hard (1.4-8 keV) range. The out-of-eclipse source in comparison is detected in both the hard and soft ranges with 4667 ± 68 in the soft range and 4014 ± 64 in the hard range. The background in both the hard and soft ranges is fairly consistent at ~ 20counts. This shows that the in-eclipse

source is much softer than the out-of-eclipse source for Z Cha.

HT Cas

For HT Cas the background count rate was higher compared to the Z Cha observation. After background subtraction HT Cas shows the same trend as Z Cha with more in-eclipse counts in the soft range compared to the hard range. In contrast, the background subtracted out-of-eclipse source has slightly more counts in the hard range (1400 ± 40) compared to 1283 ± 37 in the soft range. This shows that the in-eclipse source for HT Cas is softer than the out-of-eclipse source although the significance of this result is lower ($< 3\sigma$) than for Z Cha and OY Car.

OY Car

The in-eclipse source of OY Car is detected at the 5σ level in the 0.2-1.4 keV range. There is a slight increase in the background from 9 counts in the soft range to 13 counts in the hard range but this is not as big a difference as in the HT Cas observation. The in-eclipse source of OY Car is comparable to those in Z Cha and HT Cas in that it has significantly more counts in the 0.2-1.4 keV range than the 1.4-8 keV range. The drop in count rate from the soft to the hard X-ray range is much more significant for the in-eclipse source where the count rate decreases by 80%. The out-of-eclipse source on the other hand decreases by only 14%.

Taken together, all 3 observations show similar results. The in-eclipse sources are all softer than the out-of-eclipse sources and have their peak in the 0.6-1.4 keV range. This change in the spectrum implies that the in-eclipse X-rays have a different origin to the out-of-eclipse X-rays or at least there must be some process to significantly modify the spectrum. For the in-eclipse sources there is no significant detection above 1.4 keV whereas for the out-of-eclipse sources, the number of counts does not change much between the hard and soft ranges.

When looking specifically at the in-eclipse sources, it is more appropriate to calculate the hardness ratio using 0.2-0.6keV (soft) and 0.6-1.4keV (hard) ranges. The in-eclipse sources of Z Cha, HT Cas and OY Car all follow the same pattern of having the majority of detected photons in the 0.6-1.4keV range and less in the 0.2-0.6keV range. The calculated hardness ratios (ratio 1, table 3.1 and 3.2) are all positive showing that the in-eclipse sources are at the hard end of the 0.2-1.4 keV range.

3.5 Optical light curve analysis

The bright spot is a possible source of X-rays and may contribute to the flux detected in-eclipse. To investigate this I analysed the optical light-curve produced by the Optical Monitor (OM) instrument on XMM-Newton. In the first part I used the OM light curve to see if there is any contribution from the bright spot and determine the phases when it is visible. In the second part I investigated the X-ray light-curve to see if there was any evidence for the bright spot at the same phases where it was visible in the optical light-curve.

3.5.1 The optical light curve

The optical light curve was extracted from data taken by the XMM-Newton Optical Monitor instrument which operates simultaneously with the PN and MOS cameras. The light curves were extracted using the SAS tool 'omfchain'. This produced a light curve for the source that was split into several files. These separate files were combined into one full light curve using my own python program. The light curve was then folded by phase and binned with a bin size of phase 0.00195 This allowed comparison with the PN light curve which had also been phase-folded and binned in the same way.

Analysis of optical light curves

Z Cha The optical light curve for Z Cha (fig 3.9) clearly shows the bright spot 'hump' since it contributes a large portion of the light at optical wavelengths. For Z Cha the optical light curve eclipse starts at the same phase(-0.03) as in the X-ray. This is where the white dwarf is eclipsed. There is then a very slight plateau between the A and B line at phase (-0.02) where the white dwarf is fully eclipsed but the bright spot is still visible. After phase (-0.02) the bright spot eclipse starts and the optical light curve reaches minimum at phase 0. The minimum of the optical eclipse is 0.02 cycle (129 seconds) after the start of the X-ray eclipse minimum. The difference in eclipse timings shows that the bright spot is still visible during the first half of the in-eclipse period up to phase 0 . Based on the evidence that the bright spot becomes fully eclipsed at phase 0, this phase is chosen as the boundary between bin 1 and 2 in section (3.5.2).

HT Cas Unlike Z Cha, the HT Cas optical light curve (fig 3.10a) does not show a clear contribution from the bright spot during the in-eclipse phase. If the bright
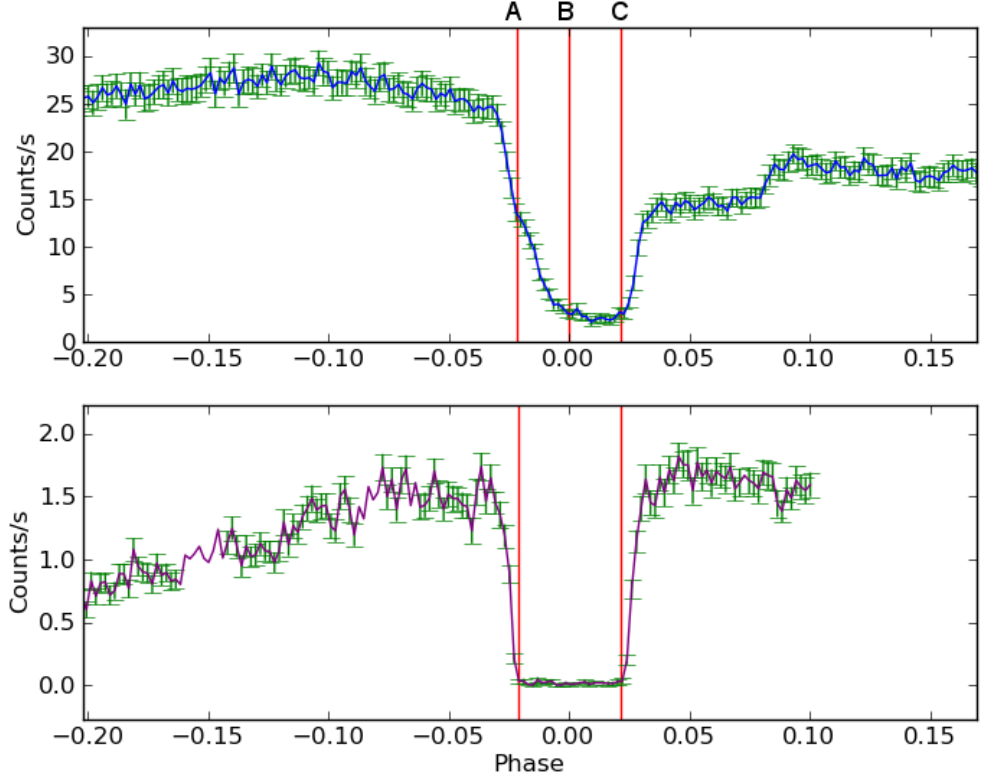
Figure 3.9: The OM optical (top) and EPIC X-ray (bottom) light curve of Z Cha.

spot is visible at all it would be in the first half of the white dwarf eclipse so the boundary between 1 and 2 was set to phase 0.

OY Car OY Car is more like Z Cha in that it shows a possible contribution from the bright spot between phases A and B. However, the optical light curve for OY Car only covers 1 eclipse so it is not clear whether this is representative of all the eclipses.

3.5.2 Searching for evidence of the bright spot in the X-ray eclipse

Next I attempted to quantify the bright spot contribution to the X-ray flux. To do this the in-eclipse X-ray light curves were binned into two bins so that one bin contained the interval where the bright spot is visible. The second bin contained only the interval when the bright spot was eclipsed by the secondary star. If the bright spot does make a significant contribution to the X-ray flux, then there should
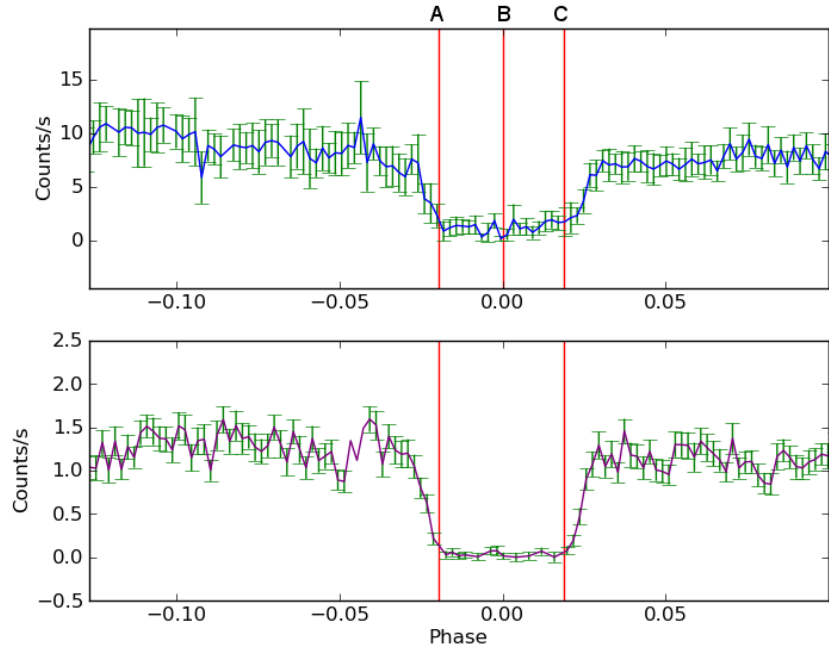
(a) HT Cas OM optical light curve (top) and EPIC X-ray light curve (bottom).
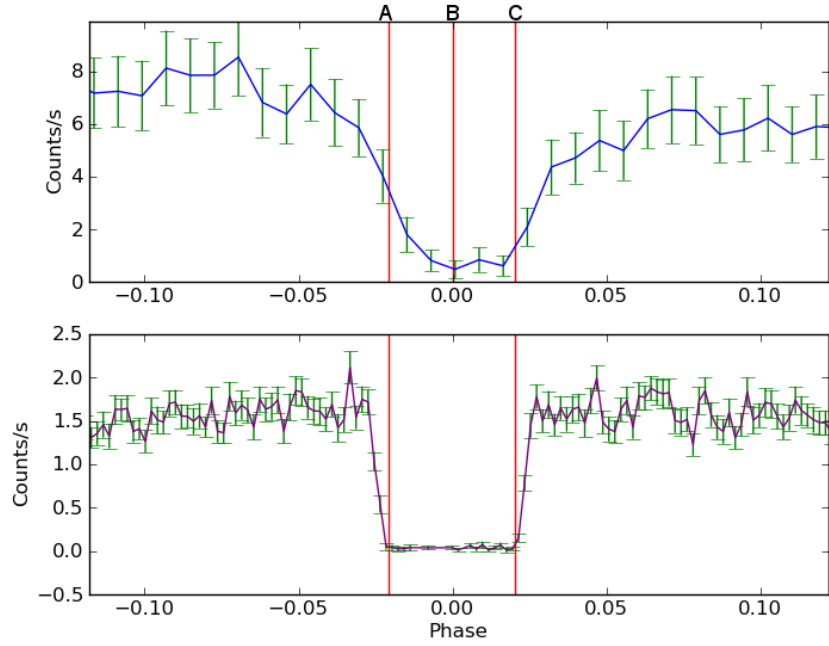
(b) OY Car

Figure 3.10: HT Cas (top) & OY Car (bottom) optical light curve and X-ray light curve showing the phase intervals used for bin 1 & 2 .

be a greater number of counts in the first bin when the bright spot was visible. For each observation, the X-ray light curves for the pn, MOS1 and MOS2 cameras were combined to get the total X-ray counts in each bin. The totals were background subtracted using background counts extracted from multiple circles on the same CCD chip and scaled to the same area as the source. The energy range used was 0.2-10keV.
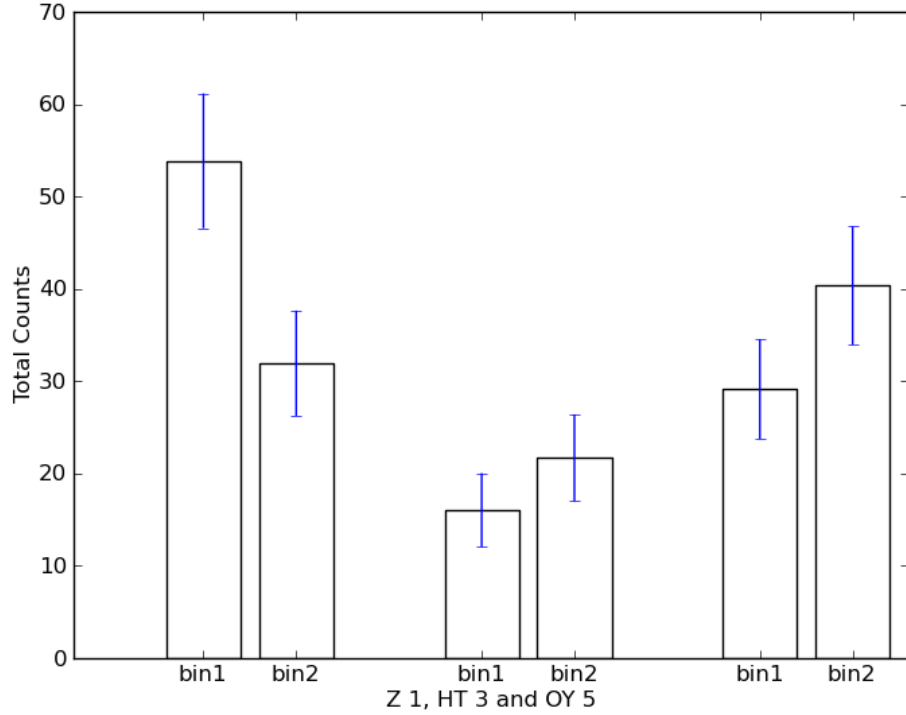
Figure 3.11: The total X-ray counts in the first and second half of total eclipse for all 3 observations. X-ray range (0.2-10keV). Z Cha (left), HT Cas (middle) and OY Car (right). Error bars indicate 1σ error range.

Results

The results show that only Z Cha has more counts in bin 1 compared to bin 2 (fig 3.11). Both HT Cas and OY Car actually have more counts in the second bin although this is not statistically significant. Also the optical light curves show that only Z Cha and possibly OY Car have an obvious contribution from the bright spot during the in-eclipse phase. The error bars in fig 3.11 indicate the 1σ error. This shows that the bright spot can not account for the in-eclipse X-rays detected from

HT Cas and OY Car. The bright spot may account for some X-rays in the first half of the Z Cha eclipses but it is not the main source of in-eclipse X-rays.

3.6   Spectral analysis

Spectral analysis can reveal a lot of details about the nature of the X-ray source such as the temperature, and the emitted flux. The spectrum extracted from the data is not the true spectrum emitted from the source because it has been altered by the characteristics of the detector. By convolving the model spectrum with the instrument response characteristics and then comparing the result to observed spectrum, we can determine what the original spectrum may have been and test the possibility that it has been emitted by different types of sources. The theoretical spectrum can then be used to derive the temperature and the flux which can be compared to values expected from different types of sources such as the secondary star corona or the bright spot.

The aim of this analysis is to determine whether the X-ray source observed during the eclipse is the same as the source observed out-of-eclipse and to determine the most likely candidate for the source. To do this I fitted theoretical spectra to the out-of-eclipse data. I then applied the same models to the in-eclipse data to see if the same source could produce both spectra.

3.6.1   Comparing the in-eclipse spectrum to the out-of-eclipse spectrum

Spectral data files were prepared using SAS and then loaded into XSPEC (Arnaud, 1996) to perform analysis. The spectra were extracted from the PN event files since these contained the most counts. The out-of-eclipse spectrum was taken from the PN event files that had been filtered to only contain an interval either side of the eclipse.

A separate spectrum was extracted for the in-eclipse source and was taken from the PN eclipse event file which had been filtered as described in section (3.1). Source and background spectra were extracted from the same regions used in the variability and hardness-ratio analysis. These were then scaled to the same size using the SAS 'backscale' tool. A redistribution matrix (RMF) was made using 'rmfgen' and an ancillary response matrix was made with 'arfgen'. The redistribution matrix file provides information about the response of the instruments at different energy ranges. This is used by XSPEC to convolve the observed spectrum and the instruments response characteristics. These files were then linked together

using the 'grppha' tool which is part of the HEASoft suite of astronomy software available from (http://heasarc.nasa.gov/lheasoft). This tool was also used to group the data so there were a minimum of 10 counts per bin in the spectra. The prepared files were then loaded into XSPEC for analysis.

In the following analysis I fit models to the in-eclipse and out-of eclipse sources separately for each model. Once a best fit model has been found for both the in-eclipse and out-of-eclipse source, their characteristics can be compared.

The 'ignore bad' command was used to remove channels that are out of the range of the instrument and to remove channels identified as bad by the calibration files. The energy range of the spectrum used for fitting was 0.1-10 keV. This energy range was chosen to include the range where most of the counts are but exclude bins where there are very few or negative counts due to background subtraction. Excluding the 10-12 keV range ensures that the spectral fitting will be carried out on bins with a good signal to noise ratio and will not be unduly affected by bins with low count rates.

Fitting the out-of-eclipse spectrum

The data were fitted with a MEKAL (Mewe et al., 1985) model for hot plasma combined with a WABS model for absorption by neutral gas (Morrison and McCammon, 1983). The WABS absorber reduces the counts in the soft X-ray range. The flux using the MEKAL model on its own would continue to increase in the 0.1-0.5keV range but this is not observed in any of the spectra so the inclusion of the WABS absorber improves the fit. The goodness of fit was tested with the χ^2 statistic. The results of fitting the out-of-eclipse spectra for all 3 systems are shown in table 3.4.

The results show that the out-of-eclipse spectrum is modelled well by a hot, 2 temperature plasma, with absorption in the soft X-ray range. All 3 systems emit in the the 0.1-10 keV range. The lower temperature component is in the range $kT = 0.9 - 1.4\,\mathrm{keV}$ while the high temperature components range from $7 - 9.4\,\mathrm{keV}$. Z

Table 3.4: Results of spectral fitting for out-of-eclipse observations.

	Z Cha	HT Cas	OY Car
model	wabs*(mek+mek)	wabs*(mek+mek)	wabs*(mek+mek)
kT 1 (keV)	1.4	0.9	1.46
kT 2 (keV)	7.04	7.76	9.4
$n_H(\mathrm{cm}^{-2})$	5.5×10^{20}	1.0×10^{21}	5.2×10^{20}
reduced χ^2	0.97	0.88	0.96
d.o.f.	391	139	218

Table 3.5: Results of simultaneously fitting the same model to both the in-eclipse and out of eclipse sources. The fit for both spectra together is good but the χ^2 result for just the in-eclipse spectra shows that the in-eclipse source is poorly fitted.

	Z Cha	HT Cas	OY Car
reduced χ^2 for simultaneous fit	1.03	0.90	0.98
reduced χ^2 for in-eclipse only	16.09	1.90	23.35

Cha, and OY Car have $N_H \sim 5\times10^{20}\,\mathrm{cm}^{-2}$ whereas HT Cas has $N_H \sim 1\times10^{21}\,\mathrm{cm}^{-2}$. These are consistent with values found in previous studies (e.g. (Nucita et al, 2009)).

Simultaneous fitting of the out-of-eclipse spectrum with the in-eclipse spectrum

Next I attempted to fit the out-of-eclipse model simultaneously to the in-eclipse and out-of-eclipse spectrum. If they both come from the same source then the out-of-eclipse model should be a good fit to both spectra.

The spectra were loaded into group 1 and 2 in XSPEC. The model used was a 2 temperature MEKAL model with a WABS absorber. A constant factor parameter was frozen at 1 for the out-of-eclipse model but allowed to vary for the in-eclipse model. All other parameters for the in-eclipse model were tied to the corresponding out-of-eclipse model parameters. This means that the only difference between the models is the normalized counts/s.

For Z Cha this results in a reduced χ^2 value of 1.03 but almost all of the in-eclipse data points were poorly fitted (see fig 3.13). HT Cas and OY Car also seem to have good fits with reduced χ^2 of 0.9 and 0.98 respectively. However, despite the χ^2 indicating a good fit, the plot of the spectral fits shows that the fit is not good for the in-eclipse spectra and the largest residuals are the in-eclipse data points around 1 keV. The low χ^2 values are a result of the low weighting of the few in-eclipse data points. The spectral fits for HT Cas and OY Car (fig 3.14) show similar results to Z Cha with the in-eclipse data points around 1 keV being poorly fitted. To calculate the χ^2 for the in-eclipse data I loaded the same model with the parameter values found for the in-eclipse data from the simultaneous fit. When the reduced χ^2 was calculated for the in-eclipse data alone, the results proved that the fit is not good (see 'in eclipse only' results in table 3.5). This result shows that the in-eclipse spectra can not be acceptably fitted with the same model as the out-of-eclipse spectra. The in-eclipse source is not just a fainter version of the out-of eclipse source and the in-eclipse X-rays are unlikely to have the same origin as the out-of-eclipse X-rays.

(a) Z Cha out-of-eclipse

(b) HT Cas out-of-ecipse

(c) OY Car out-of-eclipse
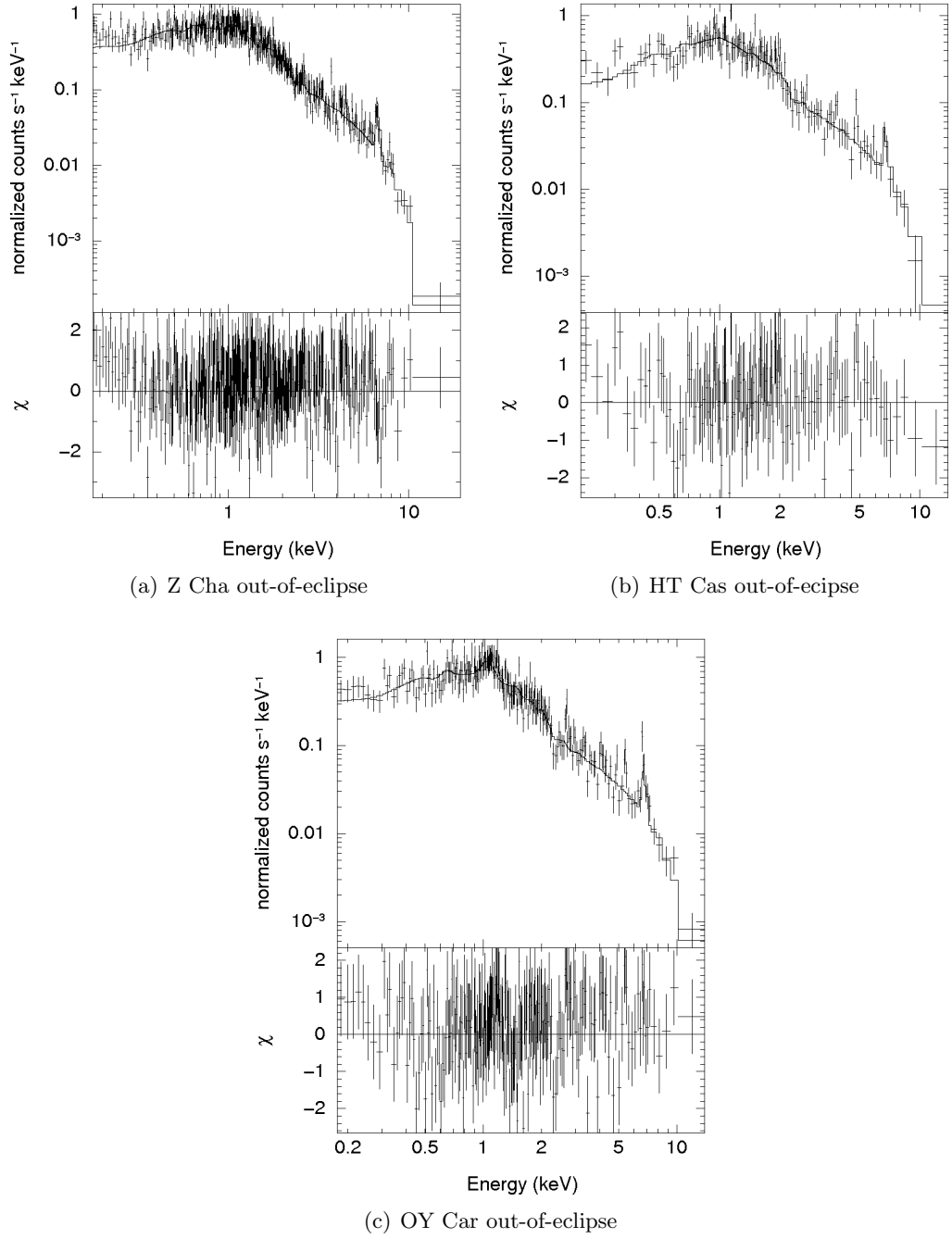
Figure 3.12: Out-of-eclipse spectra for all 3 observations fitted with a 2 temperature mekal model and wabs absorber.The black line in each upper panel is the model spectrum. The lower panels show the residuals of the observed spectrum from the model spectrum.Note that the axis are log scaled.

Figure 3.13: Plot or the out-of-eclipse (black) and in-eclipse (red) source from Z Cha fitted with the same spectral model.
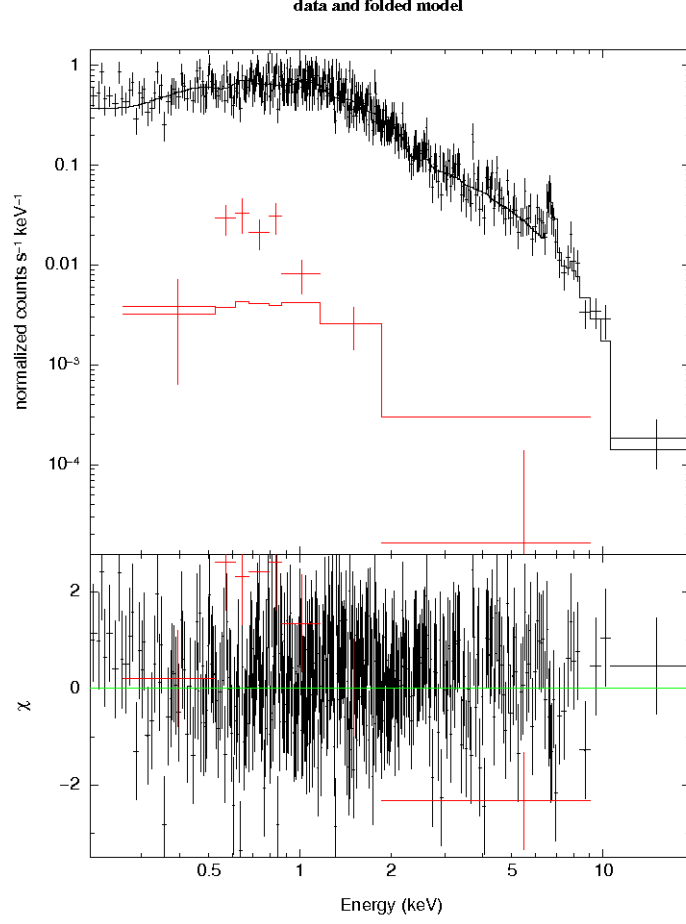
3.6.2 Fitting the in-eclipse spectrum

Coronal model spectral fitting

Having shown that the in-eclipse spectrum is different to the out-of-eclipse spectrum, I next attempted to find models that did fit the in-eclipse spectrum. In this way I aimed to test the hypothesis that the in-eclipse X-rays are due to scattering or the coronal emission of the secondary star.

An improved fit for the in-eclipse spectra was found when the model parameters were not constrained by the out-of-eclipse parameters. For each observation, the in-eclipse spectrum was fitted with a 2 temperature plasma model MEKAL with WABS absorber. A good fit of 1.16 was found for Z Cha and 1.08 for HT Cas. For OY Car the limited number of counts resulted in only 3 bins so a 2 temperature
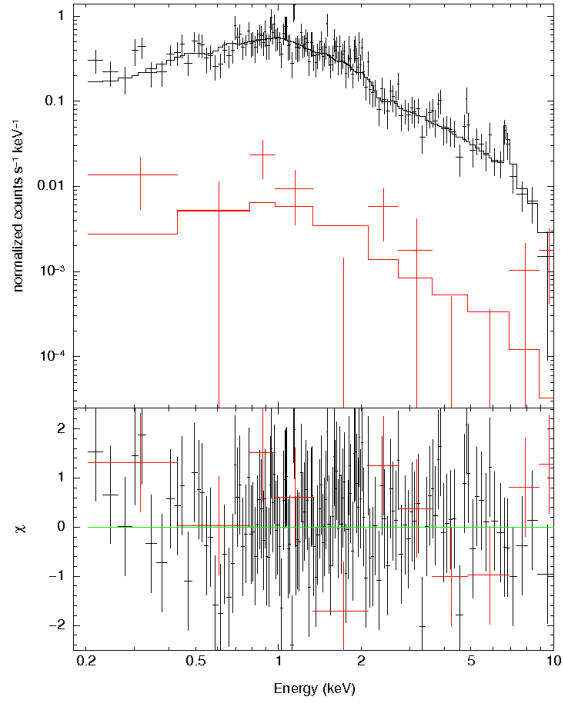
(a) HT Cas
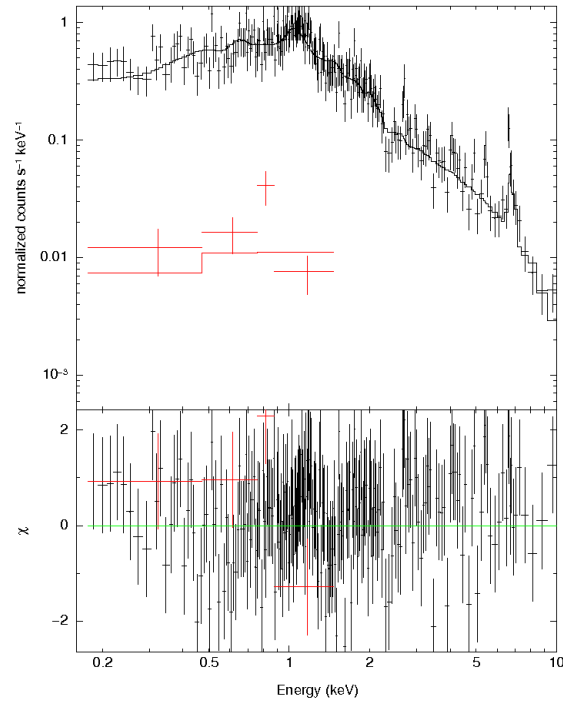
(b) OY Car

Figure 3.14: HT Cas and OY Car plot of the out-of-eclipse (black) and in-eclipse (red) source fitted with the same spectral model.

Table 3.6: The results of spectral fitting for the in-eclipse sources using a Mekal model with Wabs absorber. The goodness of fit is calculated using the C-statistic.

	units	Z Cha	HT Cas	OY Car
N_H	cm^{-2}	3.6×10^{21}	3.4×10^{20}	6.4×10^{19}
kT(1)	keV	0.21	0.86	0.56
kT(2)	keV	1.98	1.98	-
reduced χ^2	-	1.16	1.08	0.81
goodness of fit	-	32%	39%	10%
flux (0.2-2keV)	$erg\,s^{-1}\,cm^{-2}$	1.944×10^{-14}	1.69×10^{-14}	2.45×10^{-14}

model could not be constrained. A 1-temperature model with absorber resulted in a reduced χ^2 of 0.81. The resulting spectral fits are shown in fig 3.15.

The lack of counts for the in-eclipse spectra meant they had to be binned with 10 counts per bin rather than 25 which is recommended as the minimum for the χ^2 statistic. The χ^2 test may not be appropriate for these low count rates so the fit was also tested with the C-statistic (Cash, 1979). The results of the C-statistic goodness of fit test are shown in table 3.6. When using the C-statistic, the goodness of fit can not be calculated in the same way as for the χ^2 statistic. Instead, I used the 'goodness' command in XSPEC which does repeated simulations of data based on the model and calculates the percentage of those simulations which give a better fit than the observed data. If most of the simulations give a better fit than the observed data then the model is unlikely to be a correct fit for the data. Using this test a value of $\sim 50\%$ indicates that the model is a good fit to the data (Arnaud).

Using the C-statistic, the in-eclipse model for Z Cha had a goodness of fit of 32% (table 3.5), where a result of $\sim 50\%$ is a good fit and very low or high percentage values are an indication of a statistically insignificant fit. HT Cas had a similar goodness of fit of 39% so these results are fairly reliable. The goodness of fit for OY Car however was only 10% because there are not enough data points to discount other models or fit parameters.

The model parameters for the in-eclipse spectral fitting are shown in table 3.6 and the spectra are plotted in fig 3.15. All 3 spectra are remarkably similar with a peak between $0.5 - 1\,keV$. There is clearly very little emission above $2\,keV$ unlike the out-of-eclipse spectra. Having found acceptable theoretical models for the in-eclipse sources, I derived the flux of the in-eclipse source. All 3 systems had an in-eclipse X-ray flux of $\sim 2 \times 10^{-14}\,erg\,s^{-1}\,cm^{-2}$ in the $0.2 - 2\,keV$ range.

Figure 3.15: The in-eclipse spectra for all 3 observations fitted with mekal plasma models and wabs absorption.
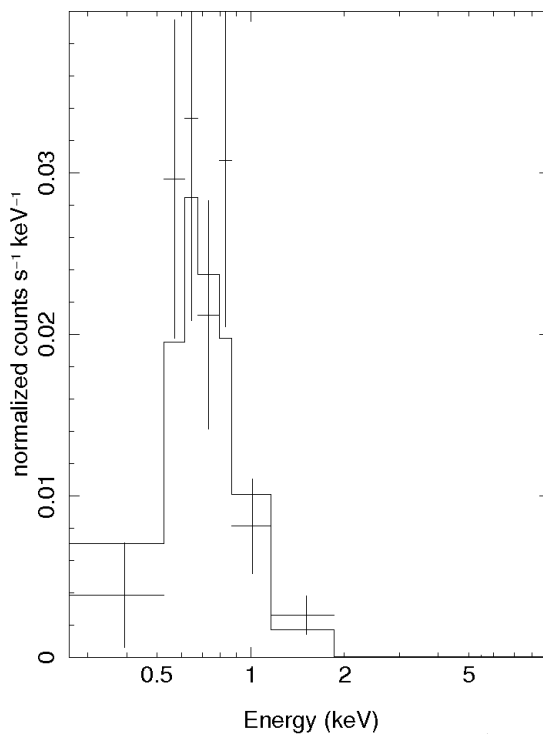
(a) Z Cha in-eclipse spectrum.
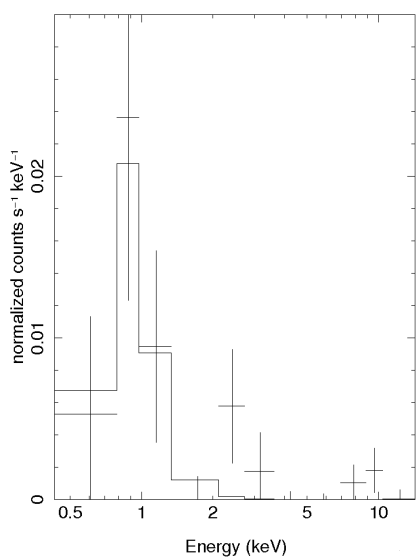
(b) HT Cas in-eclipse spectrum.
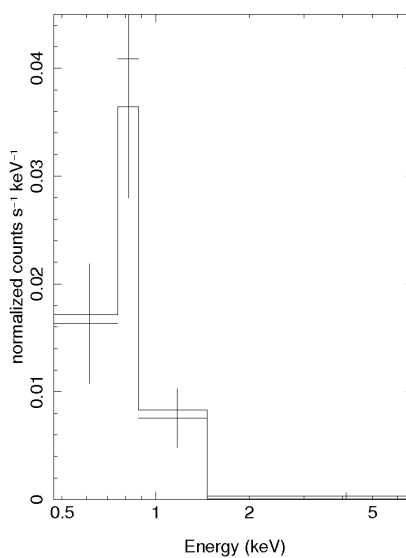
(c) OY Car in-eclipse spectrum.

Further fitting of Z Cha One problem with the in-eclipse fit for Z Cha is that the absorption needed is higher than expected at $N_{\mathrm{H}} = 3.6 \times 10^{21}\,\mathrm{cm}^{-2}$. The column density to Z Cha has been estimated at $N_{\mathrm{H}} = 0.09 \times 10^{20}\,\mathrm{cm}^{-2}$ (Dickey and Lockman, 1990). Fitting with a two temperature MEKAL model without WABS was attempted and resulted in a reduced χ^2 of 2.09 with a null hypothesis probability of 7.9×10^{-2}. The parameters for this fit are shown in table 3.7 and the results plotted in fig 3.16.

Figure 3.16: Plot in-eclipse spectrum for Z Cha fitted with a 2 temperature MEKAL model.
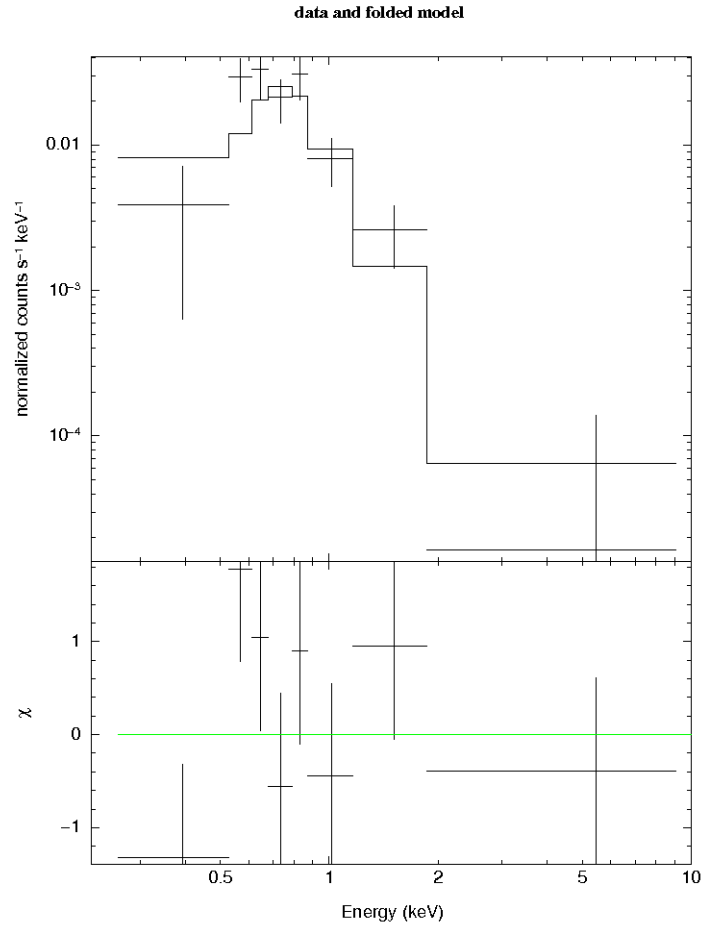
While the fit is not as good as the model with higher absorption, it seems a more realistic model given the lack of a known source of absorption. The X-ray flux for the in-eclipse source estimated for this model is $1.96 \times 10^{-14}\,\mathrm{erg\,s}^{-1}\mathrm{cm}^{-2}$ which is very close to the value estimated from the fit using higher absorption (table 3.6).

Table 3.7: Results of in-eclipse spectral fit for Z Cha using a 2 temperature MEKAL model.

Parameter	Units	Z Cha
kT (1)	keV	0.38
n_H	cm^{-3}	1
abundance		2.2
kT (2)	keV	2.3
n_H	cm^{-3}	1
abundance	relative to solar	2.24
reduced χ^2		2.09
null hypothesis		7.9×10^{-2}
X-ray flux (0.2-2 keV)	$erg\,s^{-1}\,cm^{-2}$	1.96×10^{-14}

3.6.3 Scattering model spectral fit

To investigate the possibility that the in-eclipse X-rays are emitted by a photo-ionised gas that surrounds the binary system, the in-eclipse spectra were also fitted with a scattering model. Gas surrounding the system could be irradiated by the X-rays from the boundary layer and these are then scattered in to our line of sight by the gas. To test this theory I attempted to fit the detected in-eclipse spectrum with a model scattering spectrum produced by the XSTAR software (Kallman, 1999) in XSPEC. The grid used was grid23 which was used to simulate a similar situation in CH Cygni (Wheatley and Kallman, 2006). The XSTAR program works by taking an input spectrum and parameters for the surrounding gas. The free parameters in grid23 are the ionisation parameter ξ and the column density N_H of the gas and also the normalisation.

The ionisation parameter is the ratio of ionising photons to atoms in the scattering material. Equation 3.5 shows that the ionisation increases with the luminosity of the source since there are more photons to ionise the gas. The ionisation parameter decreases with the number density of the gas 'n' and the square of the distance from the source 'R' because the ionising radiation is spread over a larger area.

$$\xi = \frac{L}{nR^2} \tag{3.5}$$

L is the source luminosity in the 0.2-2 keV range ($erg\,s^{-1}$) and n is the number of atoms in the scattering medium so a greater number of atoms will need a greater number of photons to ionise them. The elemental abundances of the scattering medium were fixed in this analysis.

XSTAR calculates the ranges of possible values for each parameter in the model in the following way. The gas is divided up in to sections through which the radiation from the input source travels. The interaction between the radiation and the scattering medium are calculated resulting in an output spectra for a range of parameter values. This process is repeated at each stage since the input spectrum is modified as it interacts with the gas. There is also the effect that the photo-ionised gas in previous section emits photons so it contributes to the input spectrum in later sections. The calculation is an iterative process where the gas is affected by the input spectrum and the input spectrum is modified by the gas at each stage.

The emission seen depends on the geometry of the system. If we had a direct line of sight towards the boundary layer source, then we would see an absorbed source spectrum with emission from the scattering material. In the case of the in-eclipse source however, we are only seeing scattered emission from the surrounding gas since the boundary layer source is obscured. XSTAR produces a model grid with a range of values for each parameter which can then be used for fitting in XSPEC.

The input spectrum for the XSTAR model was bremsstrahlung at a temperature of 8keV. This was fitted to the out-of-eclipse spectrum for each system to see if it is a realistic model for the input spectrum. This resulted in a good fit with reduced χ^2 of 0.89 - 1.24 . The normalisation from this fit was then set as a fixed parameter when fitting the in-eclipse spectra to the XSTAR output spectrum.

The scattering model resulted in a poor fit to the in-eclipse spectra with reduced χ^2 of 2.45-15.64 . The values for the best fits in table 3.9 show that the maximum values of $log\xi$ and the minimum values of N_H available in this model gave the best fits. The scattering model produced too much luminosity to be a good fit for the observed source and the fit could only be improved by using the most extreme values. An improved fit may have been possible using a lower N_H but lower values were not available using this model.

To test this theory, I repeated the fitting for Z Cha but allowed the normalisation to vary to compensate for the N_H values being too high. This did produce a good fit of reduced $\chi^2 = 1.13$. This is shown as Z Cha(2) in table 3.9. This shows that if a lower value of N_H were available, then it is likely that a much better fit could be found while still using the correct normalisation.

Plotting a graph of reduced χ^2 contours for normalisation vs N_H revealed that in this model there is a linear relationship between the normalisation and N_H when plotted on a log scale (see fig 3.17). From this graph, which has the equation(3.6), I extrapolated the N_H value which would have produced the same improvement in the fit as the artificially low normalisation. When the normalisation

was reduced from 9.38×10^{-4} to 1.2×10^{-3}, this was equivalent to reducing the column density to $8.3 \times 10^{17} \mathrm{cm}^{-2}$.

$$\log(norm) = \log(1 \times 10^{15}) + (-1) \times \log(N_H) \tag{3.6}$$
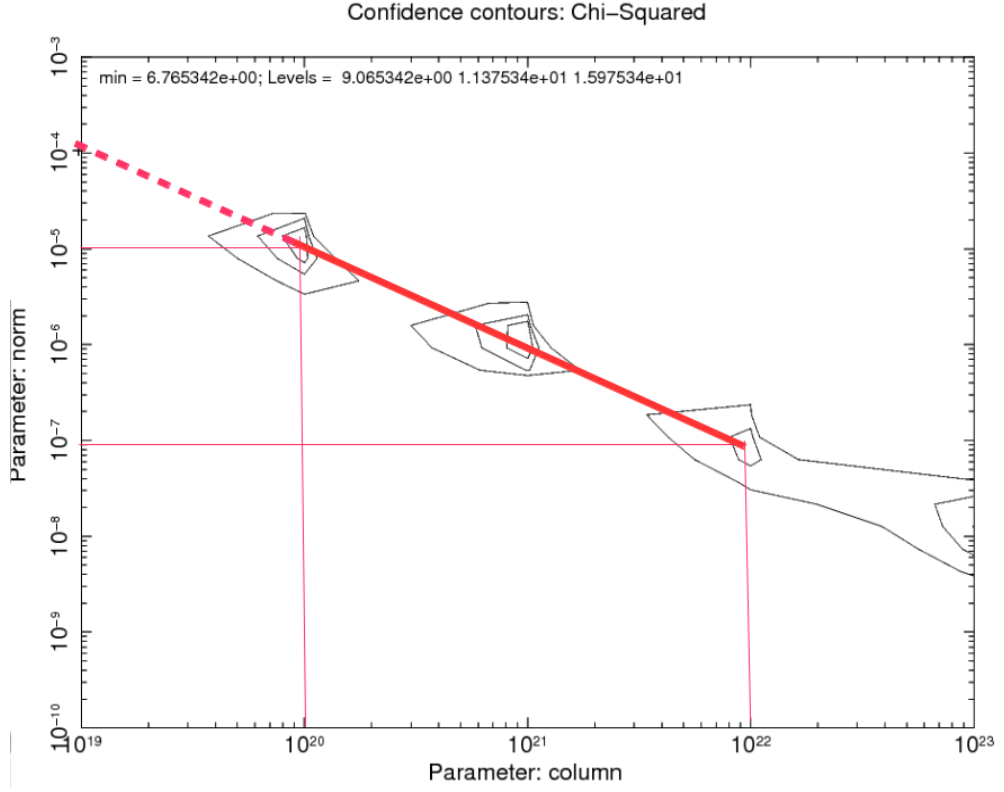
Figure 3.17: The relationship between normalisation and column density (N_H) parameters in the scattering model. The dotted line indicates the extrapolated values of N_H.

In the scattering model there is no indication of continuum emission. The model spectrum is shown in fig 3.18 (left). The fitted spectrum for Z Cha is shown in fig 3.19. This fit resulted in the parameters listed as Z Cha in table 3.9. The ionisation parameter can take a wide range of values so I repeated the fitting process with a number of different starting values to check that this was the best fitting value rather than a local minimum.

Table 3.8: The results of fitting the out-of-eclipse spectrum with a pcfabs * bremsstrahlung model. Also the flux and luminosity used for the XSTAR input source based on this model.

		Z Cha	HT Cas	OY Car
reduced χ^2		1.02	0.89	1.24
normalization		9.38×10^{-4}	8.33×10^{-4}	9.14×10^{-4}
flux (0.2-10 keV)	$\mathrm{erg\,cm^{-2}\,s^{-1}}$	4.5×10^{-12}	3.8×10^{-12}	4.7×10^{-12}
L_X	$\mathrm{erg\,s^{-1}}$	7.15×10^{30}	7.06×10^{30}	6.04×10^{30}

Table 3.9: The column density and ionisation parameters found from fitting the in-eclipse source with the scattering model. Z Cha (2) is the result of fitting when the normalisation was free to vary.

		Z Cha	Z Cha (2)	HT Cas	OY Car
reduced χ^2		15.64	1.13	2.45	7.99
N_H	$\mathrm{cm^{-2}}$	1×10^{19}	8.3×10^{17}	1×10^{19}	1×10^{19}
$log\xi$		4	4	4	4

(a) Z Cha

(b) HT Cas
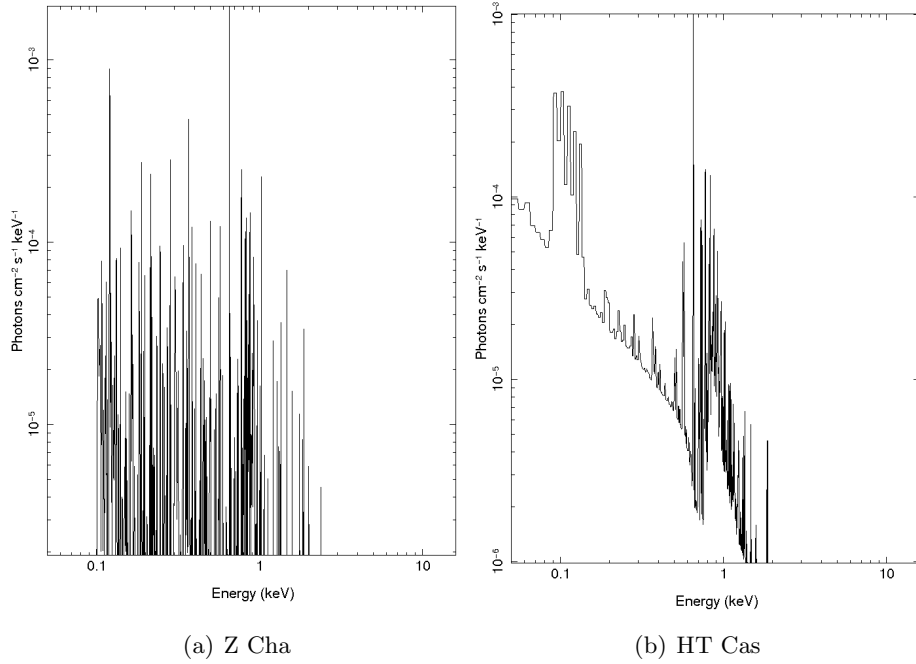
Figure 3.18: Comparison of the model spectra used for fitting to the in-eclipse spectrum of Z Cha. (left) Model spectrum for boundary layer emission scattered by a photo-ionised gas. (right) Model spectrum for 2-temperature hot plasma with absorption in the soft energy range.
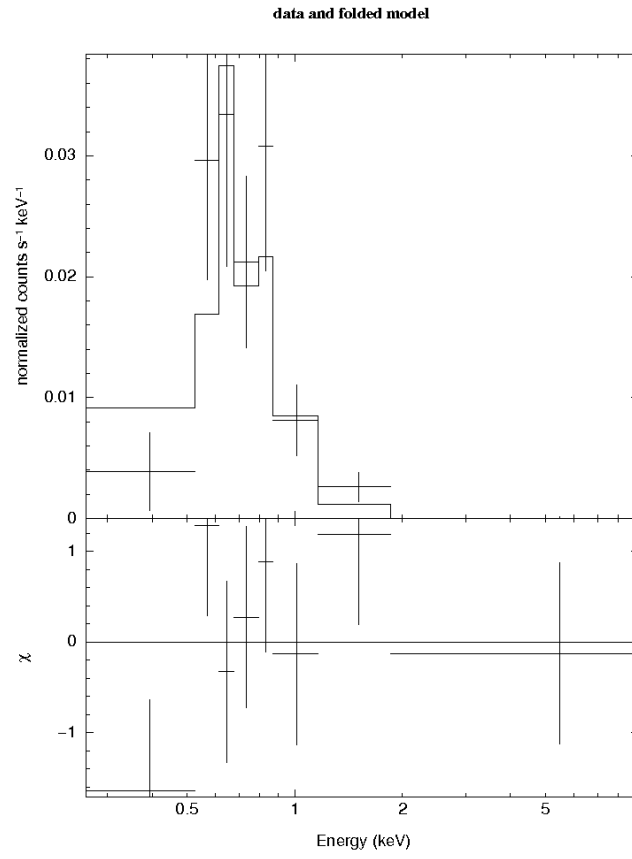
Figure 3.19: Z Cha in-eclipse spectrum fitted with model for scattered boundary layer emission.

Chapter 4

Discussion

4.1   The in-eclipse source

X-ray images taken during the eclipses of Z Cha, HT Cas and OY Car show that a faint source is still detected even though the white dwarf and boundary layer are not in our direct line of sight. Analysis of this in-eclipse source shows that it differs from the out-of-eclipse source in a number of ways which suggests that the in-eclipse X-rays have a different origin to the out-of-eclipse X-rays. The out-of-eclipse X-rays are known to originate from the boundary layer and white dwarf where they are emitted due to the release of kinetic energy from accreted material. I now compare all of the results of the analysis for the in-eclipse and out-of-eclipse sources, and discuss the possible origins of the in-eclipse X-rays.

4.1.1   Properties of the in-eclipse source and comparison with the out-of-eclipse source

For all 3 systems, the in-eclipse source is much fainter than the out-of-eclipse source. Taking the total counts in the 0.2-10keV range, the in-eclipse total is only $\sim 1-1.5\%$ of the out-of-eclipse total.

When comparing the variability in the count rate of the in/out of eclipse sources, it is expected that if the sources have the same origin then they will vary in unison. The analysis of Z Cha showed that there is no evidence that the sources vary in unison within the sensitivity of this data. This is based on the result that when comparing the sources for Z Cha, the χ^2 result was 2.02 and the null hypothesis probability was 1.27%. For the in-eclipse source, no variability around the average could be detected within the limits of the low signal to noise ratio which resulted in a low reduced χ^2 of 1.79. In comparison the out-of-eclipse source was significantly

variable with a reduced χ^2 of 10.52 (table 3.1). It is not possible to draw a conclusion for HT Cas and OY Car because the light-curves are not statistically different having null hypothesis probabilities of $\sim 40-50\%$ (table 3.2). This does not mean that the HT Cas and OY Car results contradict the Z Cha result. The in/out of eclipse light curves may have variations which are too difficult to detect due to the low count rate.

Comparison of the number of X-rays detected in different energy ranges showed that the in-eclipse source emits almost entirely in the 0.1-1.4 keV range with the majority of counts being in the 0.6-1.4 keV range. This contrasts with the out-of-eclipse sources which emit strongly in the harder 1.4-10 keV range as well as the soft range. The softness of the in-eclipse source suggests that they may be from the corona of the secondary star since this would emit softer X-rays than the boundary layer due to its lower temperature although scattering could also produce a softer spectrum.

The result that the in-eclipse sources are softer than the out-of-eclipse sources was confirmed by the spectral analysis which showed that the peak of the in-eclipse spectra was in the 0.5-1 keV range with very little emission above 2 keV. In contrast, the out-of-eclipse sources had strong emission all the way up to 10 keV.

The result of trying to fit the in-eclipse spectrum of Z Cha with the same model as the out-of-eclipse spectrum is shown in fig 3.13. The reduced χ^2 value of 1.03 suggests that the same model can be scaled to obtain a good fit to both the in-eclipse and out-of-eclipse spectrum. However, visual inspection of the spectra shows that almost all the data points from the in-eclipse spectrum are badly fitted. The reduced χ^2 value of the in eclipse spectrum alone is 16.09 . Clearly the in-eclipse spectrum is not just a fainter version of the out-of-eclipse source. Similar results were found for HT Cas and OY Car (table 3.5).

In all respects, the in-eclipse sources detected in all 3 systems have very similar properties. This increases our confidence that the results are reliable and that they represent in-eclipse sources which are common to SU UMa type CV's and not due to special circumstances within an individual system. Taken together, these results all support the hypothesis that the in-eclipse X-rays do not come directly from the boundary layer.

The detection of X-rays during the eclipse of the boundary layer and white dwarf raises the question of their origin. The two main scenarios are A) that there is a second source of X-rays which is still visible when the boundary layer is not in our direct line of sight, or B) that the X-rays always originate from the white dwarf and boundary layer, but during the eclipse, we observe X-rays that have been

scattered into our line of sight. In case B, the scattering region would have to have a much larger extent than the white dwarf otherwise it would also be eclipsed. I now discuss whether the analysis can show which of these scenarios is correct.

4.2 Possible sources of the in-eclipse X-rays

In this section I investigate the possible sources of X-rays in CVs and compare them to the in-eclipse sources that were actually detected in Z Cha, HT Cas and OY Car. First the possibility that the in-eclipse source is the bright spot is tested. Then the possibility of the secondary star and scattered boundary layer emission is discussed.

4.2.1 The bright spot

The optical light curve of Z Cha (fig 3.9) shows clear evidence of a hump associated with the bright spot. This indicates that the bright spot in Z Cha is a significant contributor to the optical light. The length of time after the white dwarf eclipse where the bright spot is still eclipsed is indicated by the plateau in the light curve after mark C in fig 3.9. The duration of this plateau shows that the bright spot must be compact so it is obscured by the secondary star for longer. In the X-ray light curve the count rate almost immediately returns to its pre eclipse level of 1.6 counts/s. In comparison, the optical light curve only increases to about half its pre eclipse count rate because the bright spot is still eclipsed. After a plateau covering phase (0.03 to 0.08) the bright spot eclipse ends. The count rate is still lower than just before the eclipse because the bright spot is moving to the far side of the disk and so much of its light is now obscured from view.

The result of comparing bin 1 and 2 for each observation is that only Z Cha has more counts in the first bin which means that the bright spot cannot be the source of in-eclipse X-rays in HT Cas and OY Car. Bin 1 of the Z Cha eclipses does have more counts than bin 2 at the 2σ level so the Z Cha in eclipse source might include a contribution from the bright spot. It is clear that an X-ray source other than the bright spot is detected during the eclipses so a contribution from the secondary star or scattered boundary layer emission is needed to explain these observations.

From the optical light curves it is reasonable to expect that bin 1 of the Z Cha observation will include X-rays from the bright spot. For HT Cas and OY Car, the lack of a hump in the optical light curves suggests that the bright spot may be very faint and not make a large contribution.

The lack of a clear bright spot hump in the optical light curves of HT Cas and OY Car may indicate that the system was in a period of low mass transfer. This can reduce the temperature of the bright spot to the point where it is almost the same as the rest of the accretion disk. Previous studies e.g. (Feline et al, 2005) have shown that the bright spot can vary in this way over periods of months or years.

From this analysis I conclude that the bright spot cannot be the main source of the observed in-eclipse X rays.

4.2.2 The secondary star

In order to make a comparison between the in-eclipse source and the X-rays expected from the secondary star, it is necessary to determine what properties the secondary star would have. Table 1.1 shows that the secondaries are low mass stars with mass in the range $\sim 0.07 - 0.2 M_\odot$ and spectral type $\sim$ M5V. As discussed in section (1.3) these stars are probably fully convective and tidally spun up to the orbital period of ~ 2 hours. In this analysis I assume that the secondary stars are tidally locked. First the X-ray luminosity (L_X) of the in-eclipse source is calculated. In the following sections, the in-eclipse source is compared to single M-dwarfs, binary central stars of planetary nebulae and pre-CVs.

Calculation of L_X and $\frac{L_X}{L_{bol}}$

The X-ray flux for the in-eclipse source is calculated from the X-ray spectrum in the energy range 0.2-2keV using XSPEC. This is then combined with the distance to the system to calculate L_X. The distance estimates from the literature vary widely (table 1.1). To try to put limits on the uncertainty, I have repeated the calculation using the most extreme distance estimates for each system (table 4.1).

Comparison with single M-dwarfs

To compare the in-eclipse L_X to that expected for a low mass M-dwarf, it is necessary to calculate the L_X expected from an M-dwarf of the same mass and rotation rate using the activity-rotation relation (see section 1.3). The first stage is to determine if the secondary star should be considered saturated. The study of low mass stars by Pizzolato et al (2003) showed that they become saturated at $R_0' \approx 0.1$. In this analysis, the modified Rossby number (R_0') was used as described in Pizzolato et al (2003). R_0' is given by $R_0' = \frac{P_{rot}}{\tau_e}$, where P_{rot} is the rotation period of the secondary star (days). However, in this case it is taken to be the orbital period of the binary star, since the secondary is tidally synchronised to the binary period. τ_e is the

convective turnover time and is calculated using $\log \tau_e(\frac{M_2}{M_\odot}) = 1.1$ days. This scaling was adopted in Pizzolato et al (2003) and shows good agreement with convective turnover times based on stellar models e.g. (Ventura et al, 1998).

The values used for the secondary star mass are taken from table 1.1. For this analysis I have used the mass values estimated from the eclipsing method (Wood, 1987) which gives $0.08 M_\odot$ for Z Cha, $0.09 M_\odot$ for HT Cas and $0.07 M_\odot$ for OY Car. The values for P_{rot} are those used when folding the light curves in section (3.1)(see references in table 1.1).

These results (table 4.2) show that the secondary stars in all 3 systems are beyond the saturation limit of $R_0' \approx 0.1$ so the appropriate method for calculating L_X is $\frac{L_X}{L_{bol}} = 10^{-3}$. The calculation requires an estimate of L_{bol} for each of the secondary stars. This can be obtained using the Mass-Luminosity relation for low mass stars (D'Antona and Mazzitelli, 1994). A previous study tested this M-L relation with a sample of low mass stars and there was good agreement between the observations and the theoretical M-L relation (Malkov et al, 1997). This is shown in fig 4.1 which is reproduced from Malkov et al (1997). Using the mass of the secondary stars from table 1.1 and the values of L_{bol} derived from fig 4.1, I calculate the predicted X-ray luminosity of the 3 secondary stars in table 4.4. The red line on fig 4.1 indicates approximately the mass and corresponding value of $log\frac{L}{L_\odot}$ used for the secondary stars.

To check that the estimates of L_{bol} are reasonable, an alternative method was used. Using T_{eff} of 2850 K (Testi, 2009) for a star of spectral type M5.5 (based on values in table 1.1), the luminosity was calculated using $L = 4\pi R^2 \sigma T_{eff}^4$ (Hale Bradt, 2004) where R is the radius of the secondary star taken from table 1.1 and σ is the Stefan-Boltzmann constant. The spectral types are taken from references in table

Table 4.1: Calculations of L_X for the observed in-eclipse sources using flux estimates based on models fitted to the in-eclipse spectra using XSPEC and distance estimated from the literature (table 1.2).

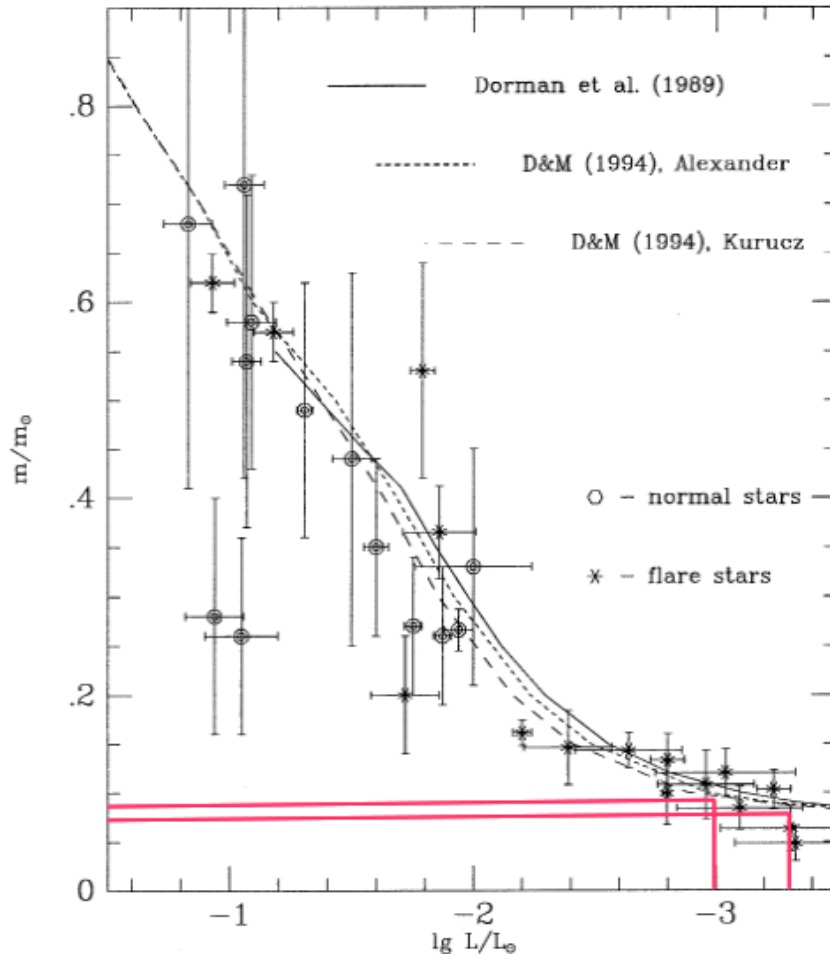|	Z Cha	HT Cas	OY Car
flux($\mathrm{erg\,s^{-1}cm^{-2}}$)	1.94×10^{-14}	1.69×10^{-14}	2.45×10^{-14}
distance(min)(pc)	97	107	82
distance(max) (pc)	131	140	121
L_X (min) $\mathrm{erg\,s^{-1}}$	2.19×10^{28}	2.32×10^{28}	1.97×10^{28}
L_X (max) $\mathrm{erg\,s^{-1}}$	3.99×10^{28}	3.96×10^{28}	4.29×10^{28}
L_X (average) $\mathrm{erg\,s^{-1}}$	3.09×10^{28}	3.14×10^{28}	3.13×10^{28}

Figure 4.1: The Mass - Luminosity relation for low mass stars. The theoretical tracks are from (D'Antona and Mazzitelli, 1994) and are a good fit to the observations of low mass stars. The red lines indicate approximately the mass of the secondary stars and the corresponding $logL_{bol}/L_{\odot}$. Diagram reproduced from Malkov et al (1997).

1.1 and are derived from infra-red observations so they are not based on the mass of the star. The key difference between these two methods is that method 1 is based on the mass of the star, while method 2 is based on the spectral type and the radius of the star. Both quantities depend on independent methods of measuring different properties of the star, but they both give similar results for L_{bol} as shown in table 4.3. A comparison can also be made with the values predicted by the semi-empirical donor sequence for CVs (table 3 (Knigge, 2006)). For CVs with $P_{orb} \sim 1.5 - 1.8$ hours, the predicted secondary star luminosity is $\sim 3.2 \times 10^{30} - 9 \times 10^{30}\,\mathrm{erg\,s^{-1}}$.

The activity-rotation relationship shows that the upper limit for L_X is related to L_{bol} by $log\frac{L_X}{L_{bol}} = -3$. Now assuming that the stars are saturated, the theoretical L_X in table 4.4 is calculated using $\frac{L_X}{L_{bol}} = 10^{-3}$. This gives a maximum theoretical L_X of $3.42 - 3.84 \times 10^{27}\mathrm{erg\,s^{-1}}$. The calculated L_X for the in-eclipse sources was higher than this at $3.09 - 3.13 \times 10^{28}\mathrm{erg\,s^{-1}}$ which results in $log\frac{L_X}{L_{bol}} \sim 2.27$ which is beyond the theoretical saturation limit.

This shows that the observed X-ray luminosity is greater than than predicted by the activity - rotation relation by almost an order of magnitude in all 3 systems which would seem to be evidence against the secondary star being the in-eclipse source. However, as discussed in the following sections, there is observational evidence that these theoretical estimates may be an order of magnitude too low. Also, a closer look at the evidence for the $log\frac{L_X}{L_{bol}} = -3$ saturation limit shows that many systems do in fact have values up to -2 as will be discussed in the following sections.

To check that the X-ray luminosity predicted by the activity - rotation relation is realistic, the results were compared to X-ray observations of M-dwarf stars. In general, M-dwarfs have L_X values in agreement with the activity-rotation relationship. However there are individual cases where the L_X detected can actually be higher than expected. For example, a study by Shkolnik et al. (2009) shown in fig 4.2 reveals many single M-dwarfs with $log\frac{L_X}{L_{bol}}$ greater than -3 right across the

Table 4.2: Calculation of the modified Rossby number for the secondary stars in all 3 systems. A value of $R_0^{'} < 0.1$ means the star is saturated.

	Z Cha	HT Cas	OY Car
$M_2(M_\odot)$	0.08	0.09	0.07
$log\tau_e$	0.0913	0.099	0.077
τ_e	1.234	1.256	1.194
$P_{rot}(days)$	0.074	0.074	0.063
$R_o^{'}$	0.06	0.059	0.053

Table 4.3: Estimates of L_{bol} for the secondary stars using different methods. 1)Using the M-L relation and the secondary star's mass. 2) Using T_{eff} estimated from the spectral type.

	Z Cha	HT Cas	OY Car
$M_2(M_\odot)$	0.08	0.09	0.07
$log(L_{bol}/L_\odot)$	-3.0	-3.0	-3.2
$L_{bol}(\,\mathrm{erg\,s}^{-1})$(from M-L)	3.8×10^{30}	3.8×10^{30}	2.4×10^{30}
T_{eff}(k)	2850	2850	2850
$R_2(M_\odot)$	0.16	0.15	0.13
$L_{bol}(\,\mathrm{erg\,s}^{-1})$(from$T_{eff}$)	5.83×10^{30}	5.12×10^{30}	5.85×10^{30}

Table 4.4: Estimate of L_{bol} and L_X for a secondary star compared with L_X measured for the in-eclipse sources.

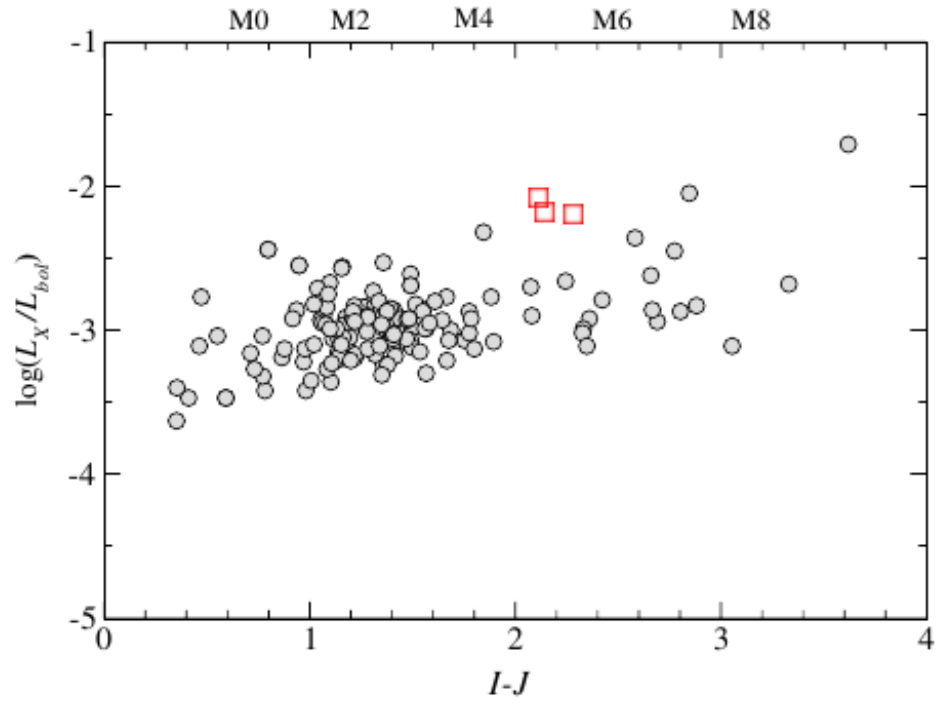|	Z Cha	HT Cas	OY Car
in-eclipse source			
$M_2(M_\odot)$	0.08	0.09	0.07
$L_{bol}\,(\,\mathrm{erg\,s}^{-1})$	3.8×10^{30}	3.8×10^{30}	2.4×10^{30}
L_X(observed)$\,\mathrm{erg\,s}^{-1}$	3.09×10^{28}	3.1×10^{28}	3.13×10^{28}
$log\frac{L_X}{L_{bol}}$	-2.27	-2.21	-2.27
theoretical M-dwarf			
$L_{bol}\,(\,\mathrm{erg\,s}^{-1})$	3.8×10^{30}	3.8×10^{30}	2.4×10^{30}
L_X (theoretical)$\,\mathrm{erg\,s}^{-1}$	3.84×10^{27}	3.84×10^{27}	3.42×10^{27}
$log\frac{L_X}{L_{bol}}$	-3	-3	-3

Figure 4.2: The $log\frac{L_X}{L_{bol}}$ values observed for active single M dwarfs compared to the values for the in-eclipse sources. The red squares indicate the approximate position of the in-eclipse sources. Original figure from Shkolnik et al. (2009).
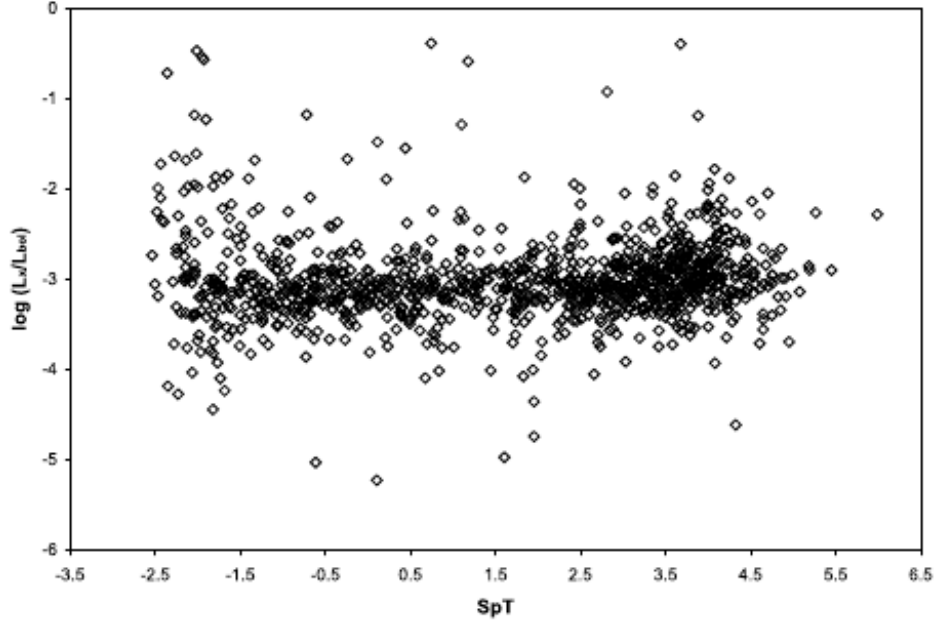
Figure 4.3: The $log\frac{L_X}{L_{bol}}$ values observed for active single M dwarfs showing many stars above the log -3 saturation limit. Original figure from Riaz et al. (2006).

M spectral type. The positions of the in-eclipse source from Z Cha, HT Cas and OY Car have been added for comparison and are clearly consistent with the overall trend. A study of 1080 active M-dwarfs (Riaz et al., 2006) found that the L_X range was $10^{26} - 10^{32}\,\mathrm{erg\,s^{-1}}$ with $log\frac{L_X}{L_{bol}}$ = -2 to -4 . The stars in this sample are saturated with $V\sin i > 15\,\mathrm{km\,s^{-1}}$. Fig 4.3 shows that although typical M-dwarfs had $log\frac{L_X}{L_{bol}} \sim -3$, there is a spread in the values up to -0.5 . One star in particular (2MASS 20194981-5816431) has a similar spectral type to the secondary stars of M6, and it had $log\frac{L_X}{L_{bol}} = -2.28$. It was suggested that this is a pre main sequence star and that its enlarged radius was the cause of its above average X-ray emission. Secondary stars of CVs are also thought to have an over inflated radius compared to their mass due to the star losing mass.

Another study (Robrade and Schmitt, 2005) found that for stars of spectral type M3.5-4.5 the X-ray luminosity was $5.4 - 6.6 \times 10^{28}\,\mathrm{erg\,s^{-1}}$ (table 4.5). This was based on a sample of single or wide binary M-dwarfs which are rapidly rotating and emitting at the saturated level ($log\frac{L_X}{L_{bol}}$ = -2.99 to -3.22).

At the far end of the M-dwarf spectral range, an observation of an M8 type star (Stelzer et al, 2006) detected $L_X \sim 5 \times 10^{27}\,\mathrm{erg\,s^{-1}}$ during quiescence. This star is emitting at the saturated level of $log\frac{L_X}{L_{bol}} = -3.1$. A flare that occurred during this observation provides a possible explanation for why the secondary stars

78

may have above average X-ray luminosity. During the flare, the L_X measured for this star increased from $5 \times 10^{27}\,\mathrm{erg\,s^{-1}}$ to $4.6 \times 10^{29}\,\mathrm{erg\,s^{-1}}$. If frequent flares are occurring on the secondaries of CVs then this could easily account for the in-eclipse sources being more X-ray luminous than predicted (see section 4.3).

It is thought that the coronal X-ray emission of low mass stars arises from two different components of the corona (Giampapa et al, 1996). There is a quiescent component which is fairly stable since it comes from the superposition of many small magnetic loops. There is also a higher temperature component which comes from flares and is therefore more variable.

The possible link between flares and the in-eclipse source is further supported by the similarity of the in-eclipse spectra to that of CN Leo (Schmitt et al, 2008) which has spectral type M5.5 the same as the secondary stars. This star has a much slower rotation rate of $v\sin i < 3\mathrm{kms^{-1}}$ (Fuhrmeister et al., 2004) but it was observed during a flare which is shown in fig 4.4. The spectrum of CN Leo during the flare has most of its emission in the 0.2-2 keV range with a peak at 0.9 keV which is very similar to the spectra of the in-eclipse sources e.g.(fig 4.6b).

Comparison with previous studies of the in-eclipse X-rays from OY Car
As discussed in section (1.2.3), a similar analysis was carried out by Ramsay et al (2001) on OY Car. Using the activity - rotation relation, Ramsay et al estimated L_X for a main sequence star with the same mass as the secondary of OY Car as less than $4 \times 10^{27}\,\mathrm{erg\,s^{-1}}$ using $M_2 = 0.1M_\odot$. The L_X value estimated for the in-eclipse source of OY Car was estimated at $L_X \sim 9 \times 10^{28}\,\mathrm{erg\,s^{-1}}$. This compares with $\sim 3 \times 10^{28}\mathrm{erg\,s^{-1}}$ which I have found for all 3 systems. Ramsay et al therefore concluded that the in-eclipse source of OY Car is too luminous to be the secondary star. However, when we take in to account other observations of M -dwarf stars, it seems that it is possible for them to have $L_X \sim 10^{28}\mathrm{erg\,s^{-1}}$. We must consider the possibility that the current activity - rotation relation is not appropriate for extremely rapidly rotating very low mass stars or the secondaries in CVs. In the samples used to derive the activity-rotation relation e.g.(Pizzolato et al, 2003), the most rapidly rotating stars had $v\sin i \sim 50\mathrm{kms^{-1}}$ which is only about half as fast as the spun up secondary stars with $v\sin i \sim 107\mathrm{kms^{-1}}$ (Copperwheat et al, 2012). Also the condition of the secondary star being gravitationally distorted by the white dwarf may make a difference to its magnetic activity.
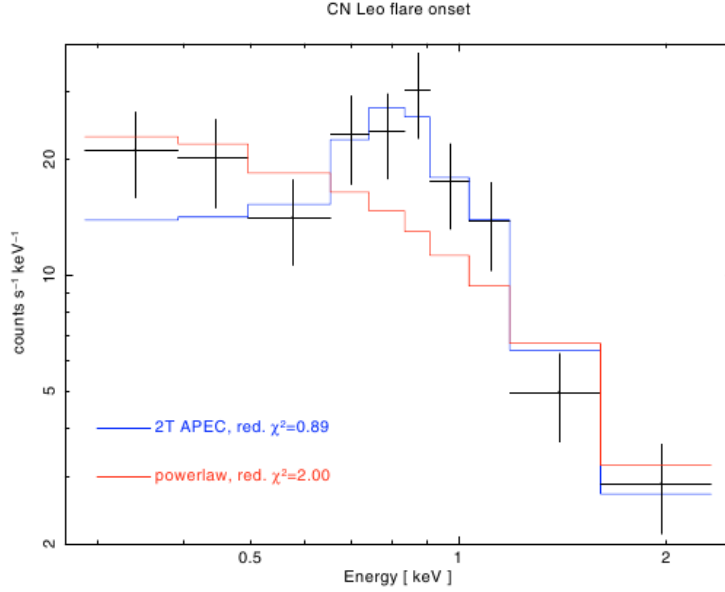
Figure 4.4: The X-ray spectrum of the spectral type M5.5 star CN Leo showing how the spectrum looked during a flare. The best fit model (blue line) is a 2-temp thermal plasma model. Figure reproduced from Schmitt et al (2008).

Comparing the in-eclipse spectra to M dwarf star spectra

The in-eclipse spectra from all 3 observations are shown in fig 3.15. The signal to noise ratio of the in-eclipse spectra is much lower than the out-of-eclipse spectra due to the low number of photons. The counts per bin are set at 10. The problem with having very low resolution is that it makes it hard to tell if we are seeing continuum emission possibly with line features or just line features with no continuum. The lack of resolution means that each bin could cover several lines which gives the spectrum the same appearance as continuum emission.

The spectral characteristics of 3 active M type stars (M3.5-4.5) were studied by Robrade and Schmitt (2005). These stars were well described by a 3 temperature plasma model (APEC). These stars are much closer than Z Cha, HT Cas and OY Car at around 25pc so the spectra are of much higher quality. They show a similar distribution to the in-eclipse sources with the majority of emission in the 0.2-1keV range. The Lx values of these 3 stars (AD Leo, EV Lac and AT Mic) are given in table 4.5 and are in the same range as the in-eclipse sources ($\sim 10^{28} - 10^{29} \mathrm{erg\,s^{-1}}$) despite having lower rotation rates 6-10 $\mathrm{km\,s^{-1}}$ compared to $\sim 109 \mathrm{km\,s^{-1}}$ for the CV secondaries.

Spectral fitting of the in-eclipse data resulted in acceptable reduced χ^2 fits

of 0.81 - 1.16 . The fits for HT Cas and OY Car had n_H of $3.4 \times 10^{20} \mathrm{cm}^{-2}$ and $6.4 \times 10^{19} \mathrm{cm}^{-2}$ which is reasonable for interstellar absorption in the direction and distance of these systems. However, the absorption needed for Z Cha was higher than would be expected if the in-eclipse source was the secondary star. This is because the accretion disk is the main source of absorption in the system, but during the eclipse, the accretion disk is on the far side of the system from our line of sight. The interstellar absorption in the direction of Z Cha has been estimated at $n_H = 0.09 \times 10^{20} \, \mathrm{cm}^{-2}$ (Dickey and Lockman, 1990) which is too low to justify this model. An alternative possibility is that the abundances of the secondary star are non-solar. This was tested by fitting with the vmekal model in XSPEC which allows for variation in the abundances of different elements. Fitting with vmekal resulted in a fit of 1.82 using more realistic absorption of $0.09 \times 10^{20} \mathrm{cm}^{-2}$. However the abundances of iron and oxygen were higher than solar at 11.6 and 1.16. These elements abundances were allowed to vary since they could be responsible for the peaks in the in-eclipse spectra at 0.6 keV and 0.85 keV which correspond to (iron) and (oxygen) respectively. Allowing these abundances to vary did improve the fit and it was always found that the oxygen abundance was ~ 10 times the iron abundance.

To see if this is reasonable I searched the literature for expected abundances of active low mass stars. Most studies e.g (Robrade and Schmitt, 2005) found that active M type stars have sub solar abundances in their corona which does not support my vmekal spectral fit. However, they do show that the spectra of M-dwarfs is dominated by emission lines of iron and oxygen which matches the peaks for the in-eclipse spectral data at 0.6 keV and 0.85 keV.

There is an interesting relation between the abundances of different elements called the inverse first ionisation potential effect (inverse FIP) (Brinkmann et al, 2001). The relation shows that the abundance of elements in stellar coronae increases proportionally to their first ionisation potential (fig 4.5). This is found to apply specifically to highly active stellar coronae wheras the normal FIP effect applies to less active stars. The in-eclipse fit for Z Cha using vmekal resulted in an oxygen abundance ~ 10 times greater than iron. This can be compared to what is predicted by the inverse-FIP effect. Oxygen has a higher first ionisation potential than iron so the relative (O/Fe) abundance according to the inverse FIP effect (fig 4.5) should mean that oxygen is 3-5 times more abundant than iron. While the in-eclipse spectrum of Z Cha seems to show the expected ratio of oxygen relative to iron, there is still the problem of why the abundances of these elements would be enhanced when observations of low mass star show under abundance. It
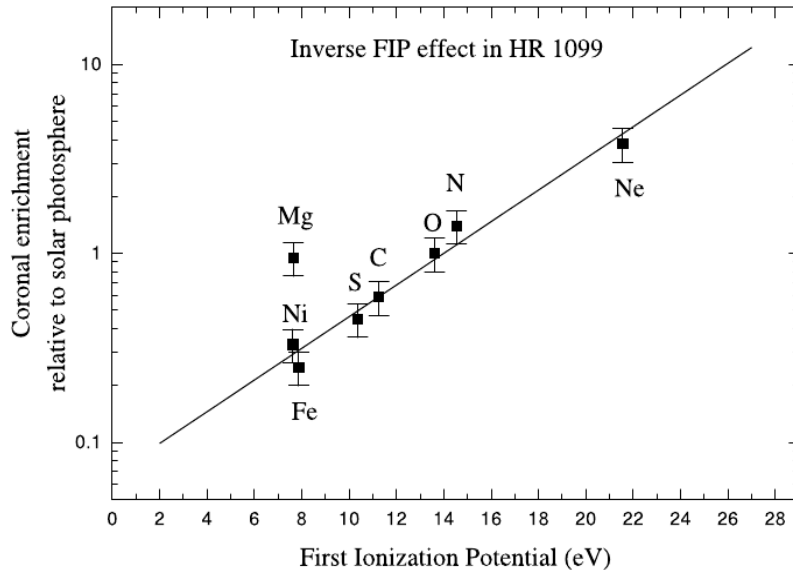
Figure 4.5: The inverse FIP effect for coronal abundances in active low mass stars. This shows that the abundance of oxygen is enhances with respect to iron. Figure reproduced from Brinkmann et al (2001).

is possible that the secondary stars of CVs have become contaminated by processes such as nova explosions which contaminate the secondary with material from the white dwarf (Stehle and Ritter, 1999). There is also evidence that stars with a lot of flaring activity show the inverse FIP effect, possibly because the flares bring up material from the lower layers of the star (Audard et al, 2003). If frequent flaring is enhancing the L_X of the secondary star, then it is likely that the star would also show the inverse FIP effect.

Comparison with binary central stars of planetary nebulae

An interesting comparison can be made between the X-ray luminosity detected in Z Cha, HT Cas and OY Car and the L_X detected from the central stars of planetary nebulae (CSPN). Some planetary nebulae are thought to be systems which have just ended the common envelope phase and are evolving into CVs (Montez et al, 2010). Accretion has not yet started so the only X-ray source would be the secondary star. The white dwarf is not expected to be a significant source of X-rays in these systems e.g.((O'Dwyer et al, 2003),(Groth et al., 1985)). Montez et al (2010) detected X-ray emission attributed to the secondary star of $logL_X \sim 29 - 30\,\mathrm{erg\,s^{-1}}$ in two CSPN sources (HFG 1 and DS 1) where the secondary star mass is estimated at $0.2-0.4M_\odot$.

Figure 4.6: Comparison between the in-eclipse spectrum of Z Cha (a) and the X-ray source from the central star of a planetary nebula (b). Note that the x axis is not the same scale on each diagram.
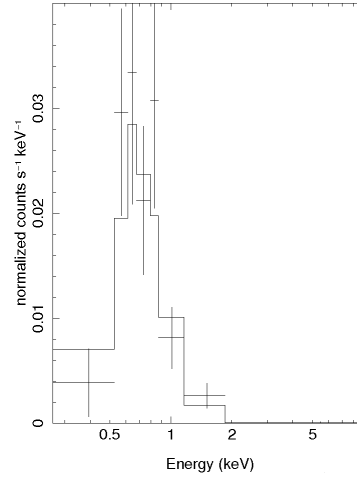
(a) Z Cha in-eclipse spectrum.
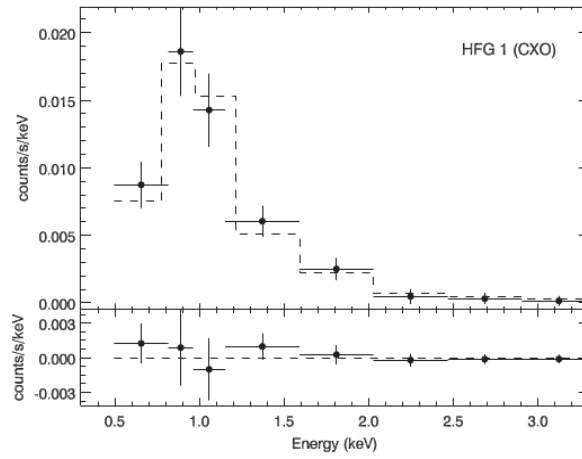
(b) CSPN (Montez et al, 2010)
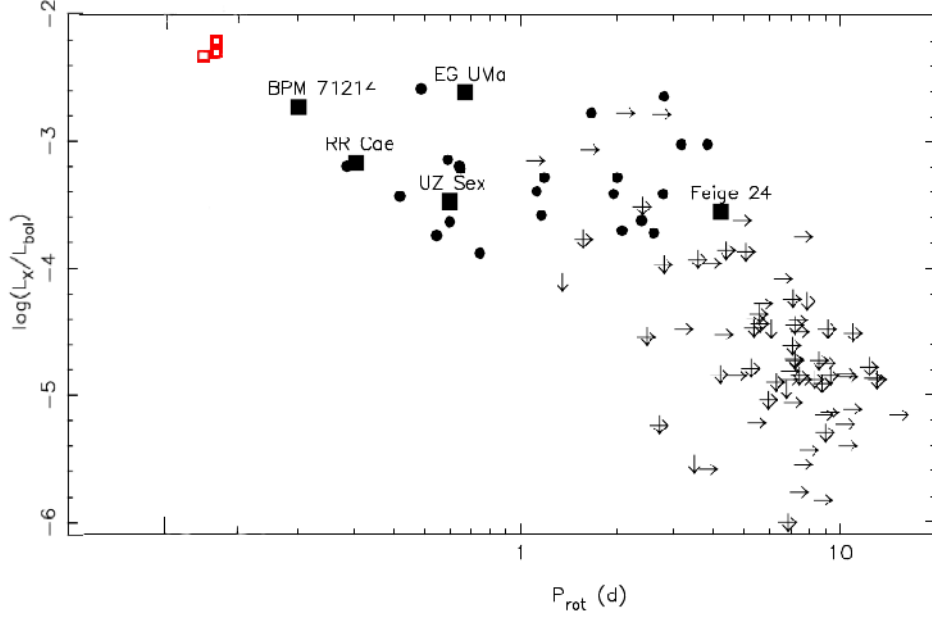
Figure 4.7: Comparison of the $log\frac{L_X}{L_{bol}}$ values for pre CVs and single M-dwarfs with the in-eclipse sources in Z Cha, HT Cas and OY Car. The red squares indicate the approximate positions of the in-eclipse sources for comparison. Original figure from Briggs et al (2007).

This is slightly higher mass than Z Cha, HT Cas and OY Car ($\sim 0.1 M_\odot$) so the saturated L_X emission would be expected to be stronger. The spectrum of HFG 1 (fig 4.6b) has a peak at 0.9keV the same as the in-eclipse source for Z Cha (fig 4.6a). Both have been fitted with a two temperature plasma model temperatures of 0.5keV and 1.8keV for HFG1 and 0.2keV and 1.98keV for Z Cha. For DS 1, the $log\frac{L_X}{L_{bol}}$ was calculated at 2.0 ± 0.3 which is above the saturation level and is very close to the values found for the in-eclipse sources. A similar study (Soker and Kastner, 2002) of another CSPN source (NGC 7293) found $L_X > 5 \times 10^{29}\,\mathrm{erg\,s}^{-1}$ (table 4.5). For both these studies the authors suggest that the observed X-ray emission is probably due to coronal emission from a late type companion.

Comparison with pre-CVs

Pre CVs are systems with a white dwarf and a low mass main sequence star where the stars are not yet close enough for Roche lobe overflow to begin. Since there is no mass transfer to power X-ray emission from accretion, any X-ray emission from these systems must come from the corona of the spun up main sequence star. If this

is the case, then the X-ray emission of pre CVs and the in-eclipse sources from CVs should have the same characteristics if the in-eclipse source is the secondary star. A study by Briggs et al (2007) found that the $log\frac{L_X}{L_{bol}}$ for some of the shortest period pre CVs (P_{rob} 0.2 days) was ~ -2.7 which is above the saturation level (fig 4.7). The pre CV EG UMa was also thought to be undergoing a flare during the observation based on the changes in its light curve. This system was found to have $log\frac{L_X}{L_{bol}} =$ -2.6 (table 4.5). These pre CV systems have slightly longer rotation periods than Z Cha, HT Cas and OY Car at 0.2 - 0.8 days compared to 0.07 days for Z Cha. Figure 4.7 taken from Briggs et al (2007) has been modified to include the in-eclipse sources from Z Cha, HT Cas and OY Car based on the $log\frac{L_X}{L_{bol}}$ values calculated in this thesis for comparison with pre CVs. This shows that the $log\frac{L_X}{L_{bol}}$ values for the in-eclipse sources are higher than for pre CVs, but don't seem unreasonable given the amount of scatter in the values for pre CVs and single M-dwarfs. Another study by Matranga et al (2012) found that the L_X for an M-dwarf observed during the eclipse of the pre CV (QS Vir), which is thought to be on the verge of Roche lobe overflow, was $L_X = 3 \times 10^{28} \mathrm{erg\,s^{-1}}$ which is very close to the values found for the in-eclipse sources ($\sim 3.1 \times 10^{28} \mathrm{erg\,s^{-1}}$).

Table 4.5: Comparison of the L_X values measured for Z Cha, HT Cas and OY Car with observations of rapidly rotating low mass stars from the literature. Also included are observations of the X-ray emission from central stars of planetary nebulae where the emission is thought to come from a late type companion which is highly spun up.

	Name	SpT	Mass($M_\odot$)	$log\frac{L_X}{L_{bol}}$	L_X erg s^{-1}	Reference
Observed in-eclipse sources	Z Cha	M5.5V	0.08	-2.27	3.09×10^{28}	this thesis
	HT Cas	M5.4V	0.09	-2.21	3.1×10^{28}	-
	OY Car	-	0.07	-2.27	3.13×10^{28}	-
Low mass stars	AD Leo	M3.5	-	-3.2	2.9×10^{29}	(Robrade and Schmitt, 2005)
	AT Mic	M4.5/4	-	-3	5.39×10^{28}	(Robrade and Schmitt, 2005)
	CN Leo	M6 Ve	~ 0.1	-2.86	$\sim 10^{27.78}$	(Giampapa et al, 1996)
	LP412-31	M8	0.04-0.1	-3.1	$< 5 \times 10^{27}$	(Stelzer et al, 2006)
	sample	K5-M6	-	-2 to -4	$10^{26} - 10^{32}$	(Riaz et al., 2006)
CSPN	HFG1	-	0.41	-3±0.2	$\sim 10^{30}$	(Montez et al, 2010)
	DS1	-	0.23	-2±0.3	$\sim 10^{29}$	(Montez et al, 2010)
	NGC 7293	-	-	-	5×10^{29}	(Soker and Kastner, 2002)
pre CVs	BPM 71214	M2.5		-2.7		(Briggs et al, 2007)
	EG UMa	M4-5		-2.6		(Briggs et al, 2007)

Overall, it seems that the in-eclipse sources have a higher luminosity than a typical M-dwarf. However, there are many exceptional cases which show that such high values are possible if not typical. When compared to CSPN and pre CVs, it seems that high luminosities are more typical of these types of systems. Z Cha, HT Cas and OY Car all have similar values to each other, as well as being more typical of CSPN and pre-CVs than single M-dwarfs. This may indicate that the special circumstances where stars are extremely spun-up make it possible for them to break the saturation limit in a way which is not possible in single stars.

4.2.3   Scattered boundary layer emission

The possibility that the in-eclipse X-rays are in fact scattered boundary layer emission was tested using XSTAR. This was used to produce a simulated scattered boundary layer model which was then fitted to the in-eclipse spectra using XSPEC.

When the normalisation was fixed at the same level as for the best fit input spectrum from the boundary layer, a good fit could not be found. However, the fits always had the lowest column density available in the model of 10^{19}cm^{-2} which indicated that an even lower column density of material was required to produce the observed in-eclipse spectrum. The column density which could have resulted in a good fit to the in-eclipse spectrum of Z Cha was estimated at 8.3×10^{17}cm^{-2}.

An order of magnitude estimate of the distance of the scattering material from the white dwarf and boundary layer was made using the parameters from the spectral fitting (Wheatley and Kallman, 2006). This done by combining the equations for the ionisation parameter and the column density (eqn 4.1 and 4.2 respctively).

$$\xi = \frac{L}{nR^2} \tag{4.1}$$

$$N_H = nl \tag{4.2}$$

$$\xi = \frac{Ll}{N_H R^2} \tag{4.3}$$

In these equations ξ is the ionisation parameter, N_H is the column density of the scattering medium and L is the luminosity of the source, which in this case is calculated from the flux of the out-of-eclipse source. Rearranging (4.2) gives $n = \frac{N_H}{l}$ which is substituted in to (4.1) to give equation (4.3). If we replace l, (the path length through the scattering medium) with R which is the maximum distance of

the scattering medium from the source, then we can cancel l and re-arrange to find R_{max} (eqn 4.4). This assumes a constant density sphere of material around the white dwarf and a constant ξ which is not realistic but allows an order of magnitude estimate of R_{max} to be made.

$$R_{max} = \frac{L}{\xi N_H} \tag{4.4}$$

R_{max} may be underestimated using this method because L is probably greater than what is calculated from the out-of-eclipse source since there may be absorption by the accretion disk along our line of sight but less in the directions above and below the disk.

As a test of the plausibility of the scattering scenario, I calculated the distance the scattering material would extend from the white dwarf/boundary layer to produce the results given by the spectral fitting.

The calculation was made for Z Cha using the extrapolated value for N_H and resulted in a maximum radial distance of the scattering medium from the source of 8.6×10^8cm. This is only $1.23 R_{WD}$. By comparison, the secondary star in Z Cha has a radius of $15\,R_{WD}$. If the scattering medium were this close to the white dwarf, it would still be eclipsed. Even if this estimate is too small by an order of magnitude, the scattering medium would still have a smaller extent than the radius of the secondary star. This test shows that the scattering scenario can be ruled out assuming that the extrapolated value of N_H is valid.

4.3 Implications

If it is true that the in-eclipse X-rays are from the secondary star, this study shows that these must be highly active and emitting X-rays above the normal saturation limit for M-dwarf stars. While an explanation for this enhanced X-ray emission can only be speculative at this point, it does seem that the levels of X-ray activity seen for the in-eclipse sources can occur in very rapidly rotating M-dwarfs. Enhanced emission is also seen in some pre CVs and CSPN systems which would be expected to have similar properties to the secondaries in CVs.

From the observational evidence, it seems that the theoretical estimate of $3 \times 10^{27}\,\mathrm{erg\,s^{-1}}$ is towards the low end of observed X-ray luminosities for active M-dwarfs around spectral type M5. The magnetic activity of fully convective stars is still poorly understood and it is possible that the rapid rotation and tidal distortion of the secondary star has unknown effects on the fully convective dynamo.

One possible explanation for the X-ray emission being above the 10^{-3} saturation limit is that the X-ray luminosity could be enhanced by emission from slingshot prominences. These are coronal structures which may exist in rapidly rotating stars and consist of a thin magnetic loop embedded in the stellar wind. These slingshot prominences can theoretically extend out to 5 stellar radii and are filled with X-ray emitting gas from the stellar wind (Jardine and Ballegooijen, 2005). A slingshot prominence was proposed as an explanation for a H_α emission peak observed in the CV J003941.06 +005427.5 (Southworth et al, 2010) which has a very rapidly rotating, fully convective secondary, with P_{orb} 91.4 min. Slingshot prominences may also have been observed in the CVs IP Peg and SS Cyg (Steeghs et al, 1996) which contain low mass rapidly rotating secondaries.

Chapter 5

Conclusion

The main conclusion from this investigation of Z Cha, HT Cas and OY Car, is that an X-ray source is detected during eclipse for all 3 systems. This is in agreement with previous studies of OY Car (Wheatley and West, 2002), (Ramsay et al, 2001) and shows that it is not an isolated phenomenon since in-eclipse X-rays are also detected from Z Cha and HT Cas during quiescence. The source in all 3 systems is very faint but is still detected at the $3 - 6\sigma$ level above the background.

I have also shown that in all 3 systems the in-eclipse source is much softer than the out of eclipse source with most of the emission in the $0.2 - 1.4 \, \text{keV}$ range. The in-eclipse source is not detected in the hard $1.4 - 10 \, \text{keV}$ range. In comparison, the out-of-eclipse source emits strongly across the whole $0.2 - 10 \, \text{keV}$ range. This suggests that the in-eclipse X-rays have a different origin to the out-of-eclipse X-rays which are known to come mainly from the boundary layer.

Analysis of the optical light curves showed that the bright spot may be visible during the first half of the in-eclipse period for the Z Cha observation. However, analysis of the X-ray light curve showed that this was not the main source of in-eclipse X-rays and a source was still detected during the second half of the eclipse when the bright spot was eclipsed. There was no significant difference between the counts in the first and second half of the eclipses of HT Cas and OY Car. This shows that the bright spot is not the main source of in-eclipse X-rays in any of the 3 observations.

Analysis of the variability of the in-eclipse source compared to the out-of-eclipse source could find no evidence that they varied in unison although the low signal to noise ratio of the in-eclipse data limits the usefulness of this test. The χ^2 result for Z Cha showed that the variation of the in-eclipse count rate is not a good model for the variation in the out-of-eclipse source count rate. From this I conclude

that, at least in the case of Z Cha, the in-eclipse X-rays are likely to have a different origin to the out-of-eclipse X-rays.

For the out-of-eclipse spectra, a good fit was found with a 2 temperature plasma model with absorption. The temperatures of the 2 components are approx $1\,\mathrm{keV}$ and $7-9\,\mathrm{keV}$. Attempts to fit the same model to the in-eclipse spectra did not result in a good fit. This is further evidence that the origin of the in-eclipse X-rays must be a different source to the out-of-eclipse X-rays.

The best fit model for the in-eclipse sources was found to be a 2 temperature Mekal model with Wabs absorber. The in-eclipse X-ray luminosity based on the flux from the spectral fits and distance estimates taken from the literature was $L_X \sim 3 \times 10^{28}\,\mathrm{erg\,s^{-1}}$ for all 3 systems. The obvious similarity of the in-eclipse sources in all 3 systems increases our confidence that this is a genuine detection and it is due to a feature which is constant in CVs and not just a transient phenomenon.

Based on further analysis of the results, I conclude that the most likely source of the in-eclipse X-rays is coronal emission from the secondary star. This is supported by several pieces of evidence.

Firstly the X-ray luminosity of the in-eclipse sources ($\sim 3 \times 10^{28}\,\mathrm{erg\,s^{-1}}$) is consistent with observed X-ray luminosity for the most active rapidly rotating main sequence stars. If the in-eclipse source is the secondary star, it is highly spun up and very X-ray active, as would be expected for a tidally locked secondary star.

Comparison with the L_X predicted by the activity-rotation relation showed that the in-eclipse X-ray luminosity is an order of magnitude greater than predicted. However, a wide range of studies of rapidly rotating low mass stars have detected L_X greater than $10^{27}\,\mathrm{erg\,s^{-1}}$. This suggests that the predicted L_X value is at the low end of possible values and cannot rule out the possibility of secondary star emission.

It is also evident that CSPN and pre CV sources can emit X-rays above the saturation level at close to $log\frac{L_X}{L_{bol}} = -2$ which is consistent with the in-eclipse sources. The fact that we know the secondary star is in our direct line of sight during the full eclipse period makes it unlikely that we would not see some evidence of it if it is emitting X-rays as expected. The alternative scenario where boundary layer X-rays are scattered in to our line of sight was shown to be unrealistic. Calculation of the required distance of the scattering medium from the white dwarf based on the parameters of the best fitting spectral model showed that the scattering medium would be too close to the white dwarf to be the source of in-eclipse X-rays.

Given the lack of a realistic scattering spectral model, and the fact that the bright spot only contributes a small proportion of the X-rays detected in the Z Cha observation, it does not seem reasonable to invoke these as the main source of

in-eclipse X-rays.

The use of highly sensitive satellites such as XMM-Newton has now made it possible to detect the in-eclipse source. Unfortunately the faintness of the source, and the fact that it can only be observed during short in-eclipse periods, means the data obtained is of low signal to noise ratio. The major problem with this investigation is the lack of in-eclipse counts in the spectral data which might have made it easier to conclusively rule out some of the possible in-eclipse sources.

As a follow-up to this investigation, it would be beneficial to investigate the eclipses of other CVs and low mass X-ray binaries as well as central stars of planetary nebulae to attempt to confirm the link between the X-ray emission and the secondary star. This may help to shed light on the early evolution of pre-CVs which is likely to be driven by the magnetic braking of the secondary star which is closely linked to its magnetic field and X-ray emission. Investigations may also provide insight into the possible role of magnetic braking in CVs below the period gap which had been thought to be affected only by gravitational radiation.

Bibliography

J.H. Applegate and J. Patterson. *ApJ*, 322:L99, 1987.

K. Arnaud. heasarc.nasa.gov/xanadu/xspec/XspecManual.pdf.

K.A. Arnaud. *ASP Conf Series*, 101:17, 1996.

M. Audard et al. *A & A*, 398:1137, 2003.

H. Awaki. *ASPC*, 113:44, 1997.

J. Bailey et al. *MNRAS*, 197:31, 1981.

R. Baptista et al. *MNRAS*, 335:57, 2002.

G. Belvedere, L. Paterno, and M. Stix. *A & A*, 88:240, 1980.

K. Beuermann and M. Weichhold. *ASPC*, 157:283, 1999.

B.W. Borges et al. *A & A*, 480:481, 2008.

J.M. Brett and R.C. Smith. *MNRAS*, 264:641, 1993.

K.R. Briggs et al. *ASP Conf Ser*, 372, 2007.

A.C. Brinkmann et al. *A & A*, 365:L324, 2001.

C.G. Campbell and J. Papaloizou. *MNRAS*, 204:433, 1983.

W. Cash. *ApJ*, 228:939, 1979.

C.M. Copperwheat et al. *MNRAS*, 421:149, 2012.

F. D'Antona and I. Mazzitelli. *ApJS*, 90:467, 1994.

de la Calle et al. *Users Guide to the XMM-Newton Science Analysis System*. ESA, issue 8.0 edition, 2011.

J.M. Dickey and F.J. Lockman. *ARA&A*, 28:215, 1990.

W.J. Feline et al. *MNRAS*, 364:1158, 2005.

T.A. Fleming et al. *ApJ*, 410:387, 1993.

E.N. Frazier. *Solar Phys*, 14:89, 1970.

B. Fuhrmeister, J.H.M.M. Schmitt, and R. Wichmann. *A & A*, 417:701, 2004.

M.S. Giampapa et al. *ApJ*, 463:707, 1996.

G. Giuricin, F. Mardirossian, and M. Mezzetti. *A & A*, 141:227, 1984.

J.G. Greenhill et al. *MNRAS*, 372:1129, 2006.

H.G. Groth, R.P. Kudritzki, and U. Heber. *A & A*, 152:107, 1985.

M. Gudel and Y. Naze. *A & A review*, 17:309, 2009.

Hale Bradt. *Astronomy Methods*. Cambridge, 2004.

F.V. Hessman et al. *ApJ*, 286:747, 1984.

F.V. Hessman et al. *A & A*, 213:167, 1989.

K. Horne, J.H. Wood, and R.F. Steining. *ApJ*, 378:271, 1991.

K. Horne et al. *ApJ*, 426:294, 1994.

S.S. Huang. *AnAp*, 29:331, 1966.

Y. Hyodo et al. *PASJ*, 61:99, 2009.

D.J. James et al. *MNRAS*, 318:1217, 2000.

F. Jansen, D. Lumb, and B. Altieri. *A & A*, 365:L1–L6, 2001.

M. Jardine and A.A. Ballegooijen. *MNRAS*, 361:1173, 2005.

Y.K. Jin, S.N. Zhang, and J.F. Wu. *ApJ*, 653:1566, 2006.

T. Kallman. http://heasarc.gsfc.nasa.gov/xstar/xstar.html, 1999.

R. Kippenhahn and A. Weigert. *Stellar Structure*, volume 100. Springer - Verlang, 1990.

C. Knigge. *MNRAS*, 373:484, 2006.

C. Knigge, I. Baraffe, and J. Patterson. *ApJS*, 194:28, 2011.

Z. Kopal. *ASPL*, 8:81, 1959.

Z. Kopal. *Dynamics of Close Binary Systems*. Dordrecht Reidel Publishing Co, 1978.

G.P. Kuiper. *ApJ*, 93:133k, 1941.

M. Lampton, B. Margan, and S. Bowyer. *ApJ*, 208:177, 1976.

M. Livio. *Accretion disks in Compact Stellar Systems*, volume 9. Singapore World Scientific, 1993.

M. Livio and N. Soker. *ApJ*, 329:764, 1988.

S.H. Lubow and F.H. Shu. *ApJ*, 198:383, 1975.

O.Y. Malkov et al. *A & A*, 320:79, 1997.

T.R. Marsh. *ApJ*, 357:621, 1990.

M. Matranga et al. *ApJ*, 747:132, 2012.

C.W. Mauche. *ASPC*, 137:113, 1998.

Z. Meglicki, D. Wickramasinghe, and G.V. Bicknell. *MNRAS*, 264:691, 1993.

L. Mestel. *MNRAS*, 138:359, 1968.

R. Mewe, E.H.B.M. Gronenschild, and G.H.J. van den Oord. *A & A*, 62:197, 1985.

R. Montez et al. *ApJ*, 721:1820, 2010.

R. Morrison and D. McCammon. *ApJ*, 270:119, 1983.

K. Mukai and J.H. Wood et al. *ApJ*, 475:812, 1997.

G.S. Mumford. *IBVS*, 337:1, 1969.

NASA XMM-Newton pages. http://ixo.gsfc.nasa.gov/technology/hxiNIckelOptics.html.

T. Naylor and C. La Dous. *MNRAS*, 290:160, 1997.

R.W. Noyes et al. *ApJ*, 279:763, 1984.

A.A. Nucita et al. *A & A*, 504:973, 2009.

I.J. O'Dwyer et al. *AJ*, 125:2239, 2003.

Y. Osaki. *PASJ*, 26:429, 1974.

Y. Osaki. *PASP*, 108:39, 1996.

J. Ostriker. *Int Ast Union Symp*, 73:206, 1976.

B. Paczynski. *ACTA*, 17(287), 1967.

B. Paczynski. *ARA&A*, 9:183, 1971.

R. Pallavicini et al. *ApJ*, 248:279, 1981.

J.C.B. Papaloizou and D.N.C. Lin. *ARAA*, 33:505, 1995.

E.N. Parker. *ApJ*, 264:635, 1983.

J. Patterson. *ApJs*, 45:517, 1981.

J. Patterson et al. *ASOP*, 117:1204, 2005.

N. Pizzolato et al. *A & A*, 397:147, 2003.

G.W. Pratt et al. *MNRAS*, 307 issue 2:413, 1999a.

G.W. Pratt et al. *MNRAS*, 309:847, 1999b.

J.E. Pringle and G.J. Savonije. *MNRAS*, 187:777, 1979.

J.E. Pringle et al. *MNRAS*, 178:195, 1977.

C.F. Prosser et al. *AJ*, 112:1570, 1996.

G. Ramsay et al. 2001a. *A & A*, 365:L294, 2001.

S. Rappaport, F. Verbunt, and P.C. Joss. *ApJ*, 275:713, 1983.

S. Rappaport et al. *ApJ*, 187:L5, 1974.

B. Riaz, J.E. Gizis, and J. Harvin. *ApJ*, 132:866, 2006.

H. Ritter and U. Kolb. *A & A*, 404:301, 2003.

J. Robrade and J.H.M.M. Schmitt. *A & A*, 435:1073, 2005.

R. Rosner. *SAOSR*, 389:79, 1980.

J.H.M.M. Schmitt et al. *A & A*, 481:799, 2008.

R. Schoembs, H. Dreier, and H. Barwig. *A & A*, 181:50, 1987.

Y. Shao and X.D. Li. *ApJ*, 745:165s, 2012.

M.R. Sherrington et al. *MNRAS*, 200:861, 1982.

E. Shkolnik, M.C. Liu, and I.N. Reid. *ApJ*, 699:649, 2009.

A. Skumanich. *ApJ*, 171:565, 1972.

J. Smak. *IAUS*, 88:443, 1980.

N. Soker and J.H. Kastner. *ApJ*, 570:245, 2002.

J. Southworth et al. *A & A*, 524:A86, 2010.

K.G. Stassun et al. *ASP Conference Series arXiv*, 2010.

D. Steeghs et al. *MNRAS*, 281:626, 1996.

R. Stehle and H. Ritter. *MNRAS*, 309:245, 1999.

B. Stelzer et al. *A & A*, 460:35, 2006.

P. Szkody and J.A. Mattei. *PASP*, 96:988, 1984.

L. Testi. *A & A*, 503:639, 2009.

A. van Teeseling. *A & A*, 319:L25, 1997.

P. Ventura et al. *A & A*, 334:953, 1998.

F. Verbunt. *SSRV*, 32:379, 1982.

O. Vilhu. *A & A*, 133:117, 1984.

N. Vogt et al. *A & A*, 94:L29, 1981.

R.A. Wade. *ApJ*, 246:215, 1981.

R.A. Wade and K. Horne. *ApJ*, 324:411, 1988.

F.M. Walter and S. Bowyer. *ApJ*, 245:671, 1981.

B. Warner. *MNRAS*, 168:235, 1974.

B. Warner. *IAUS*, 73:85, 1976.

B. Warner. *Ap&SS*, 232:89, 1995a.

B. Warner. *Cataclysmic Variable Stars*. Cambridge University Press, 1995b.

R.F. Webbink. *Apcb.Conf*, 177, 1990.

E.J. Weber and L.J. Davis. *ApJ*, 148:217, 1967.

P.J. Wheatley. *MNRAS*, 297:1145, 1998.

P.J. Wheatley and T.R. Kallman. *MNRAS*, 372:1602, 2006.

P.J. Wheatley and R.G. West. *ASPC*, 261:433, 2002.

R. Whitehurst. *MNRAS*, 232:35, 1988.

J.H. Wood. *Ap&SS*, 130:81, 1987.

J.H. Wood, K. Horne, and S. Vennes. *ApJ*, 385:294, 1992.

J.H. Wood et al. *MNRAS*, 219:629, 1986.

J.H. Wood et al. *ApJ*, 341:974, 1989.

J.H. Wood et al. *MNRAS*, 273:772, 1995.

XMM Newton Users Handbook. "XMM-Newton Users Handbook", Issue 2.9, 2011 (ESA: XMM-Newton SOC), 2011.

P. Young, D.P. Schneider, and S.A. Schectman. *ApJ*, 245:1035, 1981.

J.P. Zahn. *A & A*, 57:383, 1977.

M. Zeilik, S.A. Gregory, and E.V.P. Smith. *Introductory Astronomy & Astrophysics*. Thompson Learning, 1992.

E.H. Zhang, E.L. Robinson, and R.E. Nather. *ApJ*, 305:740, 1986.